INFORMATION TO USERS

This manuscript has been reproduced from the microfilm master. UMI films the text directly from the original or copy submitted. Thus, some thesis and dissertation copies are in typewriter face, while others may be from any type of computer printer.

The quality of this reproduction is dependent upon the quality of the copy submitted. Broken or indistinct print, colored or poor quality illustrations and photographs, print bleedthrough, substandard margins, and improper alignment can adversely affect reproduction.

In the unlikely event that the author did not send UMI a complete manuscript and there are missing pages, these will be noted. Also, if unauthorized copyright material had to be removed, a note will indicate the deletion.

Oversize materials (e.g., maps, drawings, charts) are reproduced by sectioning the original, beginning at the upper left-hand corner and continuing from left to right in equal sections with small overlaps.

ProQuest Information and Learning
300 North Zeeb Road, Ann Arbor, MI 48106-1346 USA
800-521-0600

UMI®

DISSERTATION

MATERIALS SYNTHESIS STRATEGIES FOR: MICROSTRUCTURE SELF-ASSEMBLY, POLYMER-ENCAPSULATED REVERSE MICELLES, IONIC DONORS IN BIMOLECULAR PHOTOSYSTEMS, AND EFFICIENT MEDIATORS IN DYE-SENSITIZED SOLAR CELLS

Submitted by

Shawn A. Sapp

Department of Chemistry

In partial fulfillment of the requirements

for the Degree of Doctor of Philosophy

Colorado State University

Fort Collins, CO

Fall 2002

COLORADO STATE UNIVERSITY

July 23, 2002

WE HEREBY RECOMMEND THAT THE DISSERTATION PREPARED UNDER OUR SUPERVISION BY SHAWN A. SAPP ENTITLED "MATERIALS SYNTHESIS STRATEGIES FOR: MICROSTRUCTURE SELF-ASSEMBLY, POLYMER-ENCAPSULATED REVERSE MICELLES, IONIC DONORS IN BIMOLECULAR PHOTOSYSTEMS, AND EFFICIENT MEDIATORS IN DYE-SENSITIZED SOLAR CELLS" BE ACCEPTED AS FULFILLING, IN PART, REQUIREMENTS FOR THE DEGREE OF DOCTOR OF PHILOSOPHY.

Committee on Graduate Work

Advisor

Department Chair

ABSTRACT OF DISSERTATION

MATERIALS SYNTHESIS STRATEGIES FOR: MICROSTRUCTURE SELF-ASSEMBLY, POLYMER-ENCAPSULATED REVERSE MICELLES, IONIC DONORS IN BIMOLECULAR PHOTOSYSTEMS, AND EFFICIENT MEDIATORS IN DYE-SENSITIZED SOLAR CELLS

Materials synthesis strategies have been applied to a number of projects in a variety of research fields. First, the synthesis of an amine-functionalized monomer that forms a conducting polymer was used to produce a material that could easily be used in template-synthesis to produce micro- and nanostructures. These amine-functionalized structures were employed to investigate the use of avidin-biotin technology for self-assembly. The successful self-assembly of micro- and nanoparticles to microfibers and microtubes is reported.

Second, reverse micelles were used to direct the phase segregation of a polar dye solution in a non-polar monomer. Polymerization of these mixtures resulted in encapsulation of the reverse micelles. Solid monolithic samples of optical quality that exhibit solution-state photophysical properties were obtained. The development and characterization of these materials is discussed in detail.

Third, a number of ionic derivatives of phenothiazine were synthesized and investigated as electron donors in bimolecular photosystems. These systems were

characterized by transient absorption spectroscopy under the same conditions used to study non-ionic phenothiazine donors. The results of these studies are compared to previous results. Additionally, a mixed salt of a cationic chromophore-acceptor diad and an anionic phenothiazine was metathesized and sequestered in the core of reverse micelles. The photophysics of this system was studied in the presence and absence of a magnetic field, and found to retain magnetic field-affected recombination kinetics similar to covalently-linked donor-chromophore-acceptor triads.

Finally, alkyl-substituted polyimine complexes of cobalt(II) and cobalt(III) were discovered to act as efficient electron-transfer mediators in dye-sensitized solar cells. A series of complexes encompassing a wide range of thermodynamic, structural, and steric characteristics was synthesized. This was accomplished through the use of polyimine ligands appended with electron-donating or electron-withdrawing substituents having a variety of steric requirements. The spectral properties and electrochemical behavior of the corresponding complexes were studied. Comparison of the electrochemical results with the performance of dye-sensitized solar cells containing cobalt complex-based mediators revealed empirical trends that could be used to identify potentially efficient mediators. A detailed discussion is presented on these findings as well as on the photoelectrochemical performance of optimized cobalt complex-mediated cells.

Shawn A. Sapp
Department of Chemistry
Colorado State University
Fort Collins, CO 80523
Fall 2002

ACKNOWLEDGMENTS

The body of work represented by this dissertation would not have been realized were it not for the help of many others that I would now like to gratefully acknowledge. First and foremost is my advisor, Professor C. Michael Elliott, who took me into his group as a third-year graduate student from the departing Martin research group. In the time since then, Mike has been an excellent mentor and a friend who has both inspired me and helped me to realize my full potential as a scientist and a writer. Together we have accomplished much in these few years, and I appreciate all of the rare opportunities he has given me that have helped me become a better chemist.

I owe Prof. John R. Reynolds at the University of Florida a great deal of thanks. This journey for me all began a long time ago in his office when he offered to let me conduct undergraduate research in his group with the understanding that if all went well (and it went *very* well) I would pursue my Ph.D. in chemistry. Prof. Reynolds is the reason behind why I have come so far; thanks for believing in me.

I must also acknowledge the students, post-docs, teachers, and professionals whom I have worked with throughout my education who have inspired and influenced me despite all odds: Profs. and Drs. Carlo Bignozzi, Sue Fererre, Brian Gregg, Chuck Martin, Nancy Levinger, George Barisas, Dave Grainger, Dieter Hochheimer, Steve Strauss, Peter Dorhout, Bruce Parkinson, Bob Lee, Randy Duran, Gregory Sotzing, Jerry Reddinger, All members of the Elliott research group whom I have had the good fortune

to work with, Veronica Cepak, Charlie Patrissi, Dave Mitchell, Kshama Jirage, Silvia Lueben, Brinda Lakshmi, Ron Brandolini, Mrs. Beechum, Ms. Jensen, Dr. Skinner, Mrs. Gillespie, Mrs. Stenson, and Mr. Ball

My classmates, roommates, and friends: Drs. Brady Clapsaddle, Jon Lorenz, Jeremy Weitgenant, Matthew Odom, and Paul & Holly Sebahar—who have all recently begun their illustrious careers—I have to thank for all the: discussions (both relevant and otherwise), guidance, suggestions, support, rants, raves, patience, kindness, hiking, fishing, camping, beer, and most importantly, friendship that was given me. This list also includes those friends of mine who are yet to receive their due doctoral distinction, those who have, and those who had the good sense to never embark on that path of insanity in the first place, which includes, but is not limited to: Corey Bloom, John Weber, Ryan Looper, Duane Demong, Wendy Eichel, Dr. Nathan "S.T." Guz, Dr. Brian "Marmot" Brown, Lisa Dysleski, Jory Wendling, Phyllis Weber, Jennifer Weitgenant, Jennifer Odom, Jorin "Jor-lo-lo" Botte, Brian Albrecht, and E. A. "D" Bercot. Thank you all so very much.

To my family for being who they are, and especially for: Andree "Mema" Carlot Teski who's enthusiasm for my achievements cannot be outdone, to all my cousins who were my brothers and sisters growing up, and to the loving memory of my Aunt Brenda Villarreal who showed me how to truly live and enjoy life, you were taken from us too soon.

Last but definitely not least are a few who do not fall into any specific category, but are owed thanks nonetheless: Don Dick, Chris Rithner, Susie Miller, John Chandler, Mike Olsen, Eldon Burk, John Haase, Janet Moder, Kathy Martinolich, Mary Daughtrey,

Morgan Alley, Taylor Reid, all members of the Quantum Mechanics past and present for all the grab-bag beer fun, Dick Odom for the elk hunting and blackberry brandy, Chief Hosa for the incredible skiing conditions, Toy & Roger for keeping me fed with the best damn Thai food I've ever had, all the folks at Big City Burrito, James Beam, Evan Williams, and Mark Makers for keeping my head on straight at times, Bud, Dougan, Lundi, Bernie, and Hunter the best companions we chemists could ever ask for.

This dissertation is dedicated to my parents, David and Pamela Sapp, for their unconditional support and understanding all these years.

TABLE OF CONTENTS

LIST OF ILLUSTRATIONS

Figures:

Tables:

LIST OF ABBREVIATIONS AND SYMBOLS

α	transfer coefficient in electrochemistry
A^{2+}	electron acceptor
ΔAbs	transient absorption of CS
ACN	acetonitrile
ADPN	2,2'-azobis(2,4-dimethylpentanenitrile)
AEPy	*N*-(2-aminoethyl)-2,5-di(2-thienyl)pyrrole
AIBN	2,2'-azobisisobutyronitrile
AOT	Aerosol-OT, bis(2-ethylhexyl)sulfosuccinate
APDTPy	*N*-(4-aminophenyl)-2,5-di(2-thienyl)pyrrole
APPy	*N*-(3-aminopropyl)pyrrole
Au-Av	Extravidin-coated, 10 nm diameter gold particles
Av	avidin
BARF	[tetrakis(3,5-di(trifluoromethyl)phenyl)borate]$^-$
bdb-amd	tris(2,2'-bipyridine-4,4'-bis-(di-*n*-butylamide))cobalt(II) perchlorate
BNHS	D-(+)-biotin-*N*-hydroxysuccinimide
bpy	tris(2,2'-bipyridine)cobalt(II) perchlorate
C^{2+}	$[Ru(L)_3]^{2+}$ type chromophore
3CA-Cl	[bis(1,10-phenanthroline)(4-(1-(1'-methyl-4,4'-bipyridinediium-1-yl)-3-propyl)-4'-methyl-2,2'-bipyridine)ruthenium(II)]$(PF_6)_2(Cl)_2$
3CA-PF_6	[bis(1,10-phenanthroline)(4-(1-(1'-methyl-4,4'-bipyridinediium-1-yl)-3-propyl)-4'-methyl-2,2'-bipyridine)ruthenium(II)]$(PF_6)_4$

3CA-PTZ4S	[bis(1,10-phenanthroline)(4-(1-(1'-methyl-4,4'-bipyridinediium-1-yl)-3-propyl)-4'-methyl-2,2'-bipyridine)ruthenium(II)]$(PF_6)_2$((1-(10-phenothiazinyl)-4-butyl)sulfonate)$_2$
CC	charge-carrier
CD_3CN	deuterated acetonitrile
CD_3OD	deuterated methanol
$CDCl_3$	deuterated chloroform
CD-R	recordable compact disc
CD-RW	recordable, rewritable compact disc
CMC	critical micelle concentration
CP	conducting polymer
CS	charge-separated state
CT	charge-transfer state
CV	cyclic voltammetry
CVs	cyclic voltammograms
D	electron donor
DCE	1,2-dichloroethane
DCM	dichloromethane
DDS	sodium dodecylsulfate
DLS	dynamic light scattering
4,4'-dmb	tris(4,4'-dimethyl-2,2'-bipyridine)cobalt(II) perchlorate
5,5'-dmb	tris(5,5'-dimethyl-2,2'-bipyridine)cobalt(II) perchlorate
DMF	*N,N*-dimethylformamide
dn-bpy	tris(4,4'-dinonyl-2,2'-bipyridine)cobalt(II) perchlorate
dp-bpy	tris(4,4'-diphenyl-2,2'-bipyridine)cobalt(II) perchlorate
d3p-bpy	tris(4,4'-di-(3-pentyl)-2,2'-bipyridine)cobalt(II) perchlorate

DSSC	dye-sensitized solar cell
dtb-bpy	tris(4,4'-di-*t*-butyl-2,2'-bipyridine)cobalt(II) perchlorate
dtb-est	tris(2,2'-bipyridine-4,4'-di-*t*-butoxyester)cobalt(II) perchlorate
DVB	divinylbenzene
ε	molar extinction coefficient
$E_{1/2}$	half-wave potential of the anodic and cathodic peak potentials in electrochemistry
ΔE_p	anodic and cathodic peak separation in electrochemistry
EtOH	ethanol
$Fe(ClO_4)_2 \cdot X\ H_2O$	ferrous perchlorate hydrate
FF	fill factor in solar cell measurements
GBL	γ-butyrolactone
GS	ground state
η	solar cell efficiency
η_{rel}	cobalt(II/III) complex mediated solar cell efficiency relative to the efficiency of a comparable iodide/iodine mediated cell.
^{1}**H NMR**	proton nuclear magnetic resonance spectroscopy
HFIP	1,1,1,3,3,3-hexafluoro-2-propanol
HOMO	highest occupied molecular orbital
I_2	iodine
IPCE	incident photon-to-current conversion efficiency
ITO	tin-doped indium oxide-coated glass; conducting glass
J_{sc}	short circuit photocurrent density
K-BARF	Potassium tetrakis(3,5-di(trifluoromethyl)phenyl)borate
K_{eq}	D,C^{2+} charge-transfer complex formation constant
λ_{max}	maximum absorption or emission wavelength

$LiClO_4$	lithium perchlorate
LiI	lithium iodide
Li-PTZ4S	lithium (1-(10-phenothiazinyl)-4-butyl)sulfonate
LUMO	lowest unoccupied molecular orbital
MeOH	methanol
MLCT	metal-to-ligand charge-transfer state
MPN	3-methoxypropionitrile
N_2	nitrogen gas
N3	*cis*-di(isothiocyanato)-*N,N*-bis(2,2'-bipyridine-4,4'-dicarboxylic acid)-ruthenium(II)
NaOH	sodium hydroxide
Na-PTSA	*para*-toluenesulfonic acid sodium salt
Nd:YAG	neodymium-doped yttrium aluminum garnet
NH_4PF_6	ammonium hexafluorophosphate
NMPTZ	10-methylphenothiazine. *N*-methylphenothiazine
$NOBF_4$	nitrosonium tetrafluoroborate
PD	photodiode
PE	polyester
phen	tris(1,10-phenanthroline)cobalt(II) perchlorate
phen-phen	tris(4,7-diphenyl-1,10-phenanthroline)cobalt(II) perchlorate
PMT	photomultiplier tube
PS-SAv	streptavidin-coated, 900 nm diameter polystyrene latex particles
PTZ	phenothiazine
PTZ3Q	[trimethyl-(1-(10-phenothiazinyl)-3-propyl)ammonium]$^+$
PTZ3Q-BARF	trimethyl-(1-(10-phenothiazinyl)-3-propyl)ammonium tetrakis(3,5-di(trifluoromethyl)phenyl)borate

PTZ3Q-I	trimethyl-(1-(10-phenothiazinyl)-3-propyl)ammonium iodide
PTZ3Q-PF_6	trimethyl-(1-(10-phenothiazinyl)-3-propyl)ammonium hexafluorophosphate
PTZ4S	[(1-(10-phenothiazinyl)-4-butyl)sulfonate]$^-$
RT	room temperature
Rubpy	tris(2,2'-bipyridyl)dichlororuthenium(II)
SAv	streptavidin
SEM	scanning electron microscopy
SHE	standard hydrogen electrode (defined as 0.00 V)
SnO_2:F	fluorine-doped tin oxide-coated glass, transparent conducting electrodes
τ	process lifetime
TBA^+	tetabutylammonium cation
TBA-PF_6	tetrabutylammonium hexafluorophosphate
TEM	transmission electron microscopy
te-terpy	bis(4,4',4"-triethyl-2,2':6',2"-terpyridine)cobalt(II) perchlorate
THF	tetrahydrofuran
TiO_2	titanium dioxide
tm-bpy	tris(4,4',5,5'-tetramethyl-2,2'-bipyridine)cobalt(II) perchlorate
TOA-I	tetraoctylammonium iodide
TOA-PTZ4S	tetraoctylammonium (1-(10-phenothiazinyl)-4-butyl)sulfonate
ttb-terpy	bis(4,4',4"-tri-*t*-butyl-2,2':6',2"-terpyridine)cobalt(II) perchlorate
UV	ultraviolet light
UV-vis	ultraviolet-visible light
V_{oc}	open circuit photovoltage
W_0	the molar ratio of polar solvent to surfactant

FUNDING

Financial support for the work contained in this dissertation was provided in part by (Prof. Charles R. Martin) the National Science Foundation and the Office of Naval Research (CM990001U), by (Prof. C. Michael Elliott) the U.S. Department of Energy - Office of Science (DE-FG03-97ER14808) and the National Science Foundation (CHE-0139637 and CHE-9714081), and by (Prof. Carlo A. Bignozzi) the Ferrara Research Association (F/BGI/BGI/11/01) and the Consortium Spinner (574/01).

Chapter 1.

Self-assembly of template-synthesized micro- and nanostructures using biotin - avidin/streptavidin binding chemistry.

Introduction.

With the current fervor of micro- and nanomaterials research, much of the work is shifting its focus from the fabrication of structures to the assembly of interconnected structures and organized arrays. To this end, there is considerable interest in using chemical interactions to self-assemble particles and structures into organized assemblies on the nanometer to millimeter scale. Natan et al. have used various chemical and biochemical strategies to self-assemble colloidal gold particles onto surfaces.[1,2] Mirkin et al. used thiol linkers to bind colloidal gold particles to single-stranded oligonucleotides; these nanoparticles were subsequently self-assembled into a polymeric network by addition of the complementary oligonucleotide.[3,4] Thiol linkers have also been used to attach gold nanoparticles to Fullerene pipes.[5] Whitesides' research group has used hydrophobic interactions to self-assemble mm-scale objects into a variety of highly organized structures.[6]

Prior to the approaches developed in the course of this research and discussed herein, template-synthesized micro- and nanostructures had not been self-assembled in this way. Template-synthesis is a general and versatile method for preparing micro- and nanomaterials; this method entails synthesizing the desired material within the pores of a micro- or nanoporous template membrane.[7-11] The membranes employed have cylindrical

pores, with monodisperse diameters (nm to microns), that extend through the entire thickness of the membrane. Because of the cylindrical pore geometry, corresponding cylindrical micro- and nanostructures are obtained. These may be high aspect-ratio solid nanowires,[12] hollow nanotubules,[13] smaller aspect-ratio nanoplugs,[14] and even pancake-like nanostructures with aspect ratios less than unity.[15] Micro- and nanostructures of these types composed of metals, semiconductors, conducting polymers, carbons, and other materials have been prepared.[7-11]

These micro- and nanostructures could be useful as building blocks for self-assembly of supramolecular architectures. This research represents the first steps toward using template-synthesized materials in this way. Template-synthesized conducting polymer microwires are self-assembled with commercially available colloidal particles to prepare colloid/wire supramolecular assemblies. The self-assembly chemistry is that of biotin-avidin or biotin-streptavidin binding. Both avidin and streptavidin—hereafter Av and SAv respectively—have four independent binding sites for biotin, each with an affinity constant of ca. 10^{15} M^{-1}.[16-19] This binding chemistry is commonly employed in enzyme-linked immunosorbent assays to bind multiple tagging agents to the targeted antigen.[16,18,19] This approach was chosen because the binding of biotin by Av/SAv is well understood and many reagents—including biotinylating reagents and Av/SAv conjugates—are commercially available.[18]

Figure 1.1 depicts the strategy followed in these studies to employ biotin-Av/SAv binding in self-assembling template-synthesized microstructures and colloids. To make this strategy work, it is necessary to have a chemically functionalized microstructure surface. The amine functionality was chosen because the most commonly used

biotinylating reagent is biotin-*N*-hydroxysuccinimide, which reacts readily with amines to form an amide bond.[18,19] The biotinylated microstructure can then be incubated in a solution/suspension of an Av/SAv conjugate to complete the self-assembly.

Conducting polymer (CP) materials were chosen to carry out this self-assembly strategy because: 1) they are easily deposited in template membranes via electropolymerization, 2) deposition conditions can be altered to achieve either tubules or fibers, and 3) monomers can readily be synthetically functionalized with many different chemical moieties.[20] Another motivation for using these materials is that self-assembling CP fibers with conducting linkers might lead to an interconnected network of microwires with obvious implications for microelectronics applications. There have been a number of amine-functionalized CP monomer structures published in the literature.[21-23] Initially, three of these monomers were synthesized (Figure 1.2) and following polymerization and characterization, polyAEPy was chosen to carry out further studies.

Experimental Section.

Materials. All solvents other than water were purchased from Fisher at spectroscopic grade or better purity. Acetonitrile (ACN) was distilled over calcium hydride prior to use. Toluene and *N,N*-dimethylformamide (DMF) were stored over activated (4Å) molecular sieves prior to use. Distilled water was purified using a Milli-Q® (Millipore) filtration system. Anhydrous lithium perchlorate ($LiClO_4$), sodium sulfate, tin(II) chloride, silver nitrate, tetrabutylammonium perchlorate, tetrabutylammonium hexafluorophosphate, paraformaldehyde, *para*-phenylenediamine, pyrrole, and 1,1,1,3,3,3-hexafluoro-2-propanol (HFIP) at ≥97% purity were purchased from Aldrich and used as received. *N*-(3-aminopropyl)pyrrole (APPY),[23] *N*-(2-

aminoethyl)-2,5-di(2-thienyl)pyrrole (AEPy).[21] and D-(+)-biotin-*N*-hydroxysuccinimide (BNHS)[19] were prepared according to previously described procedures. Oromerse® SO Part B, a gold plating solution (Technic Inc.), a suspension of Extravidin®-coated, 10 nm diameter gold particles (Sigma), and a suspension of streptavidin-coated, 900 nm diameter polystyrene latex particles (Spherotech) were used as received. These two Av/SAv colloidal conjugates will hereafter be referred to as Au-Av and PS-SAv respectively.

Synthesis of *N*-(4-aminophenyl)-2,5-di(2-thienyl)pyrrole (APDTPy). A solution of 1,4-di(2-thienyl)-1,4-butanedione[24] (2.0 g, 8.0 mmol) and *para*-phenylenediamine (4.5 g, 42 mmol) in 80 mL toluene was cooled to 0 °C under nitrogen in a flask equipped with a reflux condenser and addition funnel. The addition funnel was filled with 12 mL of a 0.7 M titanium tetrachloride solution in toluene, which was added dropwise over a 30 minute period to the reaction mixture under vigorous magnetic stirring. This mixture was allowed to warm to room temperature for an hour before bringing the mixture to reflux for 18 hours. The resulting solids were filtered while the reaction mixture was still hot before ice water was added to quench and cool the filtrate. The resulting aqueous phase was extracted and washed three times with ca. 50 ml of toluene. Combining the toluene fractions, drying with sodium sulfate, and rotary evaporating to dryness resulted in a dark green solid. The crude product was recrystallized from ethyl acetate to yield 1.5 g (58%) of light green crystalline solid.

^{1}H NMR (300 MHz, $CDCl_3$) δ ppm: 6.52 (2H, s, 2× pyrrolyl-H), 6.63 (2H, m, 2× thienyl-H), 6.71 (2H, m, 2× phenyl-H), 6.83 (2H, m, 2× thienyl-H), 7.03 (2H, m, 2×

thienyl-H), 7.09 (2H, m, 2× phenyl-H) *an identifiable signal for the amine protons was not observed.*

Electrochemistry. Cyclic voltammetric growth of CPs was carried out in a standard three-electrode cell. The working electrode was a platinum disc (2.8×10^{-2} cm^2). The counter was a 0.5 cm^2 platinum flag, and the reference electrode was a silver wire in a solution of 0.1 M tetrabutylammonium perchlorate and 0.01 M silver nitrate in ACN (0.47 V vs. SHE). Growth solutions were prepared using 0.01 M monomer and 0.1 M lithium perchlorate in ACN.

Spectroelectrochemistry was carried out by constructing a three-electrode cell within the confines of a standard 1 cm path-length quartz cuvette (see Figure 1.3A). The working electrode was a tin-doped indium oxide coated glass slide (ITO) that was positioned in the cuvette so as to be in the beam path of the spectrophotometer. The counter and reference electrodes were a platinum and silver wire, respectively, positioned in the cuvette so as to be out of the beam path of the spectrophotometer. Initially a polymer film was grown on the ITO using a monomer growth solution. This solution was then replaced with monomer-free electrolyte after rinsing the cell and electrodes in ACN. The potential of the ITO-polymer electrode was then controlled and stepped through a range of potentials such that the polymer was observed from its fully oxidized to its fully reduced state. UV-vis spectra were obtained at each potential step.

Template Synthesis. Polyester (PE) track-etched membranes (Poretics) with 1.0, 0.6, or 0.2 micron declared pore diameters were used as template host materials for the fabrication of CP microtubes and microfibers. Micron and sub-micron pore sizes were

used to facilitate the characterization process. Polycarbonate membranes could not be used because they were not compatible with DMF, which is used in a subsequent step.

CP microstructures were deposited by oxidative polymerization of a monomer solution (ACN 0.05 M in monomer and 1.0 M in $LiClO_4$) using a galvanostatic deposition cell that is illustrated in Figure 1.3B. The conducting back-contact on the membrane was made by sputter-coating one side of the membrane with ca. 80 nm of gold. This contact was then used as the working electrode for CP polymerization. After the deposition was complete, any polymer surface layers were removed by polishing with first 1.0 micron and then 0.3 micron alumina powder (Buehler) as a slurry in water. Polishing was then followed by rinsing and sonication. For imaging of free microstructures, the membranes were dissolved in HFIP and residual material was collected on a paper or alumina filter for scanning electron microscopy (SEM) or on a Formvar®-coated, 300 mesh, copper grid (Ted Pella) for transmission electron microscopy (TEM). SEM samples were sputtered with a 10 nm layer of gold to prevent charging.

A gold-polyAEPy microfiber composite was also fabricated in a similar fashion with the exception that a thin gold layer was first deposited within the pores of the PE membranes using an electroless plating technique.[7,8,25] PE membranes with 1.0 micron declared pore sizes were used. Following the deposition of gold, the top surface layer was removed, and the remaining gold surface layer and microtubes acted as the electrode for polyAEPy deposition. This resulted in thin gold tubes filled with polyAEPy which was exposed only at the fiber ends (see Figure 1.4).

Biotin-Av/SAv Derivatization. Microstructures of polyAEPy were biotinylated by immersing the polished membrane in a 1.0 mM solution of BNHS in DMF for one hour. The membrane was then rinsed with fresh DMF and water. Control membranes were also immersed in DMF and rinsed, but no BNHS was present in the treatment.

Self-assembly of colloidal particles to the biotinylated polyAEPy microstructures was carried out by incubation of the membrane-bound structures in commercially prepared, aqueous suspensions of Au-Av or PS-SAv conjugates. The incubation period was typically 18 hours, after which time the membrane was rinsed for 2 hours under a continuous flow of water. Gold-polyAEPy microfiber composites were also treated similarly. The template membrane was removed—prior to biotinylation and incubation with PS-SAv—by placing the membrane surface layer side down onto copper adhesive tape and immersing in HFIP for two hours.

Instrumental. All electrochemistry was carried out on an EG&G PAR model 273 potentiostat/galvanostat. UV-vis spectra were obtained using a Hitachi U-3501 spectrophotometer. SEM was carried out on a Phillips model 505 microscope, and TEM was carried out on a JEOL JEM-2000 EX-II microscope. All sputter-coating was done on an Anatech Ltd. Hummer® model 6.2 or 7 sputtering system employing an appropriate target.

Results and Discussion.

Monomers. The materials requirements imposed by the above self-assembly strategy are: (1) that microstructures can be easily formed via oxidative polymerization of the monomer, and (2) that the structure itself contains available amine groups. Based on synthetic and structural simplicity, APPy was the monomer of choice to begin these

studies. It was obtained in one synthetic step from a commercially available precursor using a literature preparation procedure.[23] However, attempts to study the oxidative polymerization process revealed polymer deposition to be prohibitively slow. Co-polymerization of APPy with pyrrole resulted in faster formation of a polymer film at the electrode surface. However, electrochemical and spectral characterization of the resulting material failed to differentiate it from pure polypyrrole.

At this point it was decided to pursue other amine-functionalized monomers. Both AEPy and APDTPy were obtained in one step from the same precursor, which was synthesized in two steps using a published procedure.[24] In contrast to APPy, both AEPy and APDTPy readily form electrode-supported polymeric films. While there is no data to confirm this, it is quite likely that the failure of APPy and success of AEPy and APDTPy in film formation is due to the amount of steric hindrance to co-planarity between repeat units[22].

Materials Characterization. Figure 1.5 shows the cyclic voltammetric growth of polyAEPy and polyAPDTPy on a platinum disk electrode. The oxidation of both monomers resulted in the deposition of a powdery polymer film on the electrode surface. This is verified by the CV data as an increase in current with each successive scan. The thickness of the deposited film could be controlled with the total anodic charge that was allowed to pass. The initial oxidation process that appears in scan 1 of APDTPy (Figure 1.5B) is attributed to the presence of a minor amount of dimer in the solution. Visual inspection of the films during cycling revealed polyAEPy changes colors between its oxidized and reduced forms. PolyAPDTPy also exhibited a slight color change, but was not as visually noticeable as was the change in polyAEPy.

The spectroelectrochemistry of a film of polyAEPy grown on ITO is shown in Figure 1.6. In the fully reduced form, most of the absorbance is concentrated in the UV, which tails off into the visible. Visually this film appears light brown translucent. As the film is slowly oxidized, a visible absorption band appears, and the film becomes purple-grey opaque. By extrapolating the band-edge of both the UV and visible transitions to zero absorbance, a close approximation of the band structure of the material can be made.[26] In the reduced form, the band-edge is ca. 2.0 eV (see Figure 1.6 dashed line B). This corresponds to the energy gap between the highest occupied molecular orbital (HOMO) band and lowest unoccupied molecular orbital (LUMO) band. Upon oxidation, charge carriers are introduced in the material, which results in the formation of a charge carrier (CC) band whose energy level lies within the HOMO-LUMO gap; in the case of polyAEPy this HOMO-CC energy gap is ca. 1.25 eV (see Figure 1.6 dashed line A).

Attempts to measure the conductivity of oxidized polyAEPy and polyAPDTPy were unsuccessful. When adhesive tape was used to try to remove freestanding films from several electrode surfaces, very little material was transferred to the tape. Generally, the deposit of polymer on the tape was in the form of a low density powder. Inspection under a light microscope confirmed that the powdery domains of CP were discontinuous, and thus could not be used to obtain reliable conductivity measurements.

Template Synthesis. Using the cell depicted in Figure 1.3 polyAEPy and polyAPDTPy were galvanostatically deposited within the pores of PE track-etched membranes. Depending on the amount of charge passed, the deposition process was found to yield either microtubes or microfibers. The SEM micrographs in Figure 1.7 show polyAEPy structures that resulted after polishing and dissolving the membrane (0.6

μm pore diameter) in which the structures were deposited. The sample that was grown using 250 mC cm^{-2} resulted in open-ended microtubes whereas 800 mC cm^{-2} resulted in fully formed microfibers. TEM of these same structures revealed the microtubes to be closed at the end from which polymerization originated (the contact layer side or bottom), but hollow throughout the remainder of the structure and open at the opposite end.

When this process was repeated for polyAPDTPy, SEM micrographs of comparable structures showed very different results. In Figure 1.8 the polyAPDTPy structures appear to have been originally formed as with polyAEPy, however, the structures appear to have been collapsed or in some way deformed. It is speculated that the phenylene moiety pendant to the pyrrolyl nitrogen allows the material to swell in HFIP. During membrane dissolution the structures might swell, but rinsing and drying result in collapse of the structures. This hypothesis was not further explored, and since polyAEPy fulfilled all the materials requirements for the self-assembly strategy (*vide supra*), polyAPDTPy structures were not employed further.

Self-Assembly of Microtubes and Gold Nanoparticles. As a first approach to self-assemby, microtubes of polyAEPy were subjected to biotinylation and incubation with an aqueous suspension of Au-Av. This was accomplished by leaving the microtubes in the template membrane (0.2 μm pore diameter), and simply immersing the membrane-bound structures into the desired solution. After the self-assembly step, the membrane was dissolved and the freed structures were collected for characterization. A control sample was prepared, which was not subjected to the biotinylation step.

Figure 1.9 shows the TEM micrographs of microstructures from the control sample (A) and from biotinylated samples (B-D). PolyAEPy structures appear relatively

translucent in the TEM, while gold particles are opaque and dark. The micrograph of the control sample includes imaging of both ends of the structures. Other than a small amount of residual gold appearing on the closed ends—which comes from the sputtered contact-electrode—there is no evidence that the spherical Au-Av nanoparticles are assembled to either the outside or inside of the control microstructures. The biotinylated structures, however, appear to have a large number of Au-Av particles assembled on both the inside (Figure 1.9C) and outside (Figure 1.9B and D) of their structure.

While this approach successfully demonstrates the use of biotin-avidin binding for self-assembly, the large difference in size between the nanoparticles and microtubes results in a structurally less interesting assembly. If the diameters of the spherical particles and the microtubes were more closely matched in size, the resulting structures would be more practical as building blocks for more complicated architectures.

Self-Assembly of Microfibers and Microspheres. A similar procedure to that used for the self-assembly of microtubes and Au-Av nanoparticles was used to carry out the self-assembly of polyAEPy microfibers with PS-SAv microspheres (see Figure 1.1). Membrane-bound microfibers were then biotinylated and incubated in a suspension of PS-SAv microspheres. The control sample differed only in the absence of biotinylation.

Figure 1.10 shows SEM micrographs of the surface of these membranes at two different magnifications (A and B) along with a comparable image of the control sample (C). The diagonal striations that appear on the membrane surface are a result of the polishing process to remove polyAEPy surface layers. Clearly the pore structures have been filled with polyAEPy in the form of microfibers. The roughness of the polished membrane surface makes it virtually impossible to determine if every attached

microsphere is located atop a microfiber. Furthermore there are likely to be some that are bound to un-removed surface layer polyAEPy. However, in most cases when the SEM is zoomed into the area of a microsphere attachment, a microfiber-filled pore structure can be resolved (see Figure 1.10A). Quantitative analysis of micrograph images like Figure 1.10B give a surface coverage density of 1.3×10^7 microspheres cm^{-2}. This can be compared to a pore density of 3×10^7 pores cm^{-2}, although admittedly the assumption that the PS-SAv microspheres are all attached to microfibers cannot realistically be validated.

Having succeeded at self-assembling comparably sized structures, it was desired to image these fiber-sphere assemblies out of the membrane. However, the PS-SAv microspheres are completely dissolved in HFIP—the only solvent known to be capable of dissolving the PE membrane. The cross-linked analog of PS-SAv was also tried, but the microspheres were so highly swelled by HFIP that it was difficult to identify them after exposure. It was thought that a simple solution to this problem could be to remove the membrane prior to carrying out the self-assembly step. However, there were a number of problems with this strategy that were discovered in exploring this option. First, polyAEPy microfibers were observed to aggregate upon membrane removal. Second, even if biotinylation is carried out with the membrane in place, it is likely that the polyAEPy microfibers are biotinylated along their sides as well as their ends. If this is indeed the case, then self-assembly after membrane removal would result in microsphere attachment to any biotinylated surface—not just the ends, which is the target architecture. What was needed was a rigid shell material that could prevent aggregation of

freestanding polyAEPy microfibers and that could act as a mask to allow microsphere attachment only at the ends.

Cepak et al. have investigated concentric microfiber composites.[25] and the procedures developed to make these materials were adapted to the purposes of a self-assembly strategy (see Figure 1.4). By electrolessly plating a thin microtube of gold and then filling it with polyAEPy, the challenges discussed above were overcome. Figure 1.11 displays the SEM micrographs of the polished membrane surface after gold deposition (A) and after polyAEPy deposition within the gold (B). If the gold and polyAEPy surface-layers are left intact (no polishing) on the bottom side of the membrane, then removal of the membrane results in freestanding microfiber composites of polyAEPy surrounded by gold. These freestanding microfiber composites were subjected to biotinylation and incubation with PS-SAv. The resulting fiber-sphere assemblies were imaged by SEM, and the micrographs in Figure 1.12 A and B show two different samples at similar magnification. Not all of the microspheres are located only on the ends of the microfiber composites, but a large percentage of them are. In all probability the gold-layer is not defect-free, and this could be the cause of self-assembly to the sides of the microfibers.

Conclusions.

While the self-assembled microstructures obtained in these studies are not useful as any type of microscale device, they are impressive because of their size and because of the tendancy of these structures to aggregate in a non-organized manner. That molecular-scale interactions have the ability to direct the self-assembly of structures in the micron size regime is quite remarkable.

This research represents the first efforts to demonstrate the use of the biotin-Av/SAv binding chemistry in the self-assembly of micro- and nanostructures. It is likely that the self-assembly strategies developed in this research will be directly applicable to more advanced structures and assemblies. The next step will be to prepare stable colloidal suspensions of a number of building-block structures—composed of different materials having different electronic and/or optical properties—that when assembled together could form a more complex and more functional assembly.

Chapter 1.

Figures

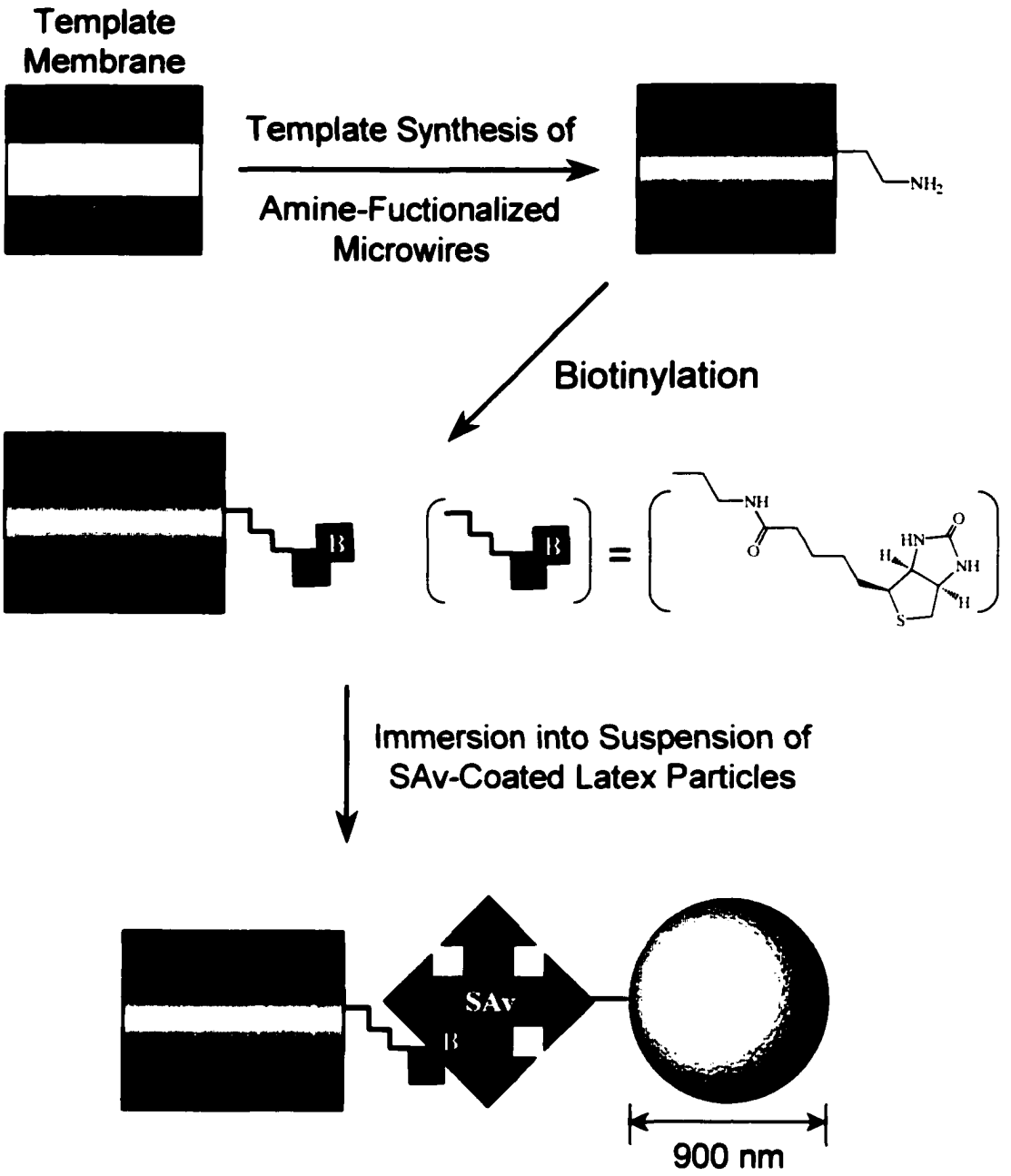

Figure 1.1. Strategy for self-assembly of microstructures and colloids using biotin-Av/SAv binding.

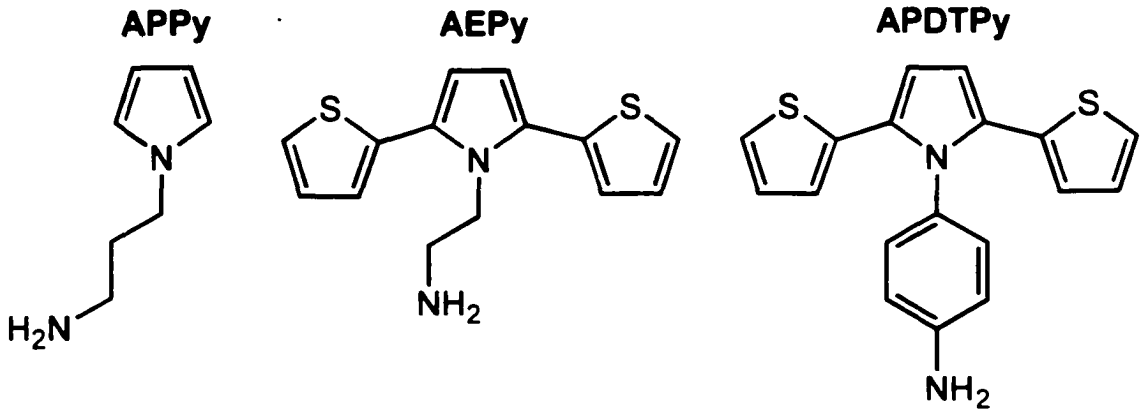

Figure 1.2. Amine-functionalized CP monomer structures.

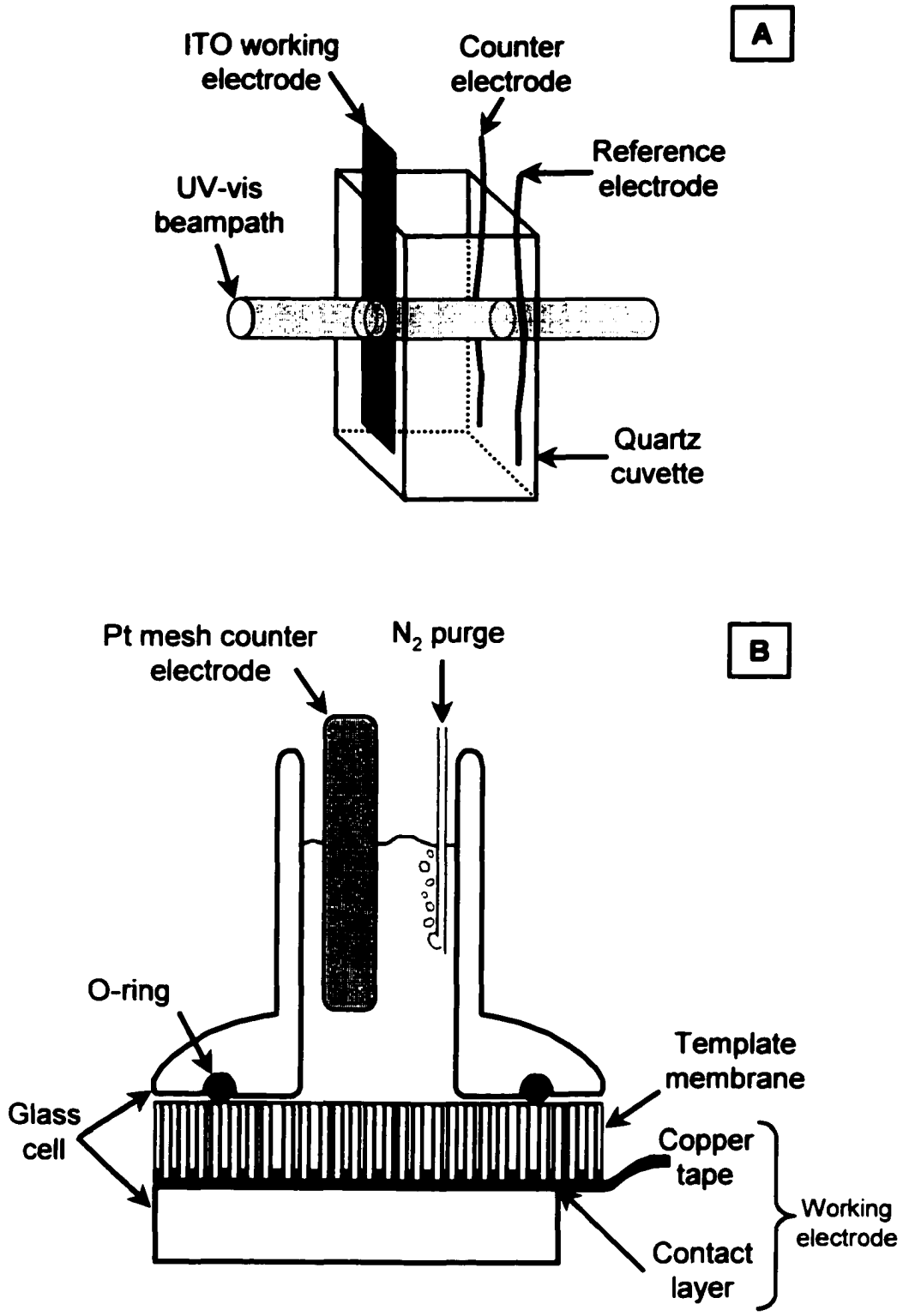

Figure 1.3. Spectroelectrochemistry cell (A) and the electrochemical deposition-based template-synthesis cell (B).

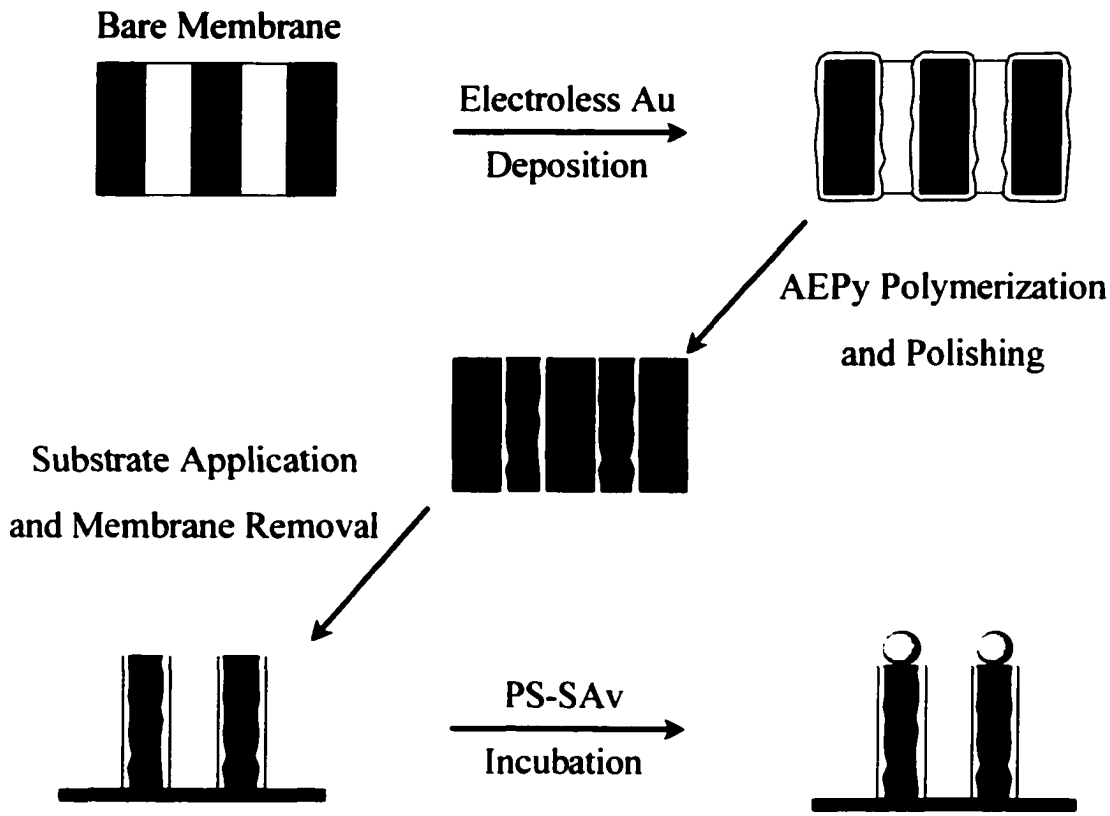

Figure 1.4. Template-synthesis of Au-PolyAEPy concentric microcoposites for freestanding, self-assemblies.

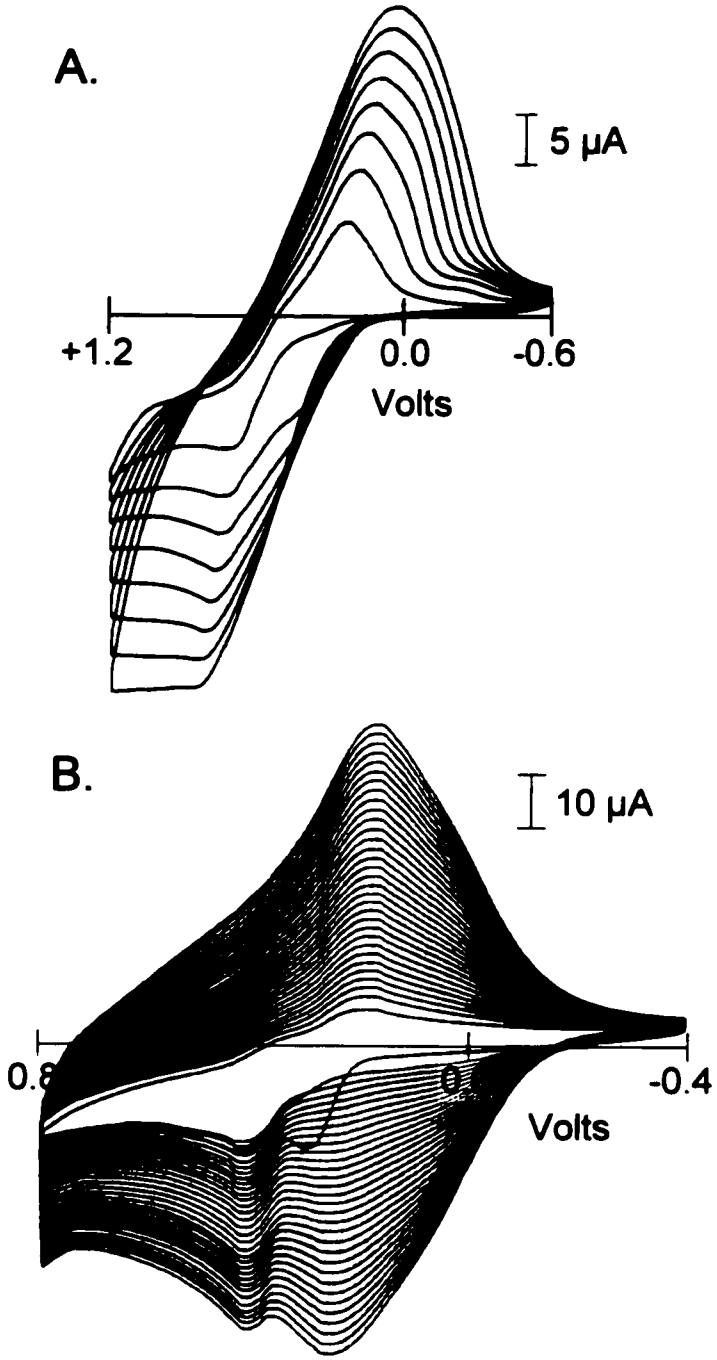

Figure 1.5. CV growth of polyAEPy (A) and polyAPDTPy (B) on a platinum disk electrode (see text for details).

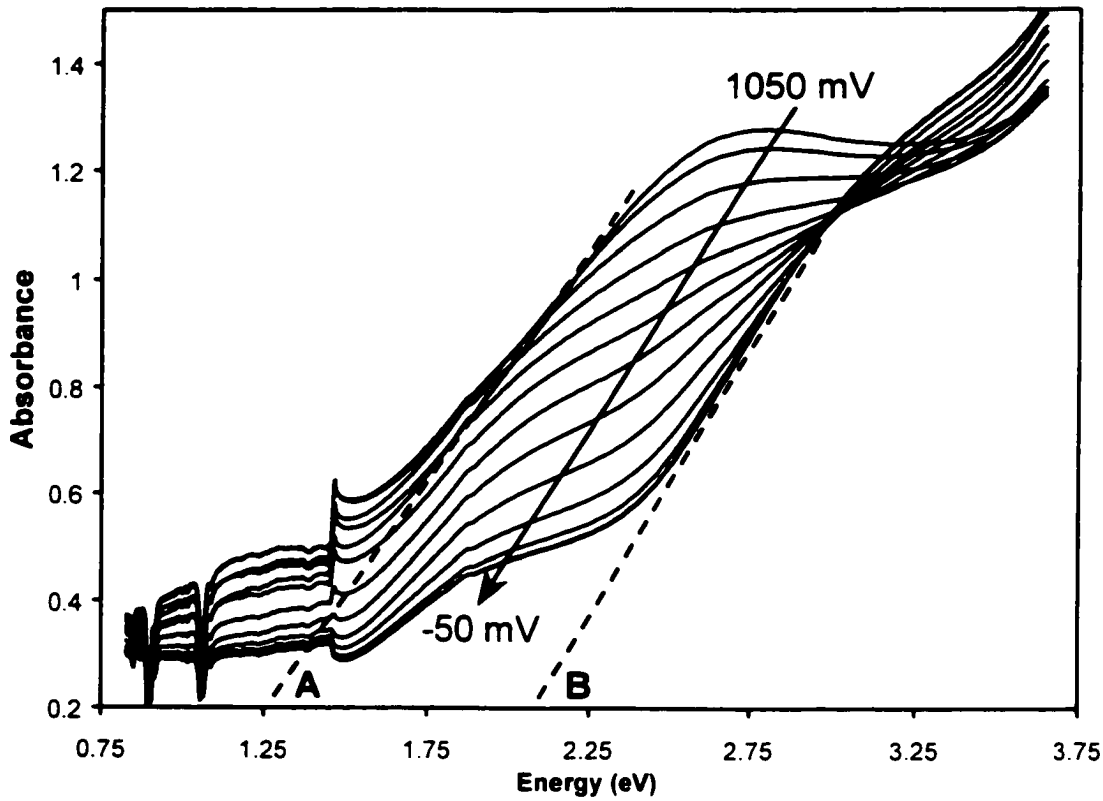

Figure 1.6. Spectroelectrochemistry of polyAEPy from the fully oxidized form (1050 mV) to the fully reduced form (-50 mV). Dashed line A represents the extrapolated energy of the HOMO-CC transition, and dashed line B represents the extrapolated HOMO-LUMO gap energy (see text for details).

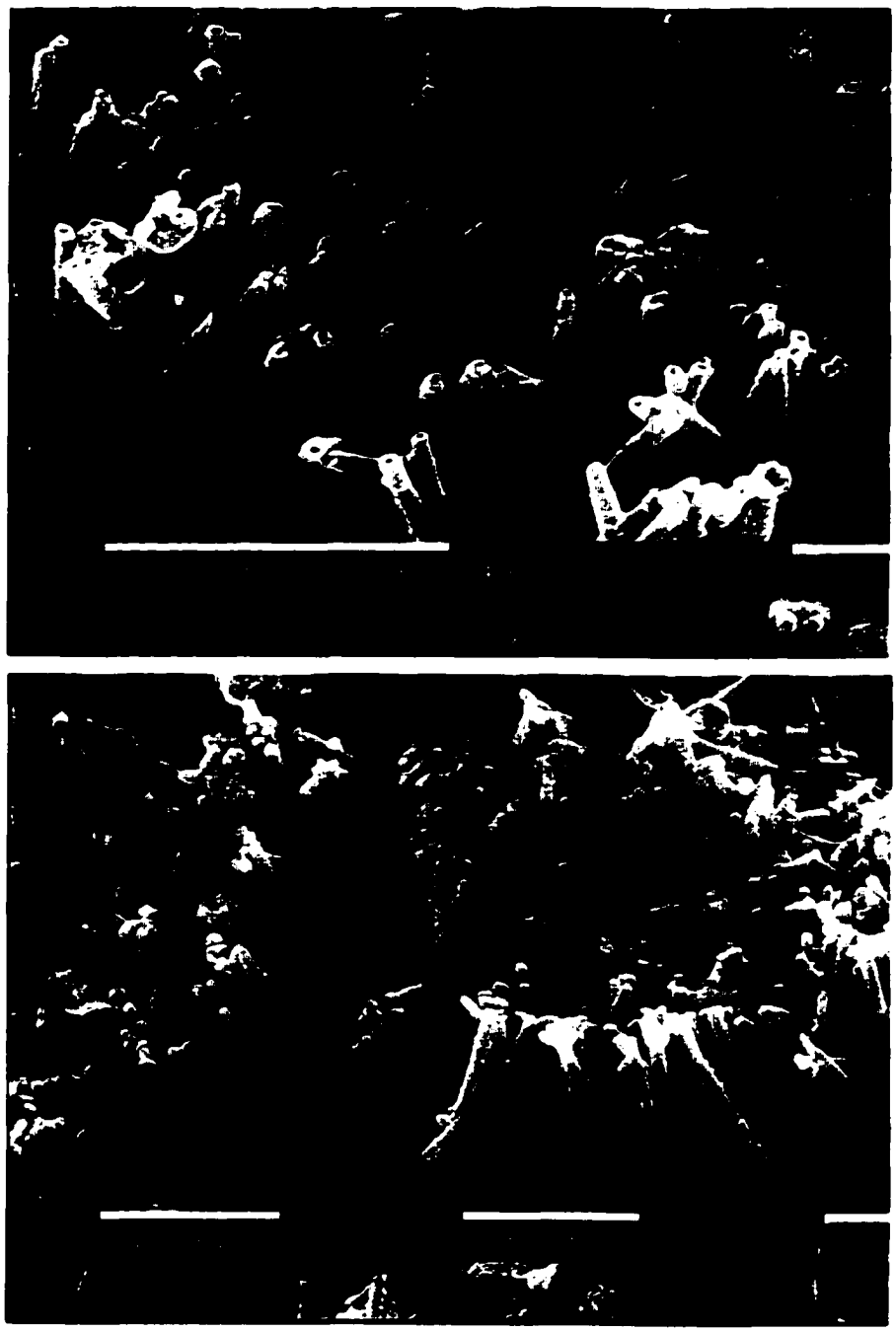

Figure 1.7. SEM micrographs of oxidative polymerization-based template-synthesis of polyAEPy microtubes (A) and microfibers (B). The samples differed in the total charge density that was passed during polymerization: A) 250 mC cm^{-2} and B) 800 mC cm^{-2}.

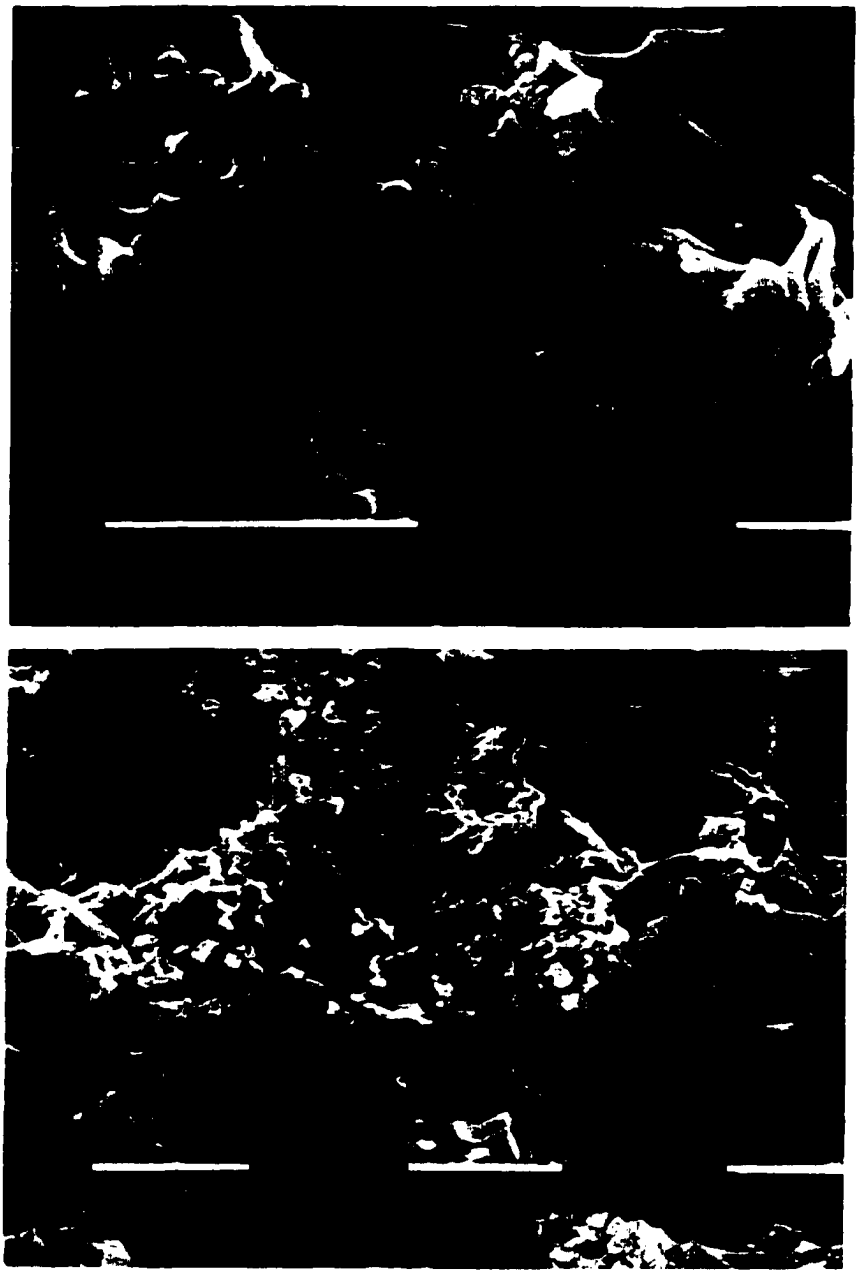

Figure 1.8. SEM micrographs of oxidative polymerization-based template-synthesis of polyAPDTPy microstructures after dissolution of the membrane with HFIP at (A) high magnification and at (B) lower magnification.

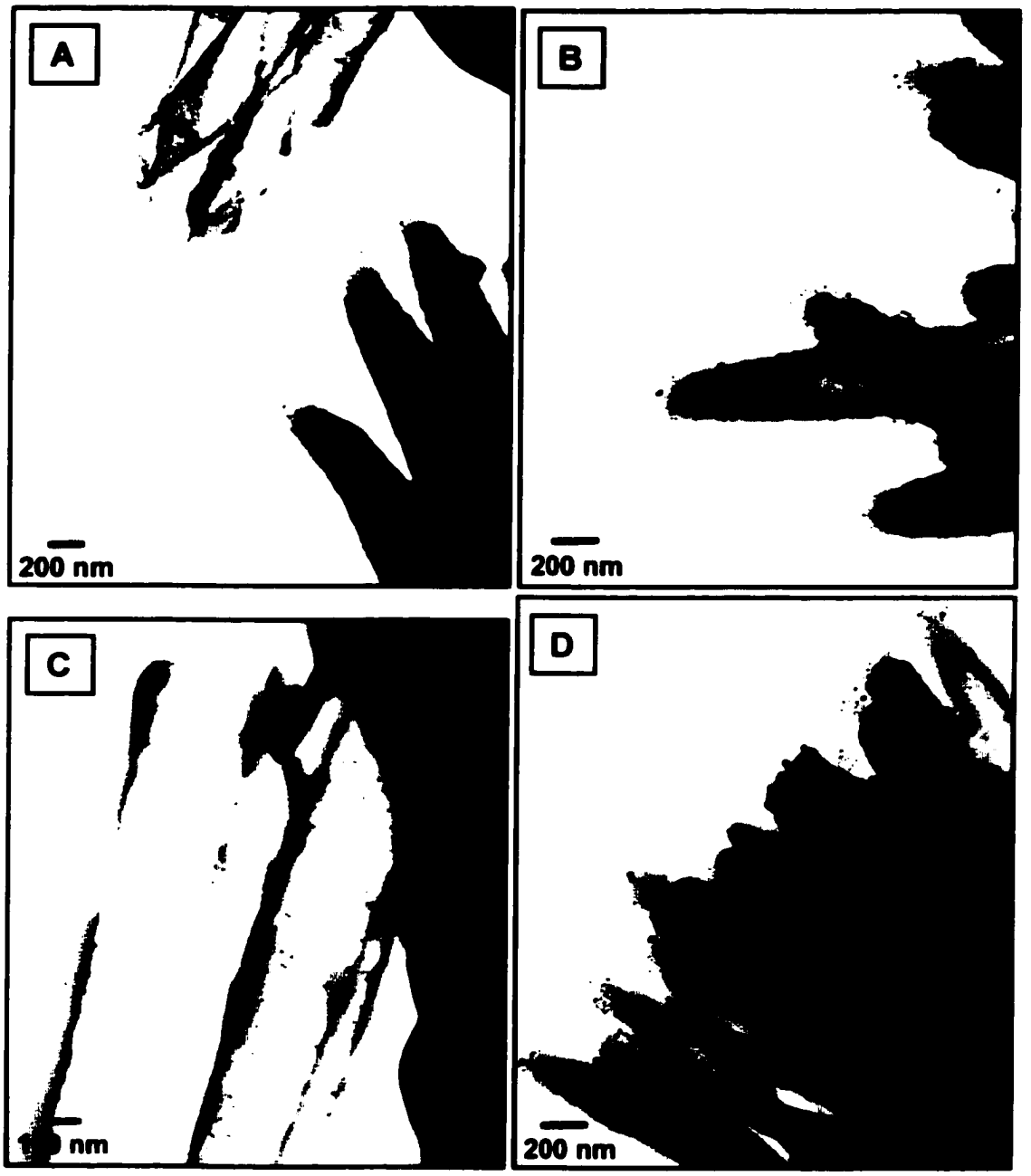

Figure 1.9. TEM micrographs of 0.2 μm diameter polyAEPy microtubes after biotinylation—except for the control sample (A)—and incubation in Au-Av colloidal solution.

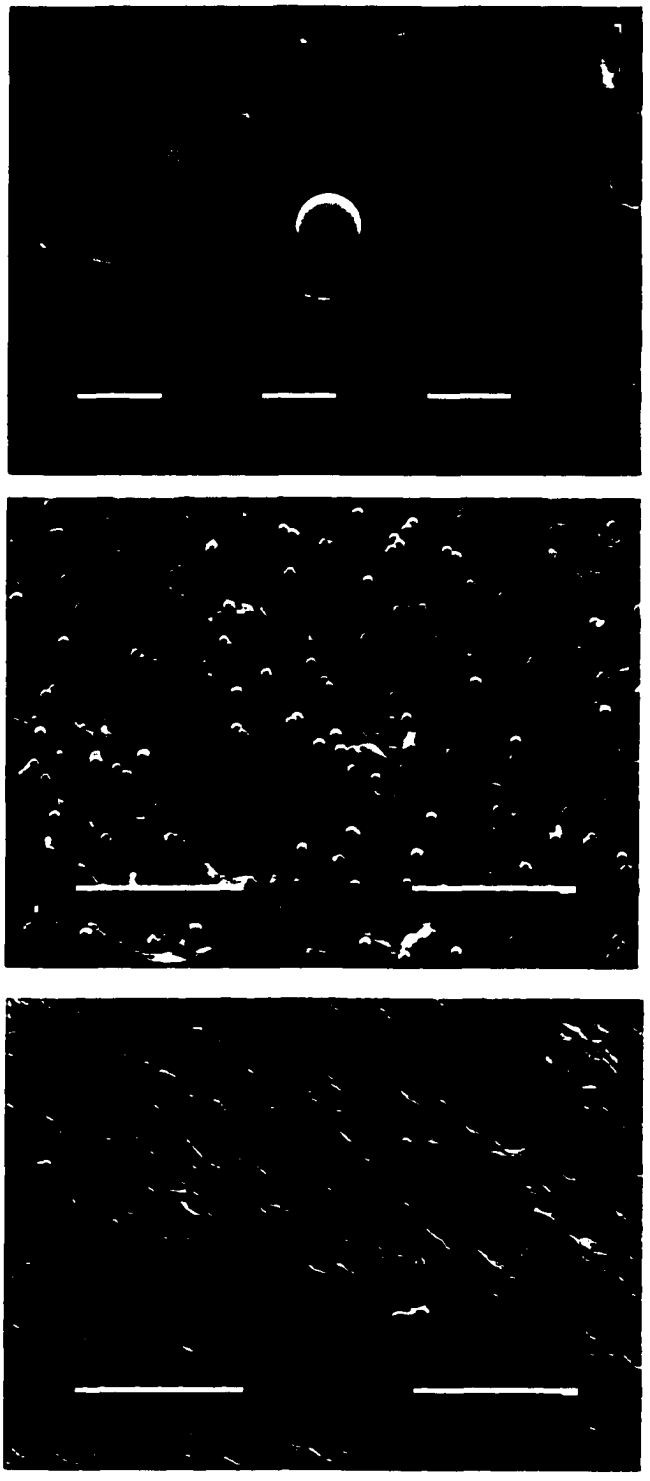

Figure 1.10. SEM micrographs of membrane-bound microfibers (0.6 μm diameter) of polyAEPy after biotinylation and incubation in PS-SAv (A and B). Micrograph C shows the surface of a control membrane that was not biotinylated.

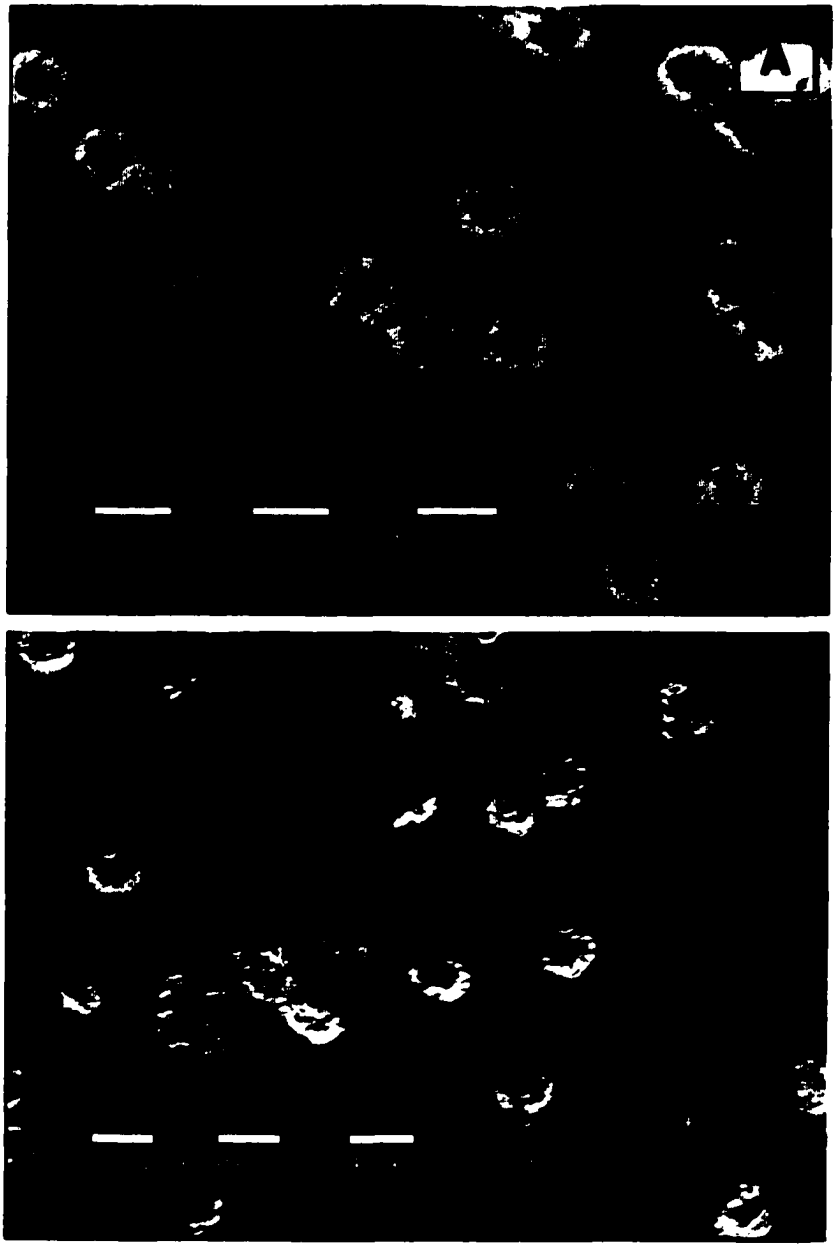

Figure 1.11. SEM micrographs showing the fabrication process of gold-polyAEPy microfiber composites (1.0 μm diameter). First, gold is electrolessly plated to form microtubes (A), then polyAEPy is deposited to fill the hollow of the gold microtubes (B).

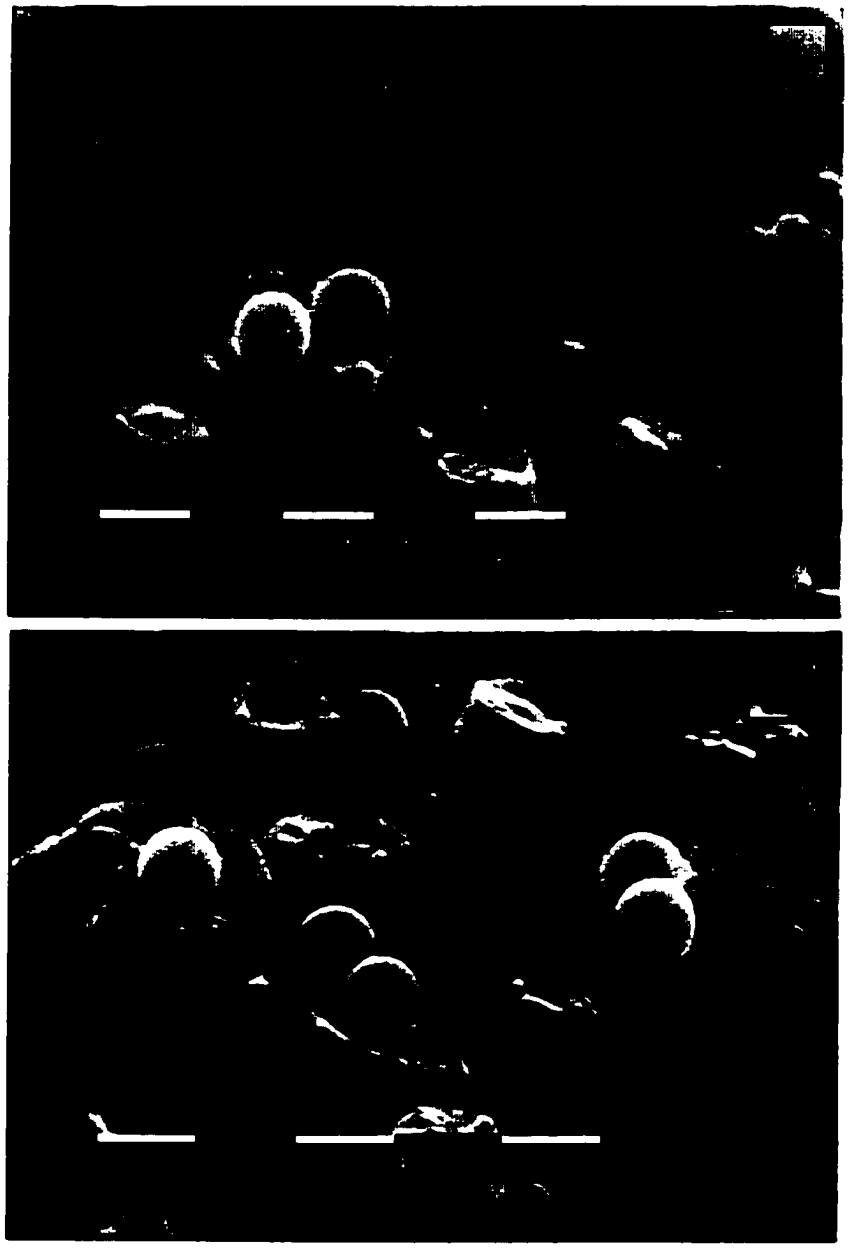

Figure 1.12. SEM micrographs of freestanding assemblies of microfiber composites and PS-SAv microspheres. Micrographs A and B were taken from different samples.

Chapter 1 References:

(1) Freeman, R. G.; Grabar, K. C.; Allison, K. J.; Bright, R. M.; Davis, J. A.; Guthrie, A. P.; Hommer, M. B.; Jackson, M. A.; Smith, P. C.; Walter, D. G.; Natan, M. J. *Science* **1995**, *267*, 1629.

(2) Grabar, K. C.; Freeman, R. G.; Hommer, M. B.; Natan, M. J. *Anal. Chem.* **1995**, *67*, 735.

(3) Elghanian, R.; Storhoff, J. J.; Mucic, R. C.; Letsinger, R. L.; Mirkin, C. A. *Science* **1997**, *277*, 1078.

(4) Mirkin, C. A.; Letsinger, R. L.; Mucic, R. C.; Storhoff, J. J. *Nature* **1996**, *382*, 607.

(5) Liu, J.; Rinzler, A. G.; Dai, H.; Hafner, J. H.; Bradley, R. K.; Boul, P. J.; Lu, A.; Iverson, T.; Shelimov, K.; Huffman, C. B.; Rodriguez-Macias, F.; Shon, Y.-S.; Lee, T. R.; Colbert, D. T.; Smalley, R. E. *Science* **1998**, *280*, 1253.

(6) Bowden, N.; Terfort, A.; Carbeck, J.; Whitesides, G. M. *Science* **1997**, *276*, 233.

(7) Martin, C. R. *Science* **1994**, *266*, 1961.

(8) Martin, C. R. *Chem. Mater.* **1996**, *8*, 1739.

(9) Marinakos, S. M.; Brousseau, L. C., III; Jones, A.; Feldheim, D. L. *Chem. Mater.* **1998**, *10*, 1214.

(10) Schönenberger, C.; van-der-Zande, B. M. I.; Fokkink, L. G. J.; Henry, M.; Schmide, C.; Krüger, M.; Bachtold, A.; Huber, R.; Birk, H.; Staufer, U. *J. Phys. Chem. B* **1997**, *101*, 5497.

(11) Routkevitch, D.; Tager, A. A.; Haruyama, J.; Almawlawi, D.; Moskovits, M.; Xu, J. M. *IEEE Trans. Electr. Dev.* **1996**, *43*, 1646.

(12) Menon, V. P.; Martin, C. R. *Anal. Chem.* **1995**, *67*, 1920.

(13) Jirage, K. B.; Hulteen, J. C.; Martin, C. R. *Science* **1997**, *278*, 655.

(14) Cepak, V. M.; Martin, C. R. *J. Phys. Chem. B* **1998**, *102*, 9985.

(15) Hornyak, G. L.; Martin, C. R. *Thin Solid Films* **1997**, *303*, 84.

(16) Hnatowich, D. J.; Virzi, F.; Rusckowski, M. *J. Nucl. Med.* **1987**, *28*, 1294.

(17) Dontha, N.; Nowall, W. B.; Kuhr, W. G. *Anal. Chem.* **1997**, *69*, 2619.

(18) Bayer, E. A.; Wilchek, M. "Avidin-Biotin Technology". In *Methods In Enzymology*: Academic Press Inc., **1990**; Vol. 184; p. 49-160.

(19) Bayer, E. A.; Skutelsky, E.; Wilchek, M. "The avidin-biotin complex in affinity cytochemistry". In *Methods In Enzymology*: Academic Press Inc., **1979**; Vol. 62; p. 312.

(20) Parthasarathy, R. V.; Martin, C. R. *J. Appl. Polym. Sci.* **1996**, *62*, 875.

(21) Röckel, H.; Huber, J.; Gleiter, R.; Schuhmann, W. *Adv. Mater.* **1994**, *6*, 568.

(22) Torres-Rodriguez, L. M.; Roget, A.; Billon, M.; Bidan, G.; Livache, T. *Chem. Comm.* **1998**, *18*, 1993.

(23) Yon-Hin, B. F. Y.; Smolander, M.; Crompton, T.; Lowe, C. R. *Anal. Chem.* **1993**, *65*, 2067.

(24) Wynberg, H.; Metselaar, J. *Synth. Commun.* **1984**, *14*, 1.

(25) Cepak, V. M.; Hulteen, J. C.; Che, G.; Jirage, K. B.; Lakshmi, B. B.; Fisher, E. R.; Martin, C. R.; Yoneyama, H. *Chem. Mater.* **1997**, *9*, 1065.

(26) Sotzing, G. A.; Reynolds, J. R.; Steel, P. J. *Chem. Mat.* **1996**, *8*, 882.

Chapter 2.

Solid solutions: polymer-encapsulated reverse micelles containing dye solutions.

Introduction.

The development of optical memory elements and sensors can be limited by advances in photo-responsive molecules or dyes. The realization of CD-R and CD-RW technology was brought about primarily by the discovery of a set of dyes that fit the optical and materials requirements for the application.[1-3] However, many dyes are discovered that have excellent switching or sensing capabilities in solution, but cannot be incorporated into a solid-state device because the dye's photophysics differ greatly between solution and the solid-state. This is often true because intramolecular motions or spatial rearrangements are involved in the dye's response to some external stimulus. This degree of freedom for molecular motions is only afforded by a fluid environment. For this reason it is desirable to develop a solid-state material in which a dye solution is encapsulated. Ideally, this material would be of optical quality—not light scattering—and exhibit photophysical properties identical to that of the same dye in solution.

The goal of this research is the development of just such a material. The Elliott group has studied a wide range of synthetic dye systems based on polypyridine complexes of ruthenium(II).[4-9] Solutions of a number of these dyes have shown dramatic optical changes in response to relatively weak magnetic fields, and as such, have great potential as optical-magnetic sensors.[10] However, the photophysical processes responsible for the

magnetic field sensitivity involve a large degree of intramolecular motion.[11,12] Simply freezing dye molecules of this type in a glassy polymer results in dramatically different photophysical properties exhibited by these dyes.[12] In fact, it has been shown that the fluorescence lifetime of a related dye—tris(2,2'-bipyridyl)dichloro-ruthenium(II) (Rubpy)—varies from 0.6 μs to 5 μs between a solution and solid-state environment, respectively.[13] This sensitivity of Rubpy to its environment was used as a probe to determine the dye environment within the materials synthesized herein.

To avoid the complications posed by a true solid, the material developed in this study contains both a solid and a liquid phase. The major phase is made up of a continuous cross-linked polystyrene network. Polystyrene was chosen because it is not highly absorbing in the visible region of the spectrum, it has excellent barrier properties to prevent oxygen gas permeation, and styrene is a sufficiently non-polar monomer to phase separate from a number of polar solvents.[14] The minor phase consists of discreet domains of polar solvent containing Rubpy dye. Assuming the refractive indices of the two phases are quite different, the size of the polar solvent domains must be less than ca. 300 nm to avoid light scattering.[15] To ensure the proper formation of liquid domains of appropriate size, a reverse micelle-forming surfactant has been used in this study to direct the phase segregation. This materials synthesis strategy is depicted in Figure 2.1.

The surfactant, sodium bis(2-ethylhexyl)sulfosuccinate, also known as Aerosol-OT (AOT), has been well studied and is known to form spherical aggregates known as reverse micelles when dissolved in a number of non-polar solvents.[16] Figure 2.2 shows the structure of AOT along with a schematic representation of a reverse micelle. The minimum concentration of AOT at which these structures are formed—the critical

micelle concentration (CMC)—depends on the solvent, but is generally in the 10^{-4} M range.[16] Concentrations of AOT well above the CMC are capable of sequestering water and a few other polar solvents in the ionic interior of the reverse micelle. In many cases, the size of the reverse micelle structure is directly proportional to the molar ratio of water to AOT (W_0), and the diameter of structures ranges from a few nanometers to tens of nanometers.[17]

Zhu et al. used AOT and water to form reverse micelles in styrene-divinylbenzene mixtures.[18-21] They found that by varying W_0, the reverse micelle size imprinted a porosity into the material that was easily controlled. UV-initiated radical polymerization resulted in highly cross-linked polymer solids which were finely ground and washed. Characterization of the powders revealed a pore volume that scaled proportionally with W_0. The stated purpose of these materials was as gel permeation chromatography column materials, and as such, no mention was made of the optical properties of the materials. Nonetheless, this work provided an excellent starting point for the development of the materials in this study. An adaptation of this procedure was used to obtain solid-state materials exhibiting the photophysical properties of the corresponding dye solutions. This adaptation involved the thermal-initiated radical polymerization of styrene and divinylbenzene to encapsulate reverse micelles containing dye solutions.

Experimental Section.

Materials. All solvents other than deionized water were purchased from Fisher at spectroscopic grade or better purity. Activated neutral alumina, sodium dodecylsulfate (DDS), sodium bis(2-ethylhexyl)sulfosuccinate (AOT), tris(2,2'-bipyridyl)dichloro-ruthenium(II) hexahydrate (Rubpy), 2,2'-azobisisobutyronitrile (AIBN), styrene, and

divinylbenzene at ≥97% purity were purchased from Aldrich and used as received. 2,2'-azobis(2,4-dimethylpentanenitrile) (ADPN) was kindly donated by Professor Marc M. Greenberg.

Monomer and Dye Solution Preparation. Both styrene and divinylbenzene (DVB) were inhibited with ca. 10 ppm of 4-*tert*-butylcatechol as received. Just prior to use, the inhibitor was removed using a short column of Dehibit-100 (Polysciences Inc.) followed by a short column of alumina. The freshly "dehibited" styrene and DVB were mixed in a 2:1 volume ratio in a 5 mL glass vial, and the surfactant AOT was added to a concentration of 50 mM. A dye solution of 15 mM Rubpy in either water or formamide was injected via microliter syringe in varying amounts (2-36 μL) to the surfactant-containing monomer mixture (typically 2 mL). As a final component, ca. 1% by weight radical initiator (either AIBN or ADPN) was added to the mixture. Samples prepared in this way were degassed with dry nitrogen and vigorously stirred for ca. 10 minutes on a Vari-Whirl® mixer (VWR).

Reverse Micelle Analysis. Dynamic light scattering (DLS) was used to measure the size of the reverse micelles formed in the above solutions. The radical initiator was left out of the solution until after the measurements were taken. All samples were filtered into the sample cuvette to remove interfering particulate matter. The filtration was accomplished using a 250 μL syringe equipped with a Teflon®-housed 0.02 μm Anodisc® 13 membrane (Whatman).

Polymerization. Thermal initiation of polymerization was carried out using a variac-controlled heating mantle filled with sand and monitored by mercury thermometer. This apparatus was brought to the desired temperature prior to sample introduction. The

polymerization temperature for samples containing AIBN was 60-65 °C. The polymerization temperature for samples containing ADPN was 35-37 °C. All samples were cured for a minimum of 48 hours at the above temperatures. The resulting polymeric monoliths were removed by carefully breaking the glass vial in which they were contained. These monoliths were cylindrical in shape, but grinding and polishing afforded flat orthogonal surfaces of high quality for optical measurements.

Fluorescence Lifetime Measurements. The lifetime of fluorescent emission from Rubpy contained within polymer-encapsulated reverse micelles was measured on the instrument depicted in Figure 2.3. The frequency-tripled output of a Spectra-Physics LAB-190 Nd:YAG laser produced a train of ca. 8 ns pulses at 30 Hz and ca. 1.5 W of power. This output pumped a methanolic solution of Coumarin 450 (Exciton) dye in a Spectra-Physics PDL-3 dye laser. The typical output from the dye laser was a corresponding train of pulses ca. 50 mW in power at 450 nm.

The excitation beam was directed onto the sample—a quartz cuvette containing a solution or a shaped and polished monolith—parallel to the surface normal of one face. The fluorescence emission was collected from a face with a surface-normal orthogonal to the excitation beam. This emission was collimated and focused through an appropriate cut-off filter onto the entrance slit of a Jarrell Ash model 82-410 monochromator set to pass 600 nm light. The light that exited the monochromator was detected with a Hamamatsu model R2496 photomultiplier tube operated at ca. 500 V.

The output from the photomultiplier tube was sent to a Tektronix TDS 620B digital oscilloscope. A Thorlabs DET210 fast photodiode monitoring scattered laser light was used to trigger the oscilloscope. Signal averaging of 200 sets of decay curves was used to

improve signal-to-noise levels. The output from the oscilloscope was saved to disc as x-y data pairs in ASCII format. Using a computer running Microsoft Windows® XP, this data was organized and truncated in Microsoft Excel®; graphical and single-exponential regression analysis was carried out in SigmaPlot® version 2000.

Instrumental. A Nikon OPTIPHOT-POL model light microscope was used for visual inspection and measurement of samples. A DynaPro® molecular sizing instrument (Protein Solutions, Inc.) was used to obtain DLS data for the determination of reverse micelle size in solution. Thin sectioning of polymeric samples was accomplished with a Reichert Ultracut E ultramicrotome using a freshly made glass knife. Transmission electron microscopy (TEM) was carried out on a JEOL JEM-2000 EX-II microscope. Shaping and polishing of samples was accomplished on a Buehler variable-speed polishing wheel with a variety of abrasive surfaces. Fluorescence emission spectra were obtained using a Horiba Fluorolog-3 spectrofluorometer.

Results and Discussion.

Solid Emulsions. Prior to discovering the work of Zhu et al., the approach that was taken to obtain polymeric solids containing encapsulated domains of dye solutions was rather crude and resulted in solid emulsions. These materials were made by 60 °C curing of a solution of dehibited styrene, DDS 5-10% by weight, AIBN 1% by weight, and ca. 10-50 μL (per 1 ml of monomer) of aqueous Rubpy solution. In all cases, the dye solution was phase separated from the monomer, but rapid mixing resulted in the formation of an emulsion. This emulsion was stable enough that the polymerization process was able to encapsulate it. Visual inspection of the resulting monoliths under a light microscope showed they contained spherical droplets of dye solution that ranged in

size from a few millimeters to a few hundred microns (see Figure 2.4). As a consequence of the size of these domains, these monoliths were highly light scattering. Since one of the objectives of this research was the synthesis of an optical quality material, this approach was abandoned.

With the knowledge that encapsulated structures would need to be less than ca. 300 nm to avoid the light scattering problem, a search was conducted to find either polymeric and/or surfactant-based structures that fit this requirement, and could be extended to encapsulate a polar dye solution. The reverse micelle is a highly studied structure that fulfills the size requirement and has a polar interior to accommodate a dye solution (*vide supra*).

AOT-Monomer Solutions. Reverse micellar structures formed from AOT and water are usually studied in aliphatic, non-polar solvents such as isooctane.[16,17] Despite the foreknowledge of the work of Zhu et al, it was necessary to confirm that reverse micelle structures could be formed in styrene/DVB mixtures. To test this and to test formamide as an alternative polar solvent, samples were prepared in which 8 μL of either polar solvent was injected into 2 mL of AOT-containing styrene/DVB. The initial injected volume of polar solvent phase separates from the monomer, but after mixing, the solution becomes completely transparent—a good indication that reverse micelles have formed.

Figure 2.5 shows the raw data that is obtained from the DLS sizing instrument for the above samples. Ten data samplings were obtained for each solution. The horizontal error bars represent the range of sizes of all observed particles within the sampling time frame. The data points themselves are simply the median values of this range. The

proper way to interpret or apply this data was not completely clear, so the average of all median data points was taken as the average measured radius.

Treating the DLS data in this way, a number of other samples were prepared in which W_0 was varied and the average radius determined. Figure 2.6 shows the two plots for samples containing water or formamide. The average radius is plotted as a function of W_0 for each set of samples. Although the relationship between size and W_0 does not appear to be linear, there is clearly a trend of increasing size with added polar solvent. This "non-ideal" behavior has been observed both with non-aliphatic solvents—like benzene and toluene—as the major phase and with polar solvents other than water in the minor phase.[16,17] Nonetheless, this data confirms the formation of reverse micelles using water or formamide as the minor phase in AOT-styrene/DVB solutions.

Polymerization Conditions. The thermal decomposition kinetics of AIBN make it necessary to run a radical initiation reaction at temperatures above 40 °C.[14] Temperatures of 60-70 °C are commonly employed in many thermally initiated radical polymerizations.[14] Thermal initiation was employed in these studies because it requires no special UV-exposure apparatus. Samples can simply be prepared in standard glass vials, heat-cured, and removed. However, all attempts to encapsulate reverse micelles under standard AIBN initiated conditions failed. The polymer monoliths that resulted were very light scattering and opaque.

Conversations with Professor Nancy E. Levinger—here at Colorado State University's Chemistry Department—and a review of the literature[16] revealed an upper limit to the thermal stability of reverse micelle structures at ca. 40 °C. At 60 °C the thermal motion and the resulting turbulence of the major phase disrupts the formation of

reverse micelle aggregates. Below 40 °C these systems are certainly dynamic, but solvent collisions are not sufficiently energetic to be disruptive. It has been estimated that for inter-aggregate collisions at 25 °C, only one event out of one thousand results in an exchange of matter from the core of the reverse micelle aggregates.[16]

AIBN is not an effective initiator below 40 °C, but there are many related azo-initiators that are effective over a wide range of temperatures. ADPN is structurally similar to AIBN, but is an effective initiator at 35 °C. It was found that polymerizations run below 40 °C using ADPN as the radical initiator resulted in polymer monoliths that were transparent and identical to the appearance of the starting monomer solution. All subsequent polymeric samples employed in the following research were prepared using ADPN as the initiator.

Monolith Characterization. TEM was used in an attempt to visualize the pore structure of polymer monoliths. Ultramicrotome sections of ca. 100 nm thickness were obtained, but these sections proved to be too thick to obtain images at the magnification necessary to resolve individual reverse micelle-imprinted pores. The best micrograph image obtained was taken in a very thin portion of a cut section, and is shown in Figure 2.7. Clearly, the resolution of this micrograph is insufficient to identify any structural characteristics attributable to the presence of reverse micelles. However, there does appear to be a texture variation in the thinnest part of this sample that is in the size range of the reverse micelles (Figure 2.7A and B), but these features could be attributed to knife artifacts, electron beam noise, or film grain.

The results of this TEM study were inconclusive. Further efforts were abandoned due to the difficult and time-consuming nature of ultra-microtomy. An alternative approach

that was not explored but could have been used is the freeze fracturing of monoliths followed by the sputtering of a platinum-carbon surface replica. TEM could then be used to image the replica, assuming that it could be freed from the surface.

Fluorescence Spectroscopy. Figure 2.8 contains the emission spectra from two sets of monoliths: one containing aqueous Rubpy (top graph) inside the reverse micelles, and the other containing formamide-Rubpy (bottom graph). The samples within each set differed in W_0, and thus contained increasing amounts of Rubpy as W_0 increased. However, the irreproducible placement of samples in the spectrofluorometer resulted in a large degree of variance in the peak intensity for each sample. To simplify visual comparison of spectra, each set of data was normalized at its peak intensity (λ_{max}). Basically, the emission characteristics of these samples—a single broad emission band with a lack of fine structure—indicate a solution environment for the dye in both water and formamide.[13] Water-containing samples show almost no spectral changes—λ_{max} varies by at most 6 nm—as a function of W_0; whereas formamide-containing samples show a very clear redshift of 20 nm with W_0 values between 0.44 and 5.2.

Fluorescence Lifetime. The fluorescence lifetime of Rubpy in solutions encapsulated by reverse micelles was measured and used as semi-quantitative indicator of the nature of the environment surrounding the dye—this lifetime being a few hundred nanoseconds in solution and a few microseconds in solid (*vide supra*). It is also known that the fluorescence of Rubpy decays with a single exponential in solution and a multi-exponential in the solid-state.[22] In the data that follows, all decay curves fit well ($R^2 \geq 0.95$) to a single exponential. Figure 2.9 shows the fluorescence lifetime data obtained as a function of W_0 for both water (top graph) and formamide (bottom graph) as the polar

solvent. To determine the effect of polymerization, data was obtained, both prior to and after polymerization for each sample. As a basis for comparison, the fluorescence lifetime was also measured in bulk water and formamide; this value is represented in the respective graphs as a dashed line.

When water is used as the polar solvent, the monomer solutions exhibit a fluorescence lifetime that is within ca. 60 ns of the lifetime measured in bulk water. This is true irrespective of the W_0 value of the sample—within the measured range. After polymerization, this lifetime increases to ca. 1.15 μs, and again is relatively invariable as a function of W_0. This data suggests two things: (1) the chemical environment surrounding the dye is relatively unchanged by the addition of more dye solution (i.e. larger reverse micelles), and (2) polymerization results in a longer lived excited-state (by ca. 800 ns) indicating a chemical environment intermediate between solution and solid.

Monomer solutions and polymeric solids containing formamide dye solutions exhibited somewhat different characteristics. Monomer solutions again exhibited fluorescence lifetimes close to the lifetime measured in bulk formamide. However, there appears to be a trend in which the lifetime increases and approaches the bulk solvent value as a function of W_0. Again, polymerization results in an approximately 800 ns increase in the lifetime. However, as W_0 increases, the lifetime decreases and approaches to within ca. 110 ns of the bulk solvent value. For both monomeric and polymeric samples this data suggests that, as the reverse micelle's size increases, the chemical environment surrounding the dye becomes increasingly similar to bulk solvent conditions.

The results obtained with water-containing samples cannot be completely explained (nor are they presently understood). In contrast, the results from formamide-containing samples are more intuitive, in that the dye's environment approaches bulk solvent properties as the reverse micelles increase in size. Notwithstanding even the less intuitive results, both sets of materials exhibit characteristics that fulfill the requirements established at the outset of this research. Figure 2.10 shows photographs of the series of water-containing monoliths under normal (A) and UV (B) illumination. These photographs clearly demonstrate the excellent optical quality of the materials developed in this study.

Conclusions.

The primary objective of this research was the development of a solid optical material incorporating a dye whose photophysical properties correspond to the dye in a fluid environment. This was achieved through the polymer encapsulation of reverse micelles containing dye solutions. AOT-monomer solutions were found to form stable reverse micelle aggregates with the addition of water or formamide as a polar solvent. These aggregates were stable below ca. 40 °C, and polymerizations carried out below this temperature resulted in highly transparent polymer monoliths.

The fluorescence spectra and lifetime of emission—of Rubpy in polar solvent containing reverse micelles—was used as a measure of the chemical environment within the micellar aggregates. Emission spectra of monolithic samples indicated a solution environment for the dye. The observed emission lifetime values differed before and after polymerization of the samples, but the results also indicated a solution environment

surrounding the dye in formamide (for $W_0 > 3$), and an environment intermediate between solution and solid with water.

While no optically responsive dyes were used in these studies, their incorporation into these materials should be straightforward. Dyes exhibiting sensor or memory capabilities in solution but not in the solid-state could now be investigated for use in solid-state applications. These materials combine the freedom of motion afforded by a solution environment, with the advantages of a solid polymer material.

Chapter 2.

Figures

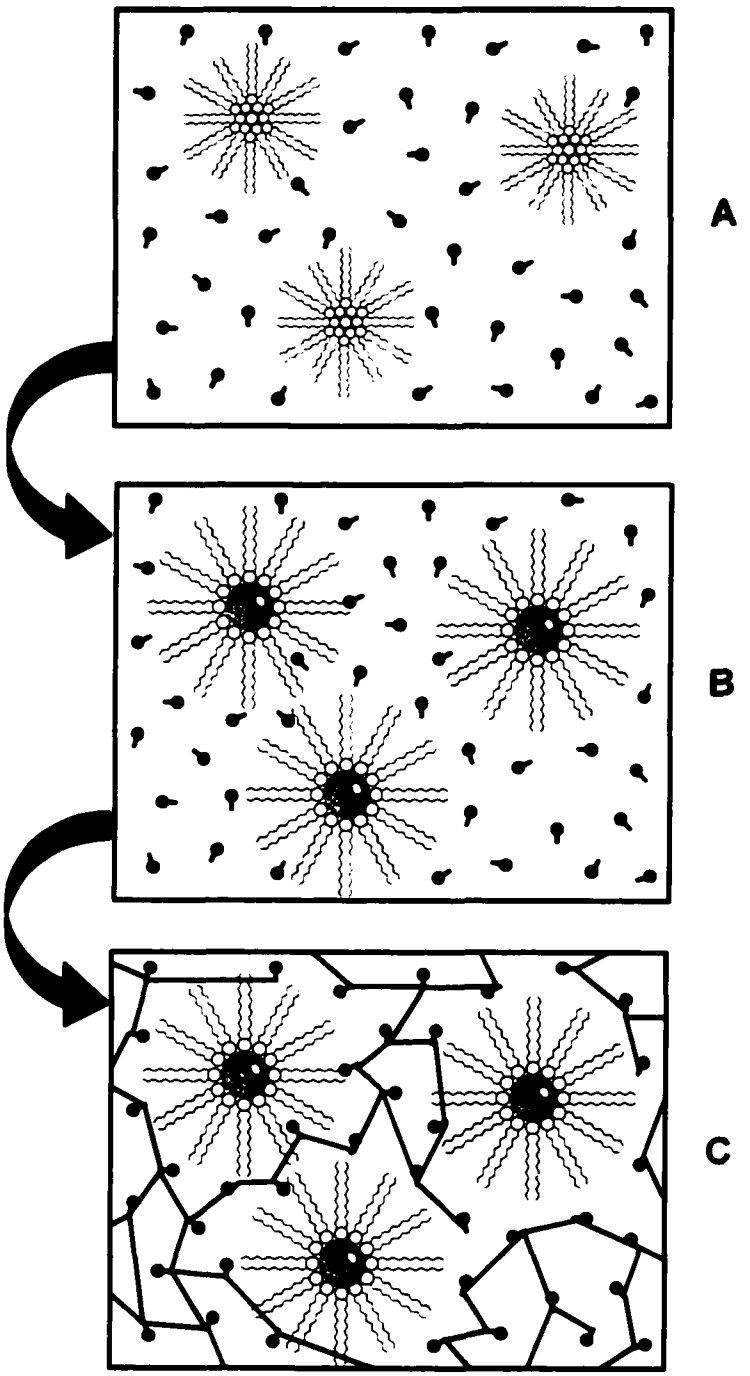

Figure 2.1. Materials synthesis strategy. First surfactant is dissolved in the monomer (A), then dye solution is injected (B), and polymerization results in encapsulated reverse micelles (C).

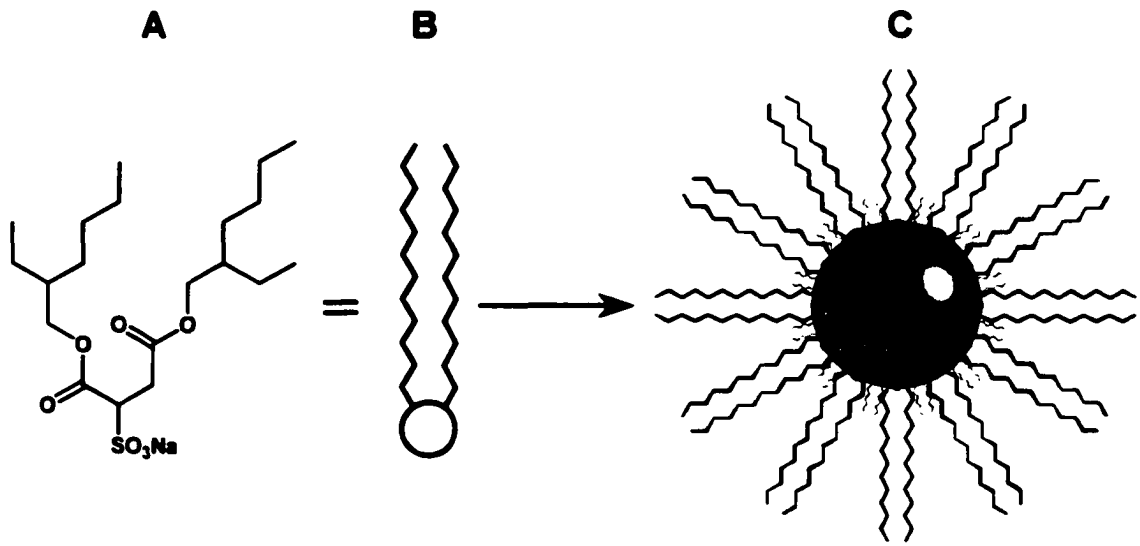

Figure 2.2. Structure of AOT (A) along with a schematic representation of its structure (B) and the structure of a reverse micelle (C).

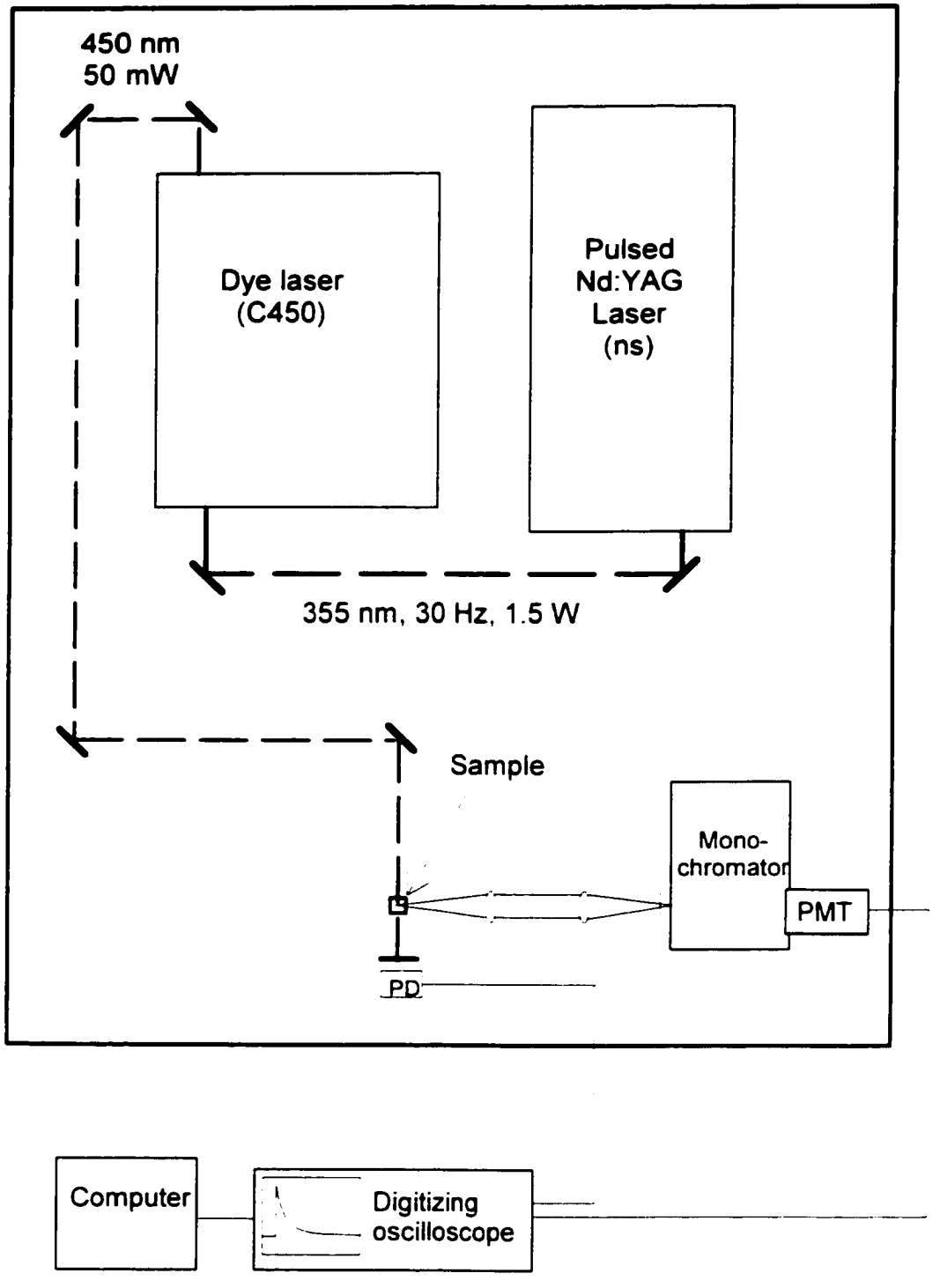

Figure 2.3. Schematic diagram of the instrumental setup for measuring fluorescence lifetimes using a Nd:YAG-pumped dye laser for excitation.

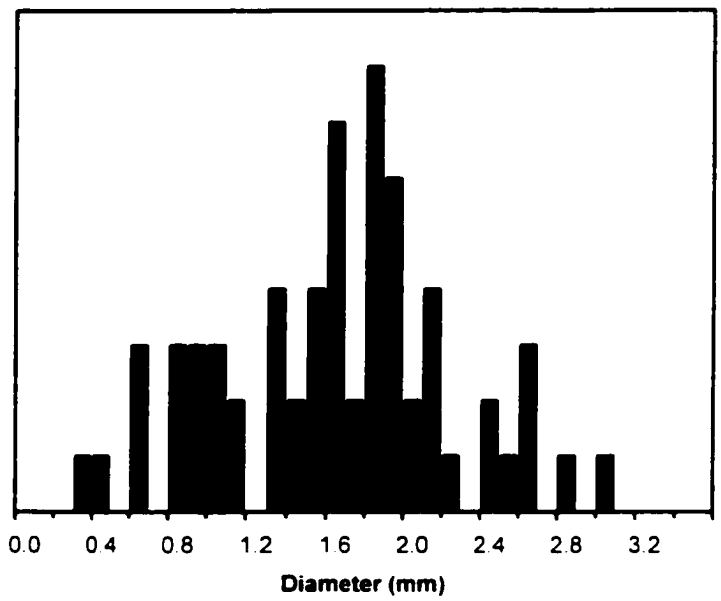

Figure 2.4. Histogram of the size distribution of emulsion droplets encapsulated in polystyrene. This data was obtained by visual measurement of a fractured monolithic sample under a light microscope. Sample population was 64.

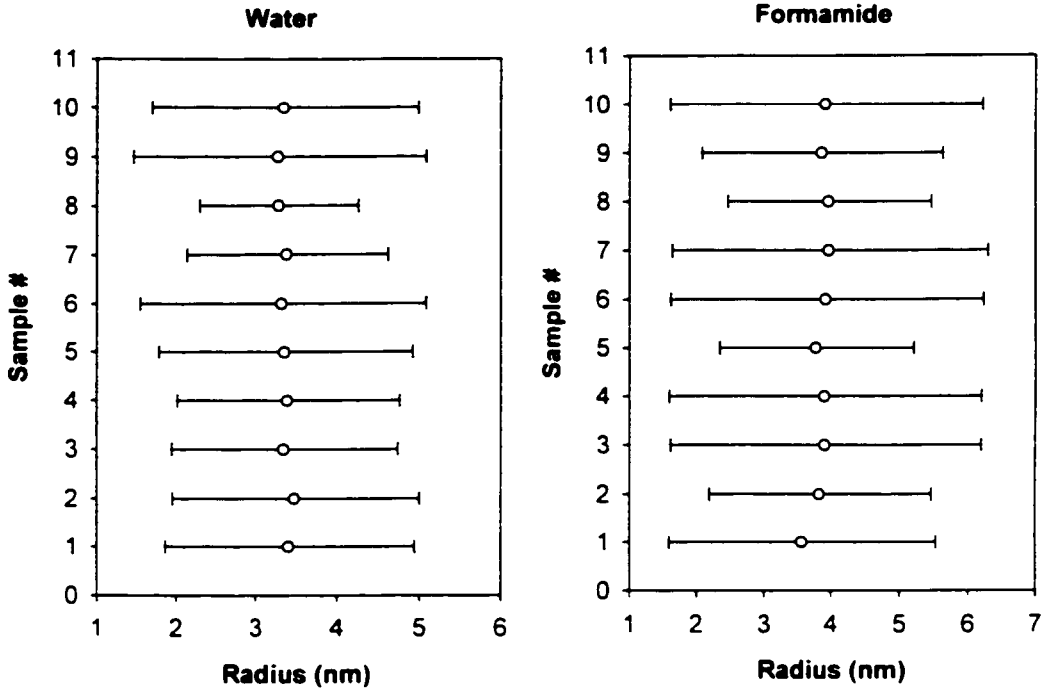

Figure 2.5. The raw data obtained from DLS determination of reverse micelle size. These two samples were prepared by injecting 8 μL of the corresponding polar solvent into a 2 mL sample of AOT containing monomer. Ten data samplings were obtained for each monomer sample. The error bars represent the range of sizes observed by the instrument within the sampling time, and the data points are the median values of this range.

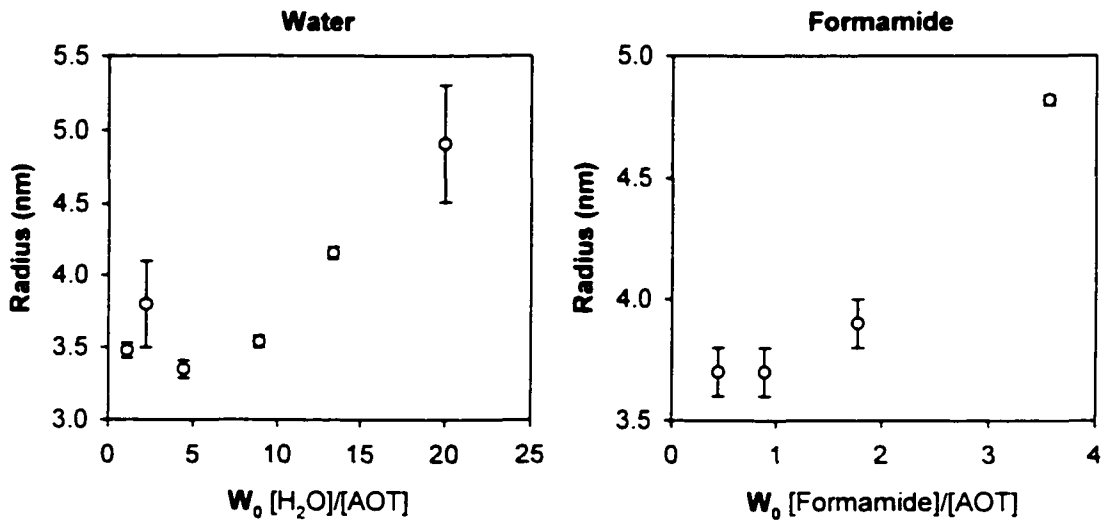

Figure 2.6. Plots of reverse micelle radius as a function of W_0 for water and formamide as the polar solvent inside reverse micelles. The radius values were calculated as the average of the median values from the DLS data. The error bars represent one standard deviation.

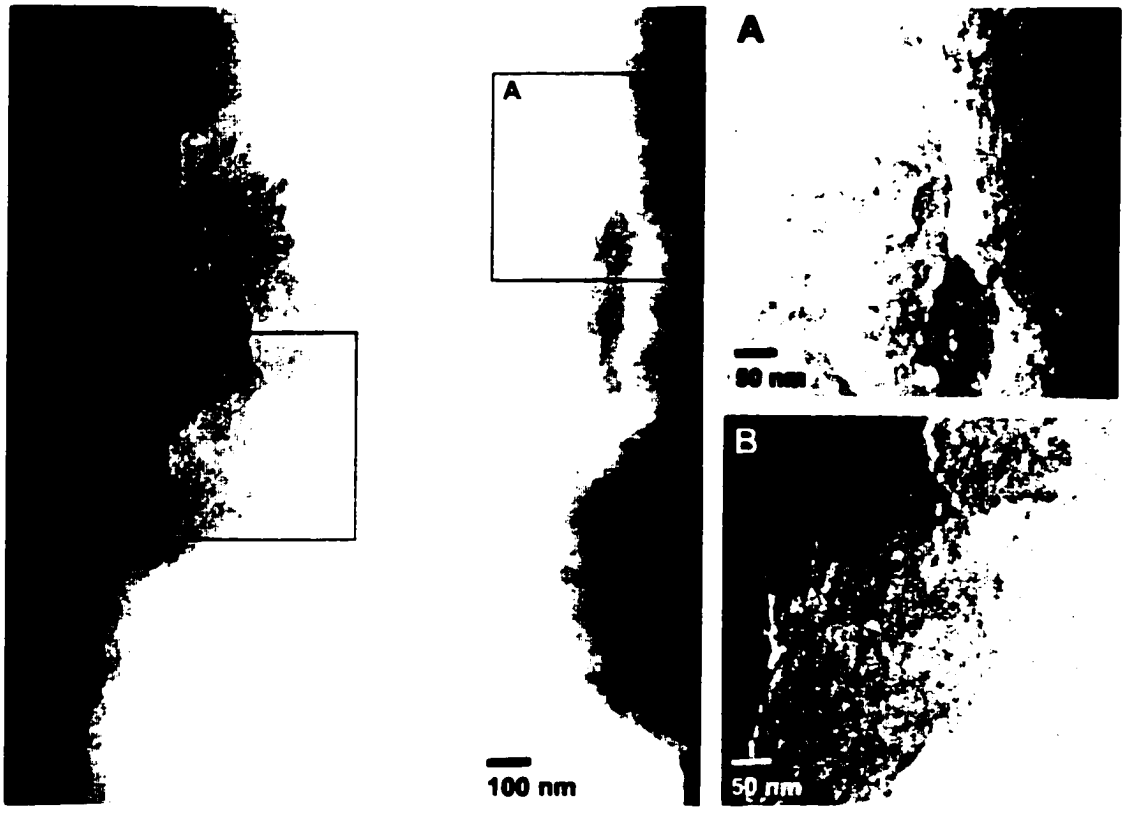

Figure 2.7. A TEM micrograph (left) of a thin section of cross-linked polystyrene encapsulating reverse micelles containing an aqueous Rubpy solution. Areas A and B were enhanced using the "Unsharp Mask" filter (Amount = 200%, Radius = 4 pixels, Threshold = 0 levels) in Adobe Photoshop version 6.0.

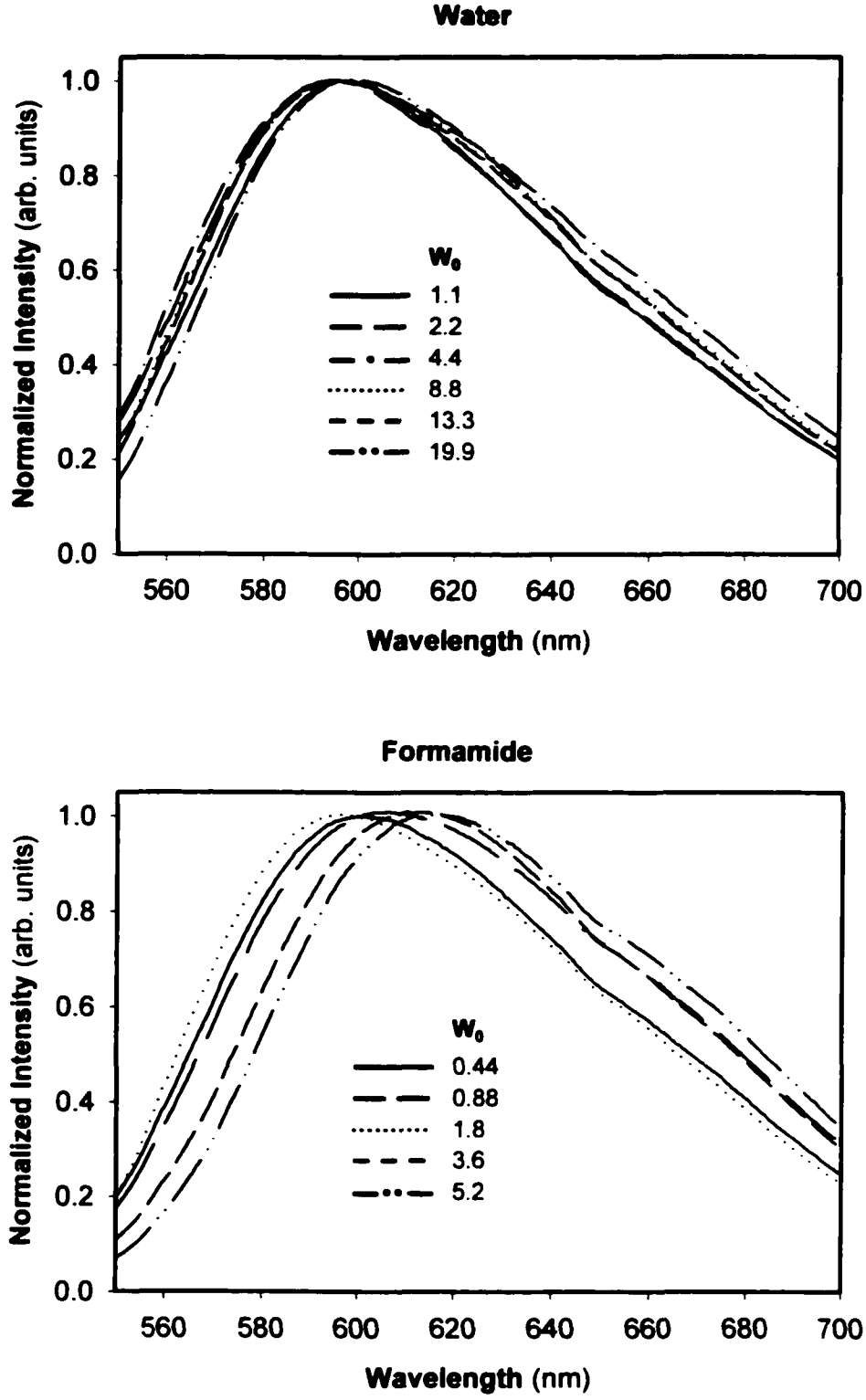

Figure 2.8. Emission spectra of polymer-encapsulated reverse micelles containing Rubpy in water (top) or in formamide (bottom). Each spectrum corresponds to a sample with differing W_0 (see legends).

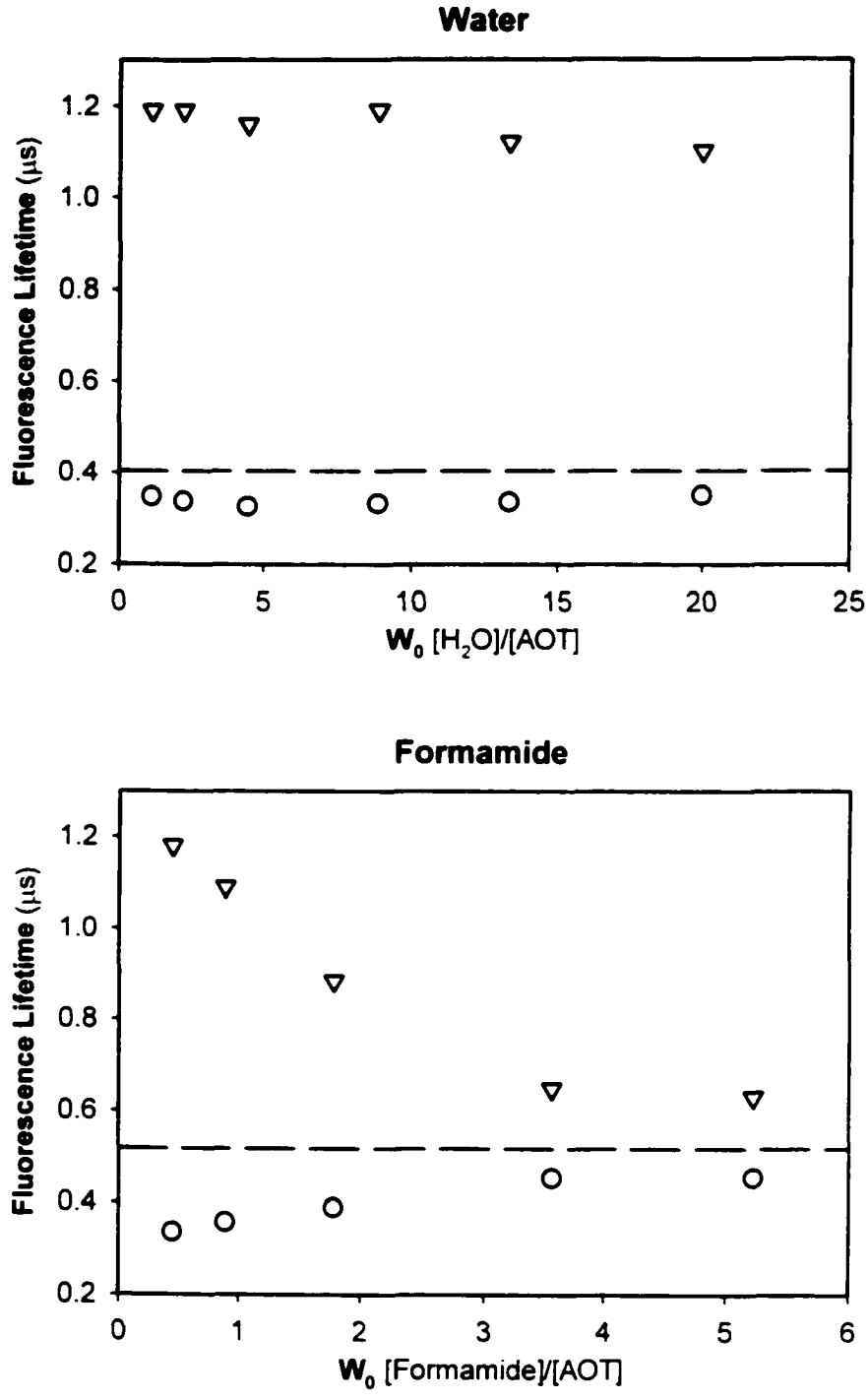

Figure 2.9. Plots of the fluorescence lifetime of Rubpy—in water (top) or formamide (bottom)—as a function of W_0. The lifetime measurements were made both prior to polymerization (○) and after polymerization (▽). The dashed line in each graph represents the measured fluorescence lifetime of Rubpy in the respective bulk solvent.

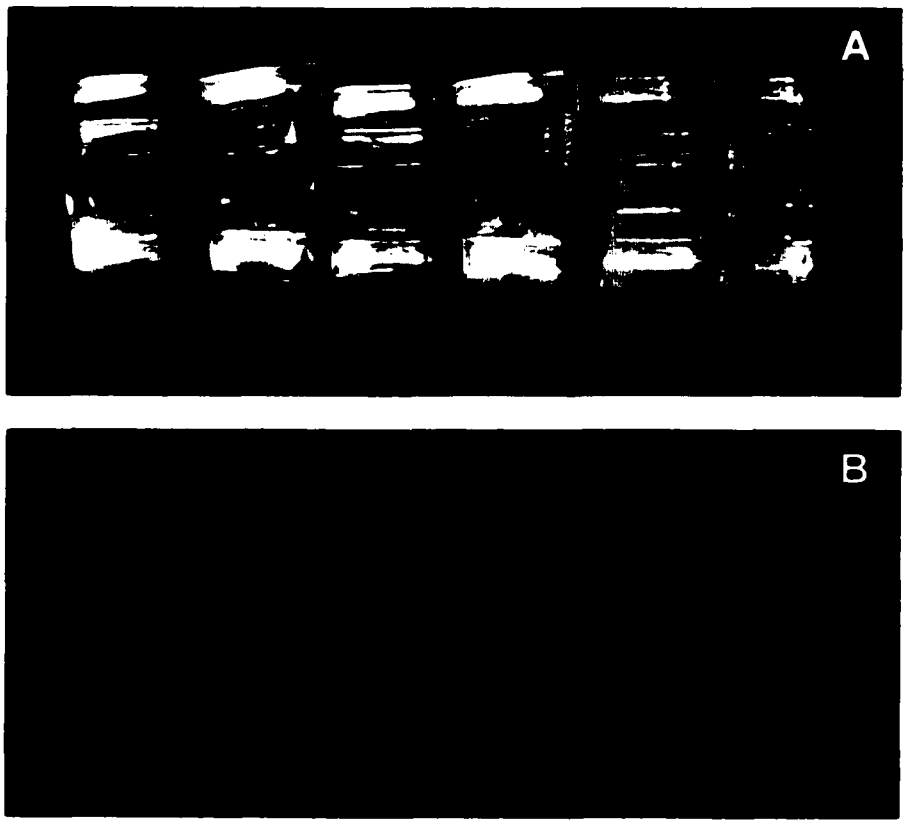

Figure 2.10. Polished monoliths of polymer-encapsulated reverse micelles containing increasing (left-to-right) concentrations of aqueous Rubpy solution under normal (A) and UV (B) illumination. These are the same samples used to obtain the data in Figure 2.8 and 2.9 top.

Chapter 2 References:

(1) www.cd-info.com; *Accessed June 2002.*

(2) www.cdrfaq.org; subject 7-1; *Accessed June 2002.*

(3) www.emediapro.net/EM1998/starrett10.html; *Accessed June 2002.*

(4) Ryu, C. K.; Wang, R. Y.; Schmehl, R. H.; Ferrere, S.; Ludwikow, M.; Merkert, J. W.; Headford, C. E. L.; Elliott, C. M. *J. Am. Chem. Soc.* **1992**, *114*, 430.

(5) Pichot, F.; Beck, J. H.; Elliott, C. M. *J. Phys. Chem. A* **1999**, *103*, 6263.

(6) Larson, S. L.; Elliott, C. M.; Kelley, D. F. *Inorg. Chem.* **1996**, *35*, 2070.

(7) Larson, S. L.; Elliott, C. M.; Kelley, D. F. *J. Phys. Chem.* **1995**, *99*, 6530.

(8) Larson, S. L.; Cooley, L. F.; Elliott, C. M.; Kelley, D. F. *J. Am. Chem. Soc.* **1992**, *114*, 9504.

(9) Cooley, L. F.; Larson, S. L.; Elliott, C. M.; Kelley, D. F. *J. Phys. Chem.* **1991**, *95*, 10694.

(10) Klumpp, T.; Linsenmann, M.; Larson, S. L.; Limoges, B. R.; Burssner, D.; Krissinel, E. B.; Elliott, C. M.; Steiner, U. E. *J. Am. Chem. Soc.* **1999**, *121*, 1076.

(11) Weber, J. M.; MacKenzie, V. J.; Limoges, B. R.; Sapp, S. A.; Elliott, C. M. *Manuscript in preparation.*

(12) Schmehl, R. H.; Ryu, C. K.; Elliott, C. M.; Headford, C. L. E.; Ferrere, S. *Adv. Chem. Ser.* **1990**, *226*, 211.

(13) Kalyanasundaram, K. *Photochemistry of polypyridine and porphyrin complexes*; 1st ed.; Academic Press: San Diego, 1992; Chapter 6.

(14) Allcock, H. R.; Lampe, F. W. *Contemporary Polymer Chemistry*; 2nd ed.; Prentice Hall: Englewood Cliffs, New Jersey, 1990; Chapter 3 & Appendix 2.

(15) Atkins, P. W. *Physical Chemistry*; 5th ed.; W. H. Freeman & Co.; New York, 1994; Chapter 23.

(16) De, T. K.; Maitra, A. *Adv. Colloid Interface Sci.* **1995**, *59*, 95.

(17) Riter, R. E.; Kimmel, J. R.; Undiks, E. P.; Levinger, N. E. *J. Phys. Chem. B* **1997**, *101*, 8292.

(18) Zhu, X. X.; Banana, K.; Yen, R. *Macromolecules* **1997**, *30*, 3031.

(19) Zhu, X. X.; Banana, K.; Liu, H. Y.; Krause, M.; Yang, M. *Macromolecules* **1999**, *32*, 277.

(20) Zhu, X. X.; Banana, K.; Yen, R. *Polym. Mater. Sci. Eng.* **1996**, *74*, 418.

(21) Leporini, D.; Zhu, X. X.; Krause, M.; Jeschke, G.; Spiess, H. W. *Macromolecules* **2002**, *35*, 3977.

(22) Colon, J. L.; Yang, C. Y.; Clearfield, A.; Martin, C. R. *J. Phys. Chem.* **1990**, *94*, 874.

Chapter 3.

Ionic derivatives of *N*-alkylphenothiazines as electron donors in bimolecular photosystems.

Introduction.

The Elliott group has had a longstanding interest in the photophysical properties of ruthenium trisbipyridyl-based chromophores and the electron-transfer processes of these dyes when combined with electron donors and acceptors.[1-5] In the past, the group has focused primarily on covalently-linked molecular assemblies in which a donor and/or acceptor are appended to the bipyridyl ligands of a ruthenium trisbipyridyl complex (see Figure 3.1).[2,3,5] This architecture results in molecular photosystems that have exhibited quantum efficiencies of greater than 80% for photo-induced charge separation.[4] This is an unprecedented efficiency that is generally only observed in biological photosystems, making these "triads" an excellent model photosystem for the study of artificial photosynthetic processes.[6]

The central core of this triad assembly is the $[Ru(L)_3]^{2+}$ chromophore (C^{2+}). One of the three bipyridine ligands has attached to it—via a two carbon chain—a diquaternary bipyridine (a so-called "diquat"). This moiety is capable of being reduced by the triplet metal-to-ligand charge-transfer state (^{3}MLCT) of C^{2+} and, as such, serves as an electron acceptor (A^{2+}). The two remaining bipyridines each have a pendant phenothiazine (PTZ) moiety that can be oxidized; thus, each is an electron donor (D). Subsequently, assemblies containing a chromophore and at least one appended electron donor and one

electron acceptor will be referred to as "triads"; they will be represented schematically as $D\text{-}C^{2+}\text{-}A^{2+}$. (NOTE: The fact that the assembly illustrated in Figure 3.1 contains two appended PTZ donors is purely a matter of synthetic expediency and is of no relevance. to its function. Consequently, it will still be referred to as a "triad" and will be represented as $D\text{-}C^{2+}\text{-}A^{2+}$ despite the presence of two donor moieties.) Similarly, assemblies containing a chromophore and *either* one appended electron donor *or* one electron acceptor will be referred to as "diads" and be represented by either $D\text{-}C^{2+}$ or $C^{2+}\text{-}A^{2+}$.

When a triad is irradiated with light of wavelength <500 nm, the C^{2+} can absorb a photon and generate the ^{3}MLCT (within a few picoseconds or less). Within a few hundred picoseconds following photoexcitation, the ^{3}MLCT reduces the acceptor to produce an intermediate charge-transfer state (CT), $D\text{-}C^{3+}\text{-}A^{\bullet-}$. On a time scale much faster than this initial electron-transfer, the CT reacts further in one of two ways: It either recombines to regenerate the ground state (i.e., $D\text{-}C^{2+}\text{-}A^{2+}$) or the donor is oxidized by C^{3+} to yield the fully charge-separated state (CS), $D^{\bullet+}\text{-}C^{2+}\text{-}A^{\bullet-}$. Figure 3.2 schematically depicts this overall process. In 1,2-dichloroethane the specific triad illustrated in Figure 3.1A (wherein n = 3) produces CS with a quantum efficiency of 86 ± 8%—in other words, virtually every photon absorbed produces a CS.[4]

In the early work with these compounds it was noted that the visible spectra of $D\text{-}C^{2+}\text{-}A^{2+}$ and $D\text{-}C^{2+}$ assemblies—where D is specifically a PTZ moiety—showed evidence of a D,C^{2+} ground state charge-transfer interaction.[7] As it turns out, it is this interaction that is ultimately responsible for the large quantum efficiency for CS formation (see Figure 3.2 top equilibrium).[8] Comparisons between spectra of complexes that contain attached PTZ

donors (i.e., D-C^{2+} and D-C^{2+}-A^{2+}) and analogs that do not (i.e., C^{2+} and C^{2+}-A^{2+}) show slight but reproducible differences in the shape of the MLCT transitions. From these spectra, it is difficult to quantify the interaction because of the strong interference from the MLCT transition of C^{2+}. However, the ^{1}H NMR spectra of the aromatic protons on the ligands of tris(1,10-phenanthroline)ruthenium(II) show a linear shift as a function of the concentration of added *N*-methylphenothiazine (NMPTZ); clearly indicating a ground state interaction between the ligands on C^{2+} and NMPTZ.[7]

Recently, Weber et al. have demonstrated that this D,C^{2+} charge-transfer interaction is intimately involved in CS formation.[8] In the bimolecular reaction between the photoexcited C^{2+}-A^{2+} diad (illustrated in Figure 3.1B) and a given concentration of NMPTZ, the initial amount of photoinduced CS observed cannot be accounted for by simple diffusional encounters.[7,8] Consequently, some form of D,C^{2+} pre-association is required to rationalize the amount of CS produced. As part of this study, Weber et al. were able to estimate the magnitude of the equilibrium constant for the charge-transfer complex formation (K_{eq}).[8] This was accomplished by assuming that all the CS that is formed originates from a pre-associated D,C^{2+}-A^{2+} assembly, and from the charge-transfer complex formation equilibrium:

$$D + C^{2+}\text{–}A^{2+} \overset{K_{eq}}{\rightleftharpoons} D,C^{2+}\text{–}A^{2+} \qquad K_{eq} = \frac{[D,C^{2+}\text{–}A^{2+}]}{[D][C^{2+}\text{–}A^{2+}]} \quad (1)$$

It follows from mass balance that:

$$[C^{2+}\text{–}A^{2+}] = [C_t] - [D,C^{2+}\text{–}A^{2+}] \quad (2)$$

where $[C_i]$ is the initial concentration of the diad. Plugging this into the equilibrium equation (1) and solving for $[D,C^{2+}\text{-}A^{2+}]$ results in:

$$[D,C^{2+}\text{–}A^{2+}] = \frac{[C_i]\,K_{eq}\,[D]}{1 + K_{eq}\,[D]} \quad (3)$$

Assuming that the quantum efficiency is unity, then:

$$[CS] = \frac{B[C_i]\,K_{eq}\,[D]}{1 + K_{eq}\,[D]} \quad (4)$$

where B is a spectral constant relating $[C_i]$ and $[C_i]^*$. Since [CS] is proportional to the initial absorbance of CS (ΔAbs) measured in a flash-photolysis transient absorption experiment (see experimental for details):

$$[CS] \propto \Delta Abs \quad (5)$$

thus,

$$\Delta Abs = \frac{AB[C_i]\,K_{eq}\,[D]}{1 + K_{eq}\,[D]} \quad (6)$$

where A is an instrumental proportionality constant. A plot of ΔAbs as a function of [D] can then be fitted to a function of the form:

$$f(x) = \frac{abx}{1 + bx} \quad (7)$$

where b is equal to K_{eq}. For the specific bimolecular system in Figure 3.1B, the fitted value for K_{eq} was $10^1\ M^{-1}$ in DCM.[8]

Thus far the consideration of spin chemistry has been intentionally ignored, except to acknowledge that the MLCT has triplet spin multiplicity. The C^{2+} species is a low-spin

d^6 complex; thus all metal electrons are paired. Also, A^{2-} and D have no unpaired electrons; therefore, the ground state species, $D\text{-}C^{2+}\text{-}A^{2-}$, is a singlet. Since the excited and ground states have different spin multiplicities, in principle, the rates of processes connecting these two states could be influenced by externally applied magnetic fields. In fact, this is just what Klumpp et al. observed for a series of triads.[4] In the bimolecular photosystem of D and $C^{2+}\text{-}A^{2-}$, however, cage escape of $D^{+\bullet}$ destroys spin memory, therefore the following discussion of magnetic field effects applies only to triads.

Figure 3.3A shows a series of transient absorption decay curves for a solution containing the triad complex illustrated in Figure 3.1A wherein n = 2.[4] In this series of experiments the excitation was at 460 nm, near the maximum of the MLCT transition, and the decay was monitored at 390 nm near the maximum absorbance of $A^{-\bullet}$. In zero field, the CS lifetime for this triad is on the order of 100 ns. With applied fields between 1 and 500 mT, the decay kinetics of the CS are strongly affected by the field. Specifically, the decay is split into a fast minor component and a slow major component. The rate constant for the minor component is approximately field-independent, whereas the rate constant for the major component decreases steadily with increasing field. The effect is first observable at about 1 mT and limits at about 500 mT.

In the absence of a field, the triplet spin multiplicity of the ^{3}MLCT is transmitted intact through the CT product ($D\text{-}C^{3+}\text{-}A^{-\bullet}$) to the CS. In other words, as it is formed the CS is a "pure" triplet; consequently, recombination to the singlet ground state (^{1}GS) is formally spin forbidden. Return to the ^{1}GS occurs via the spin allowed pathway from ^{1}CS, which is made possible by the rapid mixing (ca. 5×10^8 s^{-1}) of the ^{3}CS and ^{1}CS by hyperfine coupling.[4]

Figure 3.3B illustrates the effect of weak magnetic fields on the CS portion of the reaction manifold. Application of a field results in Zeeman splitting of the triplet, which disrupts the degeneracy between the T_- and T_+ levels and ^1CS. As a result, the mixing of these components with the singlet is less efficient (i.e., slower) giving rise to the bi-exponential character of the CS decay. As the field is increased the triplet-to-singlet inter-conversion of the outer Zeeman components becomes slower until eventually the spin-forbidden pathway, 4, is dominant. It is speculated that this pathway becomes partially allowed through spin-orbit effects from the sulfur atom in the PTZ radical cation.

The magnetic field effect data in Figure 3.3A very clearly demonstrates the sensitivity of these triads to very weak magnetic fields. This magnetic-field-dependent difference in CS lifetime and the concomitant changes in visible spectra, in principle, could serve as an optical transducer of weak magnetic fields for use in a sensor material (see Chapter 2). However, the synthesis and purification of triads is very difficult, and yields of purified product are typically only a few milligrams. In contrast, diads are much simpler to produce and yields are on the order of hundreds of milligrams. Diads in solution with NMPTZ do not exhibit any magnetic field sensitivity (*vide supra*). However, the confinement of geminate radical pairs in micelles or reverse micelles has been shown to retain spin memory and thus magnetic field sensitivity in a number of bimolecular photosytems.[9-11]

The primary objective of this research was to confine a D and C^{2+}-A^{2+} diad within the core of a micelle or reverse micelle, to discover if magnetic field effects could be retained in diad-based bimolecular photosystems. In the course of these investigations, this

seemingly simple objective proved to be quite a challenge. Micelles or reverse micelles are either extremely non-polar or extremely polar in their respective interiors. Of the two structures, reverse micelles were selected because polar derivatives of PTZ could be synthesized more easily than a non-polar diad. This resulted in a series of ionic *N*-alkylphenothiazines and a number of salts thereof shown in Figure 3.4. These products included a C^{2+}-A^{2+} diad salt of PTZ4S$^-$ that was studied inside Aerosol-OT reverse micelles in toluene.

The ancillary objective to study the effect of ionic derivatization of D on the formation of CS with diads was made possible by the synthesis of extremely lypophillic salts of both the PTZ cation and anion—PTZ3Q-BARF and TOA-PTZ4S, respectively. These salts were soluble in the same conditions as those used to study NMPTZ-diad photophysics, making direct comparison of the data possible. The results of these investigations follow.

Experimental Section.

Materials. All solvents other than deionized water and tetrahydrofuran (THF) were purchased from Fisher at spectroscopic grade or better purity. THF was distilled over a Na^0/benzophenone mixture and under nitrogen just prior to use. Activated neutral alumina, sodium bicarbonate, lithium perchlorate ($LiClO_4$), Aerosol-OT (AOT), *para*-toluenesulfonic acid sodium salt (Na-PTSA), tetrabutylammonium hexafluorophosphate (TBA-PF_6), tetraoctylammonium iodide (TOA-I), 1,4-butanesultone, 0.25 M *n*-butyllithium in hexane, promazine hydrochloride, phenothiazine, and iodomethane at ≥97% purity were purchased from Sigma-Aldrich and used as received. Ammonium hexafluorophosphate (NH_4PF_6) was purchased from Ozark-Mahoning (Tulsa, Oklahoma)

and used as received. Bis(1,10-phenanthroline)dichlororuthenium(II) was synthesized according to a procedure adapted from Sullivan et al.[12] 4-(1-(1'-methyl-4,4'-bipyridinediium-1-yl)-3-propyl)-4'-methyl-2,2'-bipyridine$(PF_6)_2$ and [bis(1,10-phenanthroline)(4-(1-(1'-methyl-4,4'-bipyridinediium-1-yl)-3-propyl)-4'-methyl-2,2'-bipyridine)ruthenium(II)]$(PF_6)_4$ (3CA-PF_6) were synthesized by John M. Weber according to a procedure adapted from Yonemoto et al.[13] Potassium tetrakis(3,5-di(trifluoromethyl)phenyl)borate (K-BARF) was synthesized by Dr. Susan M. Hendrickson according to a procedure adapted from Iwamoto and Bahr et al.[14,15]

Synthesis of lithium (1-(10-phenothiazinyl)-4-butyl)sulfonate (Li-PTZ4S). A solution of phenothiazine (0.56 g, 2.8 mmol) in 60 mL THF was cooled to -78 °C (dry-ice/acetone) under nitrogen in a flask equipped with a reflux condenser. After cooling this solution, 1.1 ml (2.8 mmol) of 2.5 M *n*-butyllithium in hexane was injected via syringe. This mixture immediately turned deep gold-yellow, and was stirred for ca. 30 minutes, after which time, the dry-ice/acetone dewar was removed. As the reaction mixture was starting to warm to room temperature (RT), 6.2 ml (60 mmol) of 1,4-butanesultone in 20 ml of THF was added via syringe. The color of this mixture turned orange as it continued to warm to RT with stirring. After stirring at RT for ca. 30 minutes, this mixture was brought to reflux and left overnight. Upon cooling, 20 ml of methanol was added to the light yellow solution, with no obvious effect. Approximately 40 ml of diethyl ether was then added, and this mixture was cooled for 24 hours in the freezer to precipitate the product. The crude product was filtered and rinsed in diethyl ether to yield 0.6 g (63%) of white solid.

^{1}H NMR (300 MHz, CD_3OD) δ ppm: 1.91 (4H, quintet, 2× CH_2), 2.80 (2H, t, 1× CH_2-SO_3^-), 3.93 (2H, t, 1× PTZ-CH_2), 7.02 (8H, m, 8× PTZ-H).

Synthesis of tetraoctylammonium (1-(10-phenothiazinyl)-4-butyl)sulfonate (TOA-PTZ4S). Li-PTZ4S was dissolved in a minimal amount of ca. 2:1 volume ratio of water:methanol. A saturated solution of TOA-I in the same solvent was also prepared, and when added to the Li-PTZ4S solution, TOA-PTZ4S formed an oily phase that was isolated by decanting. To dry the product, the oil was frozen in a glass vial immersed in liquid nitrogen. This solid product was crushed and powdered in its frozen state, and placed (still frozen) in a vacuum oven at RT and dried overnight.

Synthesis of trimethyl-(1-(10-phenothiazinyl)-3-propyl)ammonium iodide (PTZ3Q-I). The free base of promazine was obtained from the hydrochloride salt by liquid-liquid extraction from aqueous bicarbonate solution into dichloromethane (DCM). Rotary evaporation of the solvent afforded a viscous oil of the promazine free base. 2.5 g (8.8 mmol) of this oil was dissolved in 50 mL acetone along with 1.36 g (9.1 mmol) of iodomethane under nitrogen in a flask equipped with a magnetic stirbar. This mixture was stirred overnight at RT. No precipitate had formed in this time so a heating mantle and reflux condenser were employed to bring the mixture to reflux for 4 hours. Cooling, adding 30 ml of diethyl ether, and scratching the side of the flask with a glass rod resulted in heavy precipitation of the product, which was filtered and rinsed with diethyl ether. This yielded 3.2 g (85 %) of white solid product.

^{1}H NMR (300 MHz, CD_3CN) δ ppm: 2.17 (2H, quintet, 1× CH_2), 2.92 (9H, s, 3× N-CH_3), 3.35 (2H, m, 1× CH_2-N), 4.01 (2H, t, 1× PTZ-CH_2), 7.01 (4H, m, 4× PTZ-H), 7.24 (4H, m, 4× PTZ-H).

Synthesis of trimethyl-(1-(10-phenothiazinyl)-3-propyl)ammonium hexafluorophosphate (PTZ3Q-PF_6). PTZ3Q-I was dissolved in a minimal amount of ca. 2:1 volume ratio of water:methanol. A saturated solution of NH_4PF_6 in the same solvent was also prepared. Mixing the two solutions resulted in the precipitation of a white solid that was isolated by centrifuge and dried under vacuum at RT.

Synthesis of trimethyl-(1-(10-phenothiazinyl)-3-propyl)ammonium tetrakis(3,5-di(trifluoromethyl)phenyl)borate (PTZ3Q-BARF). The solubility of PTZ3Q-PF_6 in DCM was poor (ca. < 5 mM), so PTZ3Q-BARF was made by the metathesis of PTZ3Q-I and excess K-BARF in ca. 5:1 methanol:water. This resulted in the formation of a white precipitate that was isolated by centrifuge and dried under vacuum at RT. The DCM solubility of this salt was ca. × 3 better than PTZ3Q-PF_6.

Synthesis of [bis(1,10-phenanthroline)(4-(1-(1'-methyl-4,4'-bipyridinediium-1-yl)-3-propyl)-4'-methyl-2,2'-bipyridine)ruthenium(II)]$(PF_6)_2(Cl)_2$ (3CA-Cl). The following reaction and workup were done under darkroom conditions to prevent photodegradation of the product. A solution of 22 mg (41.3 μmol) of bis(1,10-phenanthroline)dichlororuthenium(II) in 15 ml of 2-propanol was added to a flask equipped with a reflux condenser and magnetic stirrer. After refluxing this solution for 1 hour, 32 mg (47.7 μmol) of 4-(1-(1'-methyl-4,4'-bipyridinediium-1-yl)-3-propyl)-4'-methyl-2,2'-bipyridine$(PF_6)_2$ was added, and reflux continued overnight. During this time, the solution turned from deep purple to rusty red-orange. Rotary evaporation of the solvent yielded a rusty red-orange solid that was chromatographed on Sephadex-SP C25 (Aldrich) with a gradient of 0.01 M to 0.5 M Na-PTSA in water. The pure product eluted as the third and final band—which remained at the origin until the concentration of Na-

PTSA reached ca. 0.3 M. The product containing fractions were combined and the solvent was removed by rotary evaporation.

Synthesis of [bis(1,10-phenanthroline)(4-(1-(1'-methyl-4,4'-bipyridinediium-1-yl)-3-propyl)-4'-methyl-2,2'-bipyridine)ruthenium(II)](PF$_6$)$_x$((1-(10-phenothiazinyl)-4-butyl)sulfonate)$_y$ (3CA-PTZ4S) ***where x + y = 4.*** The following metathesis was done under darkroom conditions to prevent photo-degradation of the product. 3CA-PTZ4S was made by the metathesis of 3CA-Cl and excess Li-PTZ4S in water. This resulted in the formation of a bright orange precipitate that was isolated by centrifuge and dried under vacuum at RT.

Electrochemistry. Cyclic voltammetric data was obtained using a standard three-electrode cell with an EG&G PAR Model 173 Potentiostat/Galvanostat controlled by a Model 175 Universal Programmer. The reference electrode was Ag/Ag$^+$ (0.47 V vs. SHE) composed of 0.1 M silver nitrate in dimethylsulfoxide. The auxiliary electrode was a 0.5 cm^2 platinum flag and the working electrode was a 2.8×10^{-2} cm^2 platinum disc electrode (BAS). The analyte concentration was 10 mM, and the supporting electrolyte was either 0.1 M $LiClO_4$ in propylene carbonate or 0.1 M TBA-PF_6 in acetonitrile (ACN). The data was recorded on a Yokogawa 3023 X-Y recorder. This data was scanned and plotted using an Acer flatbed scanner and Adobe Photoshop v6.0 on a computer running Microsoft Windows® XP.

Sample Preparation. With the exception of the reverse micelle-containing sample, all samples consisted of ca. 10^{-5} M 3CA-PF_6 in DCM. One of the donors under investigation was also added to this diad solution at varying concentrations (ca. 0.5-45

mM) to prepare different samples. For comparison between different donors, samples of the diad solution were prepared with each donor at 10^{-2} M.

Reverse micelles were prepared with AOT dissolved in toluene to a concentration of 0.1 M. A concentrated solution (ca. 10^{-2} M) of 3CA-PTZ4S in formamide was then injected via microliter syringe into the toluene solution (5 μl in 2 ml). Vigorous mixing resulted in a completely homogeneous solution with no obvious phase separation or light scattering.

All samples were prepared and handled under darkroom conditions prior to rigorous degassing by freeze-pump-thawing for three cycles using liquid nitrogen. This was accomplished in a 1 cm path-length optical glass cell equipped with a Pyrex® sidearm (for freezing) and a threaded Teflon® valve for vacuum attachment.

Transient Absorbance. Transient absorbance data was obtained on the instrument depicted in Figure 3.5. The frequency-tripled output of a Spectra-Physics LAB-190 Nd:YAG laser produced a train of ca. 8 ns pulses at 30 Hz and ca. 1.5 W of power. This output pumped a methanolic solution of Coumarin 450 dye (Exciton) in a Spectra-Physics PDL-3 dye laser. The typical output from the dye laser was a corresponding train of pulses ca. 50 mW in power at 450 nm.

The excitation beam was directed onto the sample orthogonal to the probe beam. The probe beam consisted of the output of an Oriel xenon arc lamp, focused through a Bausch & Lomb monochromator and onto the sample. The light exiting the sample was collimated and focused onto the entrance slit of a Jarrell Ash model 82-410 monochromator. Both monochromators were set to pass the same wavelength, and for these investigations, 397 nm was used, which corresponds to the absorption maxima of

A^{**}. The light that exited the second monochromator was detected with a Hamamatsu model R2496 photomultiplier tube operated at ca. 500 V.

The output from the photomultiplier tube was sent to a Tektronix TDS 620B digital oscilloscope. A Thorlabs DET210 fast photodiode monitoring scattered laser light was used to trigger the oscilloscope. Signal averaging of 200 sets of decay curves was used to improve signal-to-noise levels. The output from the oscilloscope was saved to disc as x-y data pairs in ASCII format. Using a computer running Microsoft Windows® XP, this data was organized and truncated in Microsoft Excel®; graphical and exponential regression analysis was carried out in SigmaPlot® version 2000.

A magnetic field was applied to the reverse micelle-containing sample by mounting a stack of four cylindrical neodymium-iron-boron permanent magnets (5.1 cm diameter × 2.5 cm wide, Edmund Scientific) next to the sample cell. The field strength in the area of the sample holder was measured with a gaussmeter on loan from Prof. Carl E. Patton, Department of Physics, Colorado State University and found to be 600 mT.

Results and Discussion.

Electrochemistry. The cyclic voltammetric response of both the PTZ anion ($PTZ4S^{\cdot}$) and the PTZ cation ($PTZ3Q^{\cdot}$) are shown in Figure 3.6. Li-PTZ4S was only sparingly soluble in ACN so propylene carbonate was used as the electrolyte solvent. Under these conditions the $E_{1/2}$ is 0.41 V with a ΔE_p of 80 mV. The $E_{1/2}$ of PTZ3Q-PF_6 was measured in ACN and was found to be 0.50 V with a ΔE_p of 62 mV. These redox properties were expected and found to be comparable to NMPTZ, which has an $E_{1/2}$ of 0.42 V in ACN. This result is important because the intention of the ionic derivatization was to alter the

solubility of the PTZ donors without altering the thermodynamic driving forces involved in CS formation.

Transient Absorption and Lifetime of CS. The photophysics of bimolecular photosystems employing NMPTZ have typically been studied in solvents such as DCM or 1,2-dichloroethane (DCE). These are poor solvents for highly ionic species, but *N*-alkylphenothiazines are only sparingly soluble in more polar solvents so a suitable compromise is found in DCM and DCE. For example, the diad 3CA-PF_6 (10^{-5} M) and NMPTZ (50 mM) in DCE readily forms a CS when photo-excited at 450 nm. The lifetime of the CS is measured by monitoring the absorption signal of the reduced viologen acceptor, and is found to be 190 μs. Note that the bimolecularly formed CS is more than three orders of magnitude longer-lived than the CS formed from triads (*vide supra*). This is attributed simply to the fact that $NMPTZ^{+\bullet}$ can cage-escape and thus recombination becomes a diffusion-controlled process—a much slower process than the intramolecular recombination present in triads.

In contrast to NMPTZ, both types of ionic derivatives of PTZ exhibit much shorter CS lifetimes—similar to triads—under comparable conditions. Figure 3.7 shows plots of the bimolecular CS transient absorption signals for 3CA-PF_6 with TOA-PTZ4S or PTZ3Q-BARF. The anionic PTZ results in a CS with a lifetime of 260 ns, and the CS lifetime with cationic PTZ is 510 ns. These shorter lifetimes suggest a much lower effective cage escape yield for the ionic PTZ derivatives. In other words, after the CS is formed, these oxidized donors remain closer to the C^{2+}-$A^{+\bullet}$ and thus are more readily available for recombination than $NMPTZ^{+\bullet}$.

It is likely that aggregation or clustering of ionic species in DCM is largely responsible for these effects, but there is presently no data to confirm this. Furthermore, the fact that oxidized NMPTZ is a radical cation, oxidized PTZ3Q is a di-cation, and oxidized PTZ4S is a zwitterion complicates the interpretation of these results in terms of a simple electrostatic attraction or repulsion model. The fact that the lifetime of the CS with PTZ4S is nearly half that with PTZ3Q can, however, be rationalized in this way. The diad, C^{2+}-$A^{\bullet-}$, is highly positively charged thus the zwitterionic oxidized PTZ4S is less coulombically repulsed from the diad than the di-cationic oxidized PTZ3Q.

However, this rationale makes less intuitive sense when the CS decay kinetics with oxidized NMPTZ are considered. The lifetime of CS with NMPTZ as a donor is ca. four orders of magnitude longer lived than with PTZ3Q (*vide supra*). The fact that the decay kinetics of cationic oxidized NMPTZ suggest a higher apparent cage-escape yield than the di-cationic oxidized PTZ3Q cannot be rationalized by the simple electrostatic model proposed above. It may be that the positive charge on oxidized NMPTZ, which is delocalized over the aromatic portion of the molecule, behaves differently than a localized cationic charge, both in terms of solvation by DCM and its electrostatic properties. This possibility, together with some form of ionic aggregation behavior with PTZ3Q and PTZ4S, but not with NMPTZ could be responsible for the counterintuitive results. Again, this is merely speculation: there is presently no conclusive data to support this.

Measurement of K_{eq}. In an effort to further compare the behavior of bimolecular photosytems with ionic and non-ionic donors, the initial absorption of CS was measured as a function of donor concentration for both ionic PTZs. Figure 3.8 contains the plots of

this data for TOA-PTZ4S and PTZ3Q-BARF with 3CA-PF_6 in DCM. The data from each experiment was fit to a function of the form of equation 7, and the results of the fits are represented as a dashed line in each graph. Both fits agree well with the measured data, and the values calculated for K_{eq} were on the order of 10^2 M^{-1} for both the PTZ anion and cation. This is an order of magnitude higher than the K_{eq} value measured for NMPTZ with the same diad and solvent (*vide supra*). Again it is speculated that ionic aggregation could account for these differences between ionic and non-ionic donors, but at present, only DCM has been used as a solvent in these studies. Possibly by carrying out similar experiments in other solvents, these assertions could be evaluated, but studies of this nature were not within the scope of these investigations.

Bimolecular Magnetic Field Response in Reverse Micelles. There are a very limited number of polar solvents other than water that can be sequestered by AOT reverse micelles.[16] Fortunately, formamide is a solvent that is both sequestered by reverse micelles and readily dissolves 3CA-PTZ4S—which was metathesized by precipitation out of water. AOT-toluene solutions injected with 3CA-PTZ4S in formamide formed homogeneous solutions upon mixing that were visually identical to normal solutions of the 3CA-based dyes.

Figure 3.9 contains the transient absorption data from this sample in the absence and presence of a magnetic field. With no field present, the CS decays via a single exponential process and has a lifetime of 130 ns. When a field of 600 mT is applied, ca. 80% of the CS population retains its fast recombination kinetics with a lifetime of 160 ns, but ca. 20% of the CS population recombines via a much slower process and has a lifetime of 710 ns. This data is qualitatively consistent with the magnetic field effect data

observed in triads,[4] with one exception: this effect in triads was saturated at comparable field strengths, while this system exhibits what is apparently only a minor change. However, without the capabilities to conduct a full magnetic field effect study, it is difficult to say whether this system is truly less responsive to magnetic fields or whether its response is inherently different. Nonetheless, this data represents proof of concept that it is possible to retain spin memory—and magnetic field sensitivity—by confining a bimolecular photosystem of this type in reverse micelles.

Conclusions.

A series of ionic *N*-alkylphenothiazines was synthesized and characterized using electrochemistry and transient absorption spectroscopy. The cyclic voltammetric response of both the PTZ anion and cation were found to be very similar ($E_{1/2}$ values within 80 mV) to NMPTZ. Studies of TOA-PTZ4S or PTZ3Q-BARF as donors in a bimolecular photosystem with 3CA-PF_6 in DCM revealed formation of CS with lifetimes on the order of hundreds of nanoseconds. This behavior is more akin to the photophysics observed with triads rather than diads, and is attributed to a low cage escape yield for the oxidized donor, possibly due to ion aggregation in DCM. Fits obtained from plots of the initial amount of CS formed versus donor concentration revealed K_{eq} values an order of magnitude higher than for NMPTZ and the same diad. This indicates a strong pre-association of these ionic PTZs with the diad chromophore in DCM.

Finally, the primary objective of this project was achieved using a mixed salt of the diad and donor (3CA-PTZ4S). A concentrated solution of this mixed salt in formamide was sequestered inside AOT reverse micelles in toluene. The transient absorption of the CS revealed recombination kinetics comparable to triads. Furthermore, the application of

a 600 mT magnetic field resulted in the appearance of a second, slower recombination process also similar to the magnetic field effect observed with triads. However, at this field strength, the effect is quite small; far less sensitive than would be required for sensor applications. Nonetheless, this research provides useful information about the effects of ionic derivatization of donors and their behavior in bimolecular photosystems. The results of these studies along with further investigation into the intermolecular interactions between donors, chromophores, and acceptors could lead to the design of a highly efficient, next-generation photosystem.

Chapter 3.

Figures

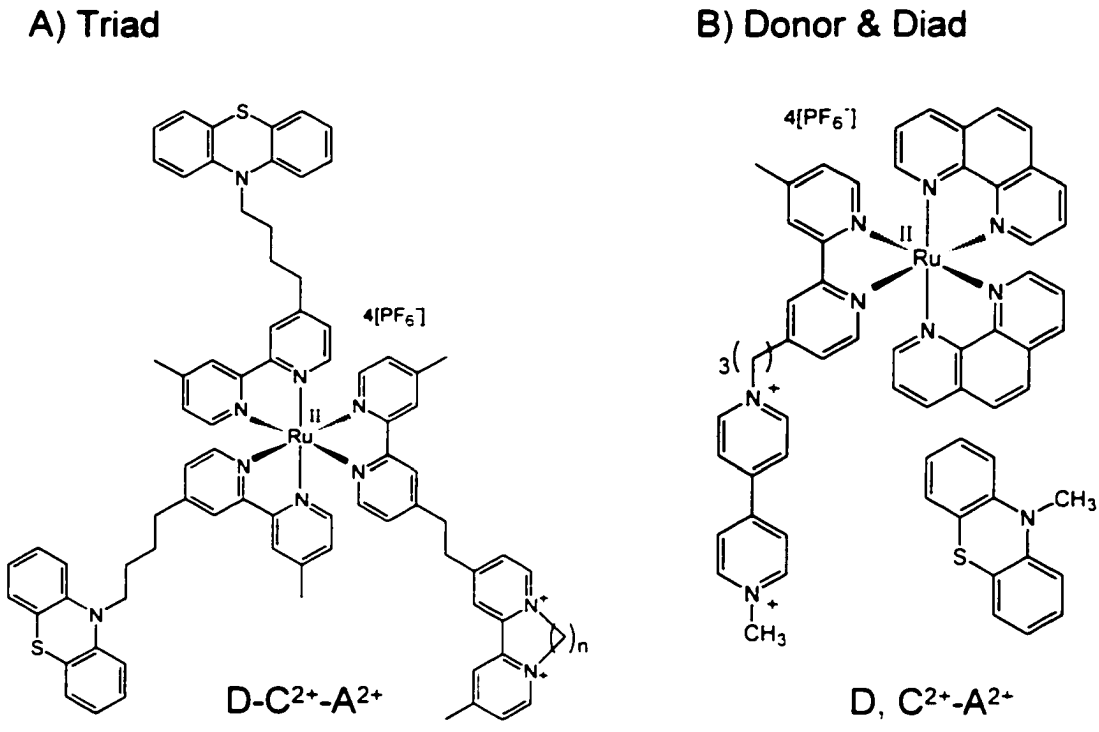

Figure 3.1. A typical triad molecule (A) consisting of two pendant phenothiazine donors, a chromophore core, and a pendant "diquat" acceptor (n = 2, 3, or 4): A typical C^{2+}-A^{2+} diad and NMPTZ (B).

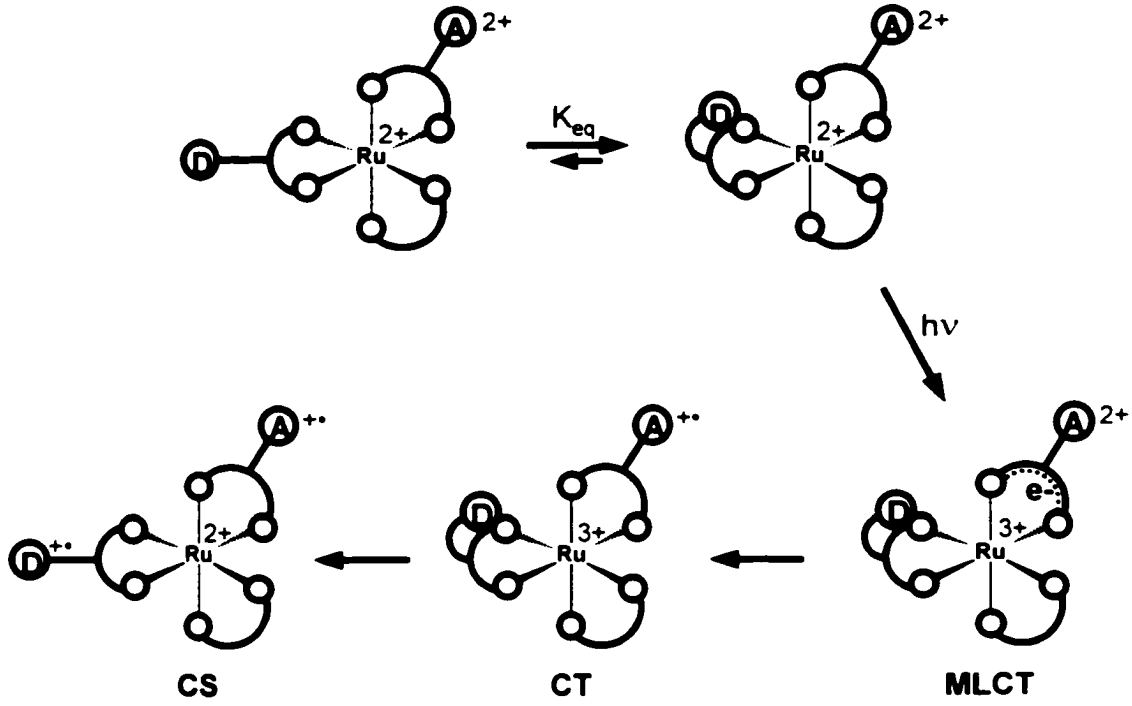

Figure 3.2. Schematic representation of photophysical processes involved in the formation of the CT and CS in triads (see text for details).

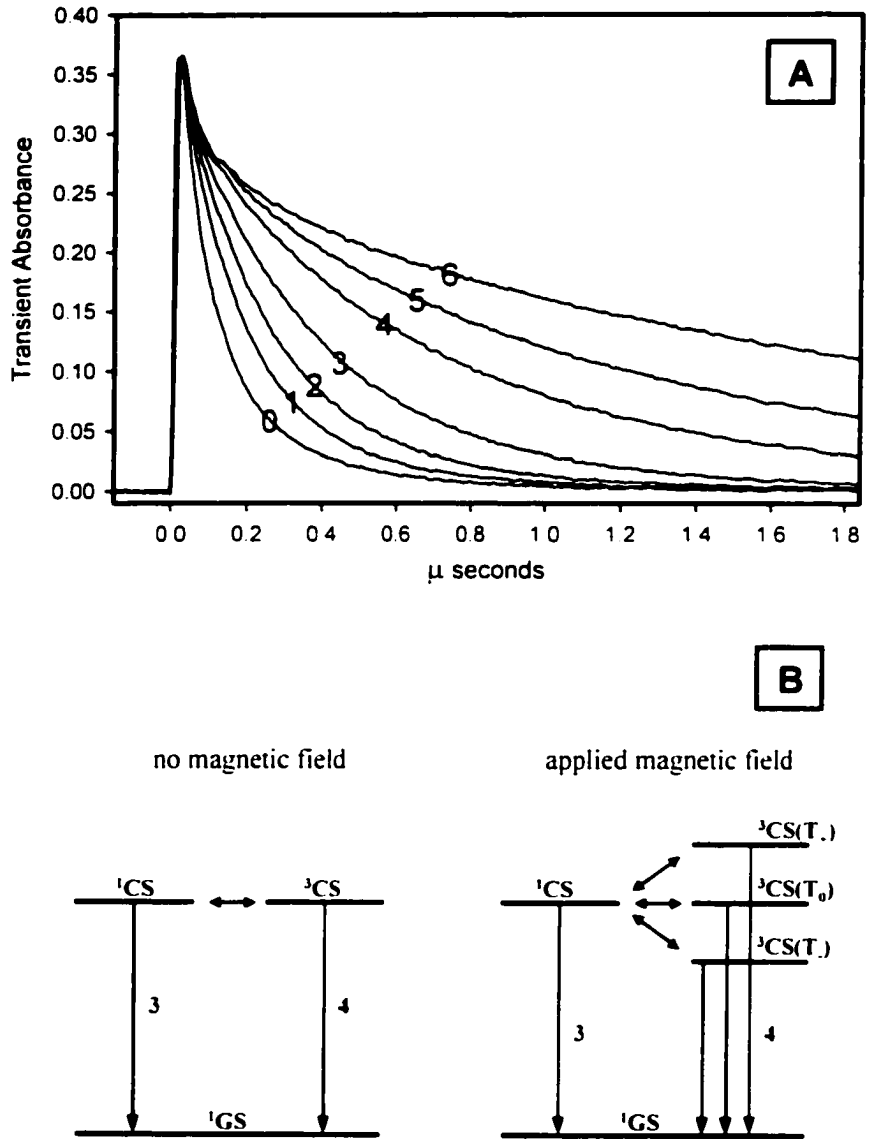

Figure 3.3. **(A)** Absorbance decay of the CS in a triad for different magnetic field strengths (see text and reference 4 for details): (0) 0T, (1) 5 mT, (2) 10 mT, (3) 20 mT, (4) 50 mT, (5) 100 mT, (6) 500 mT. **(B)** A partial energy level diagram showing the return to the ground state from the CS in a triad molecule with regard to spin multiplicity and the effects of an applied magnetic field.

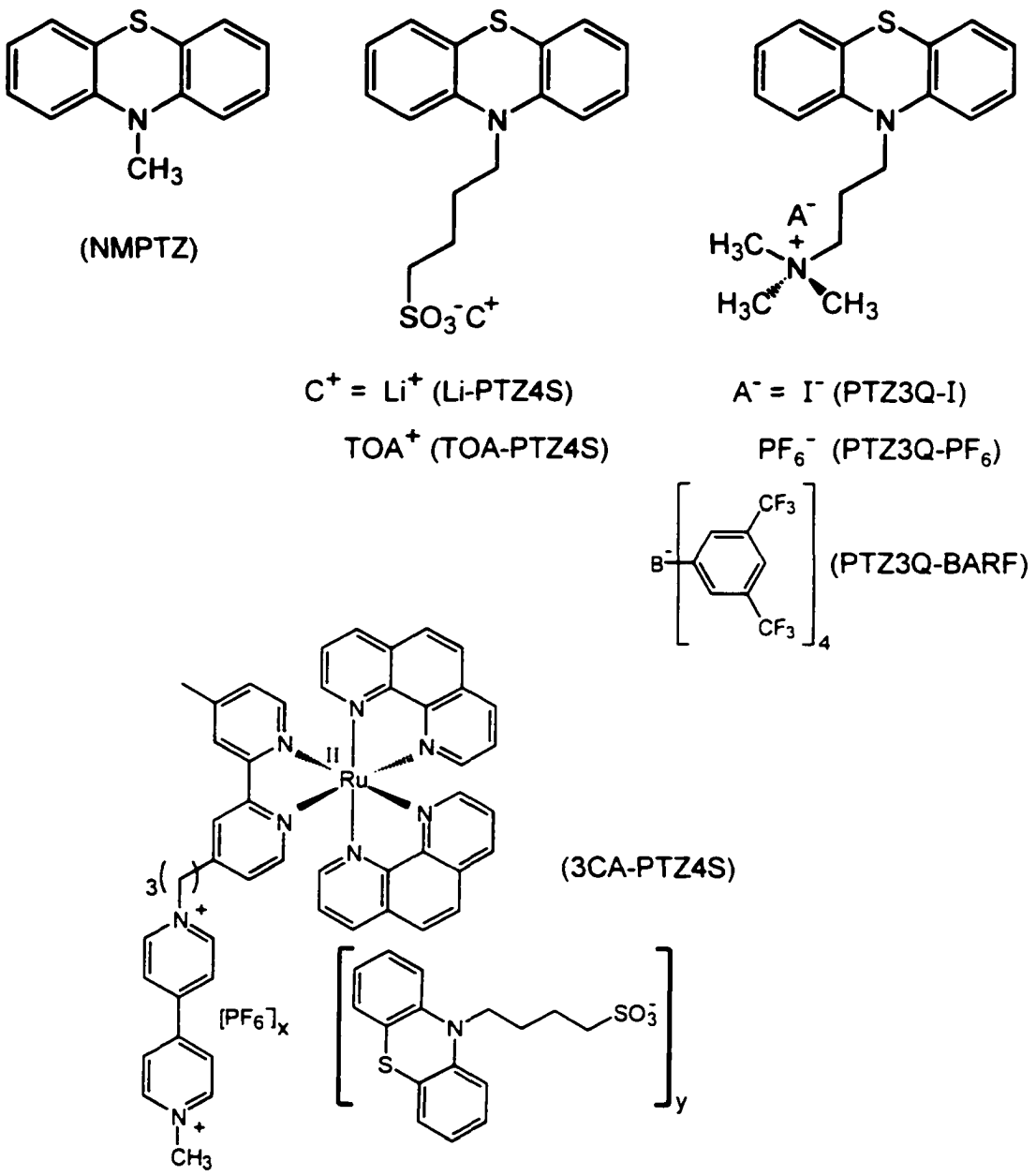

Figure 3.4. Structures of *N*-alkylphenothiazine derivatives and salts thereof referred to throughout the text.

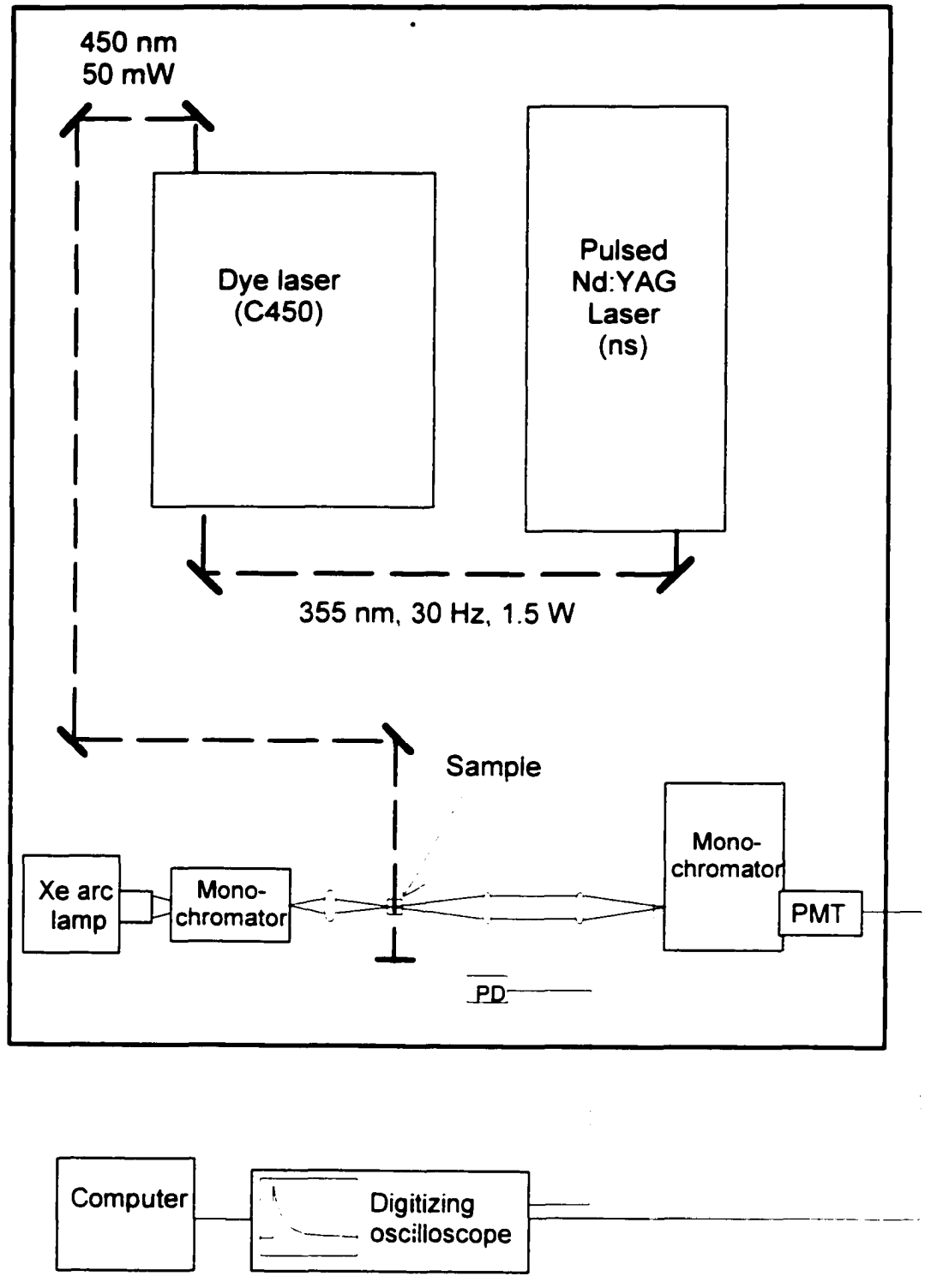

Figure 3.5. Schematic diagram of the instrumental setup for measuring transient absorption signals using a Nd:YAG-pumped dye laser for excitation, and the monochromatic output of a xenon arc lamp as an absorbance probe.

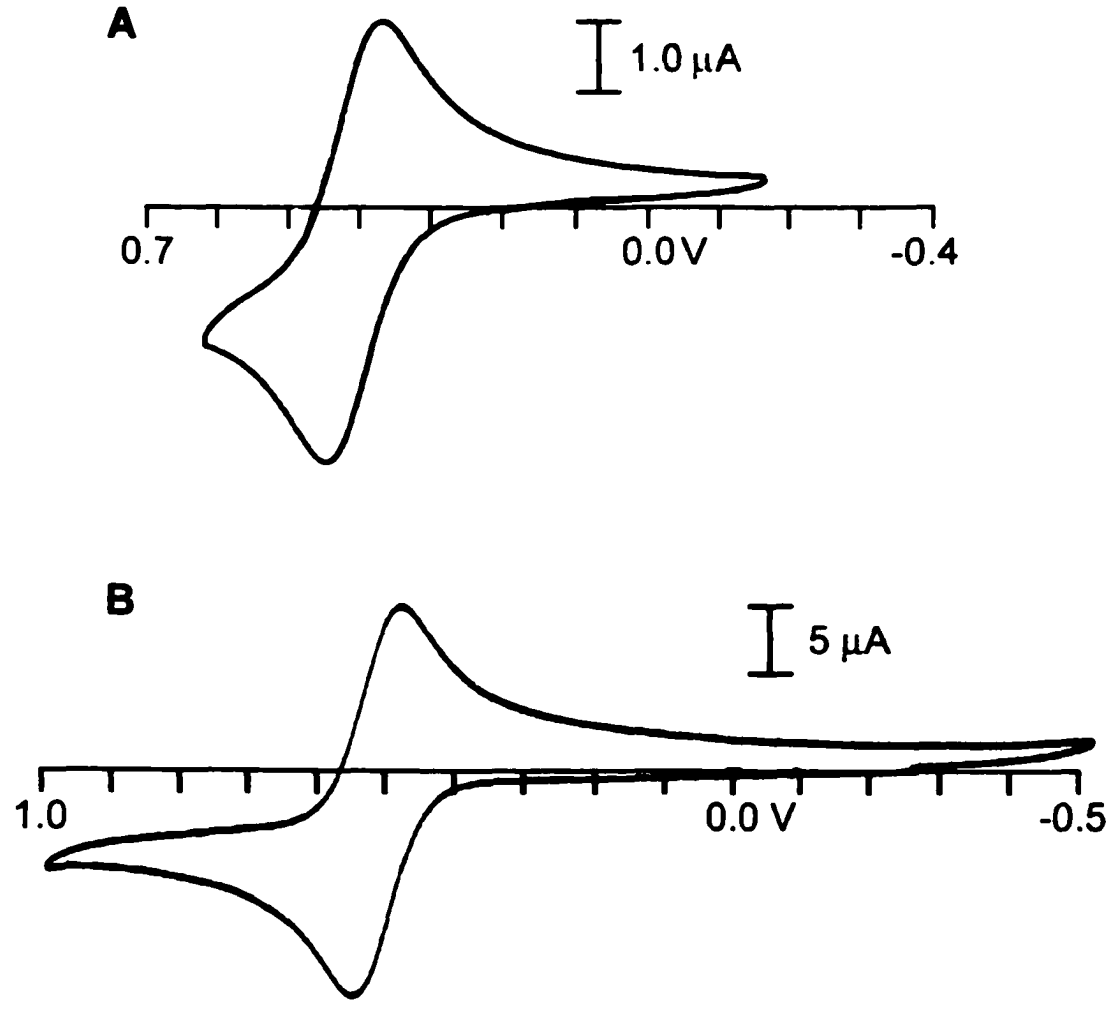

Figure 3.6. Cyclic voltammograms of ionic PTZs. The data in "A" was obtained in a propylene carbonate solution of 0.01 M Li-PTZ4S and 0.1 M $LiClO_4$ at 20 mV s^{-1}. The data in "B" was obtained in an ACN solution of 0.01 M PTZ3Q-PF_6 and 0.1 M TBA-PF_6 at 100 mV s^{-1}.

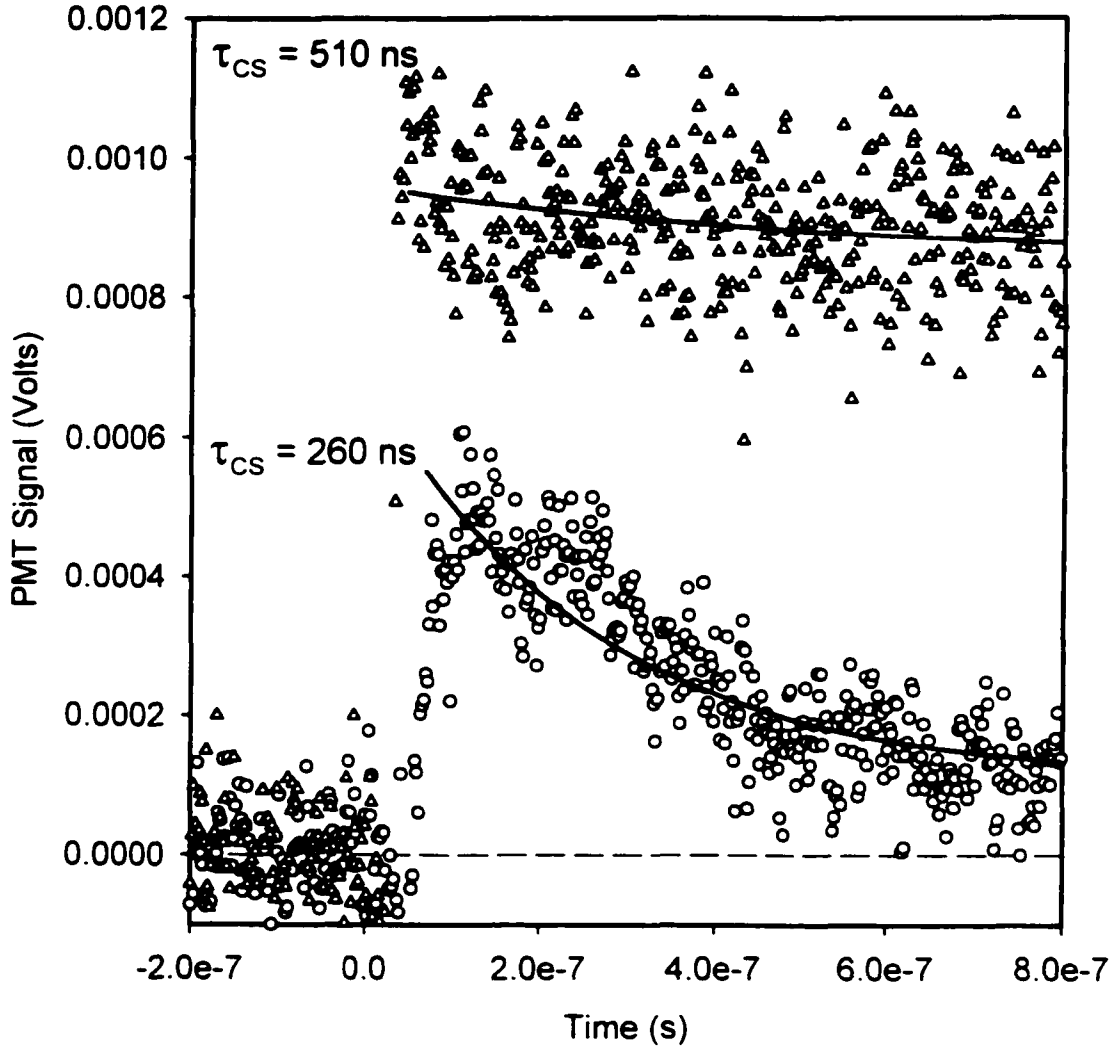

Figure 3.7. Comparison of the lifetimes of the bimolecular CS of 3CA-PF_6 in DCM with either TOA-PTZ4S (○) or PTZ3Q-BARF (△) as electron donors. The solid lines represent the single exponential fits for the data.

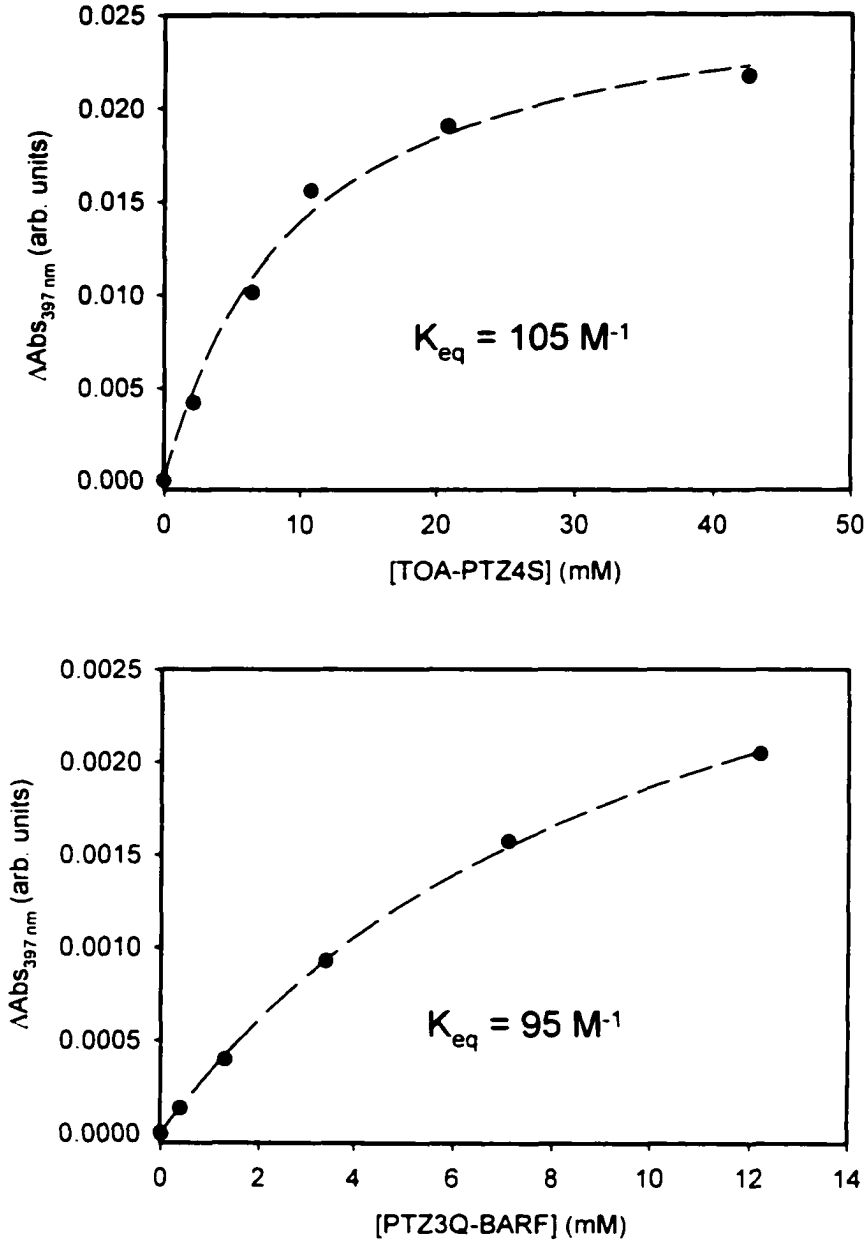

Figure 3.8. Plots of the initial ΔAbs at 397 nm of CS in DCM as a function of donor concentration. The data obtained with TOA-PTZ4S and 3CA-PF_6 is shown in the top graph. and the data obtained for PTZ3Q-BARF and 3CA-PF_6 is shown in the bottom graph. The values for K_{eq} obtained from fitting this data are also shown for each respective donor (see text for details).

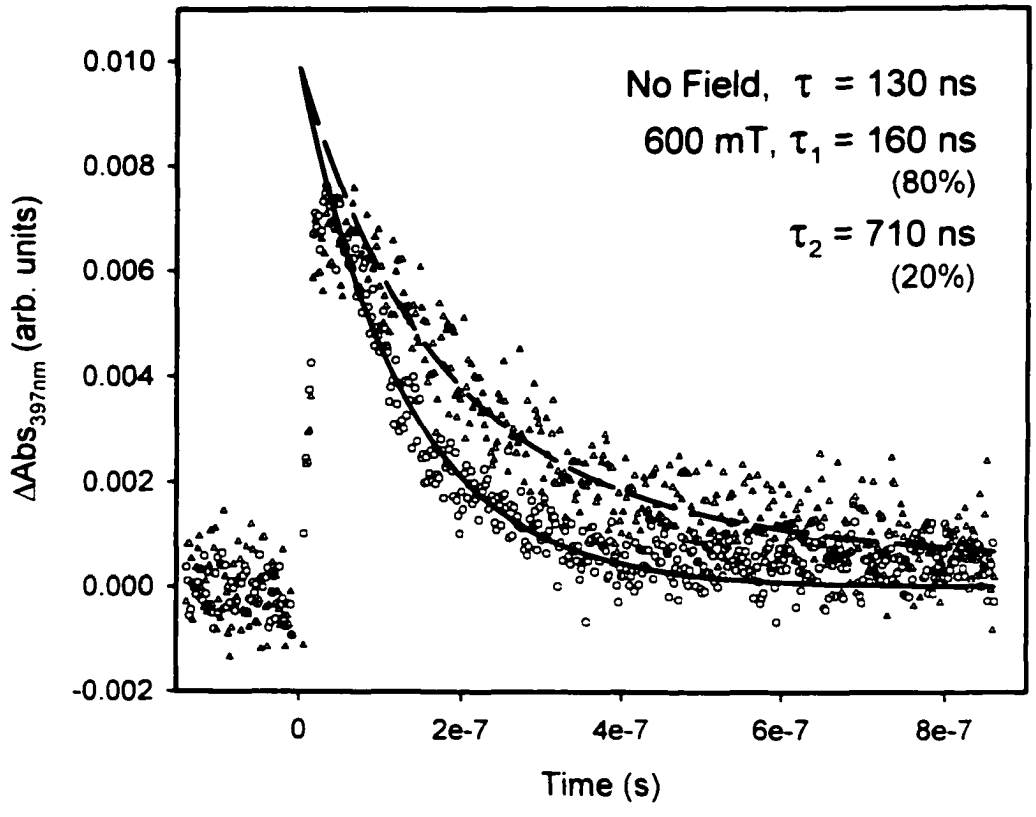

Figure 3.9. Comparison of the lifetimes of the bimolecular CS of 3CA-PTZ4S inside AOT reverse micelles in toluene with no magnetic field (○) or 600 mT magnetic field (△). The solid line represents the single exponential fit for the ○ data. The dashed line represents the double exponential fit for the △ data. To correct for differences in laser intensity between the two experiments, the magnetic field data and fit were scaled on the y-axis to match the no field data and fitted value at time = 0. The lifetime values (τ) obtained from the fits are listed in the upper right corner of the graph.

Chapter 3 References:

(1) Larson, S. L.; Elliott, C. M.; Kelley, D. F. *Inorg. Chem.* **1996**, *35*, 2070.

(2) Larson, S. L.; Elliott, C. M.; Kelley, D. F. *J. Phys. Chem.* **1995**, *99*, 6530.

(3) Larson, S. L.; Cooley, L. F.; Elliott, C. M.; Kelley, D. F. *J. Am. Chem. Soc.* **1992**, *114*, 9504.

(4) Klumpp, T.; Linsenmann, M.; Larson, S. L.; Limoges, B. R.; Burssner, D.; Krissinel, E. B.; Elliott, C. M.; Steiner, U. E. *J. Am. Chem. Soc.* **1999**, *121*, 1076.

(5) Cooley, L. F.; Larson, S. L.; Elliott, C. M.; Kelley, D. F. *J. Phys. Chem.* **1991**, *95*, 10694.

(6) Kalyanasundaram, K. *Photochemistry of polypyridine and porphyrin complexes*; 1st ed.; Academic Press: San Diego, 1992; Chapter 6 & 16.

(7) Limoges, B. R. *Ph.D. Thesis*, Department of Chemistry, Colorado State University, 2001.

(8) Weber, J. M.; MacKenzie, V. J.; Limoges, B. R.; Sapp, S. A.; Elliott, C. M. *Manuscript in preparation.*

(9) Gould, I. R.; Zimmt, M. B.; Turro, N. J.; Baretz, B. H.; Lehr, G. F. *J. Am. Chem. Soc.* **1985**, *107*, 4607.

(10) Ulrich, T.; Steiner, U. E. *Chem. Phys. Let.* **1984**, *112*, 365.

(11) Sakaguchi, Y.; Hayashi, H. *Chem. Phys. Let.* **1982**, *87*, 539.

(12) Sullivan, B. P.; Salmon, D. J.; Meyer, T. J. *Inorg. Chem.* **1978**, *17*, 3334.

(13) Yonemoto, E. H.; Riley, R. L.; Kim, Y.; Atherton, S. J.; Schmehl, R. H.; Mallouk, T. E. *J. Am. Chem. Soc.* **1992**, *114*, 8081.

(14) Bahr, S. R.; Boudjouk, P. *J. Org. Chem.* **1992**, *57*, 5545.

(15) Iwamoto, H.; Sonoda, T.; Kobayashi, H. *Tetrahedron Lett.* **1983**, *24*, 4703.

(16) Riter, R. E.; Kimmel, J. R.; Undiks, E. P.; Levinger, N. E. *J. Phys. Chem. B* **1997**, *101*, 8292.

Chapter 4.

Substituted Polypyridine Complexes of Cobalt(II/III) as Efficient Electron-Transfer Mediators in Dye-Sensitized Solar Cells.

Introduction.

It is now well documented that certain photoelectrochemical cells based on dye-sensitized nanocrystalline TiO_2 photoanodes can have total energy conversion efficiency in excess of 10% when irradiated with sunlight.[1] Such efficiencies meet or exceed those of solid-state cells based on amorphous silicon but fall far short of the efficiency of single crystal and poly-crystalline silicon cells.[2-4] That fact notwithstanding, the potential for fabricating large surface area cells out of relatively inexpensive materials—compared to single crystalline silicon cells, for example—is driving interest in dye-sensitized solar cells (DSSCs).

Although the demonstrated energy conversion efficiencies of DSSCs have become competitive with some existing commercial technologies, there are a number of issues that remain to be addressed before this type of cell can become truly commercially viable. The first issue is that the best "dyes" for sensitizing the TiO_2 photoanode are ruthenium-based coordination complexes. With such dyes there are potential stability issues. Furthermore, ruthenium is relatively rare and major known sources are geographically localized in politically unstable regions; thus, its use could pose serious practical problems. Secondly, only cells based on liquid-state electrolytes have produced the high efficiencies required for competitiveness with existing technologies.[5-9] Lastly,

an extremely limited set of electron-transfer mediators work in these cells. The overall best system to date is the I^-/I_3^- couple, which regrettably has a list of undesirable chemical properties.[10] Figure 1 depicts the basic construction and operation of an I^-/I_3^- mediated cell.

Considerable effort has been focused on finding new dyes.[11] In contrast, efforts to find electron-transfer mediators other than I^-/I_3^- have been relatively modest.[10] The I^-/I_3^- couple functions well in these cells because of a fortunate confluence of the right kinetics for at least four different heterogeneous electron-transfer reactions: (1) The photo-excited dye must inject an e^- faster than it reacts with the mediator. (2) The oxidized dye must be reduced by the mediator more rapidly than it recombines with the photoinjected electron. (3) The oxidized mediator must, itself, react slowly with electrons in both the TiO_2 and the fluorine-doped tin oxide (SnO_2:F) contact. (4) Finally, the reduction of the oxidized mediator at the cathode must be rapid (see Figure 2). At present, there is no way to predict what other systems might possess similar electron-transfer kinetics—which is most likely why this problem has been less-aggressively addressed.

Periodically, interest arises in cobalt complexes as mediators in DSSCs but many previous efforts along these lines have been disappointing.[12,13] There has also been a report of a cobalt complex-based mediator that rivaled the I^-/I_3^- mediator in terms of the kinetics to regenerate the dye.[14] However, the ligands used to form this complex are not readily available, and we assume they were obtained using a multi-step synthetic procedure.[14]

We have recently discovered that particular cobalt polypyridine complexes—formed from structurally simple ligands—do function as efficient electron-transfer mediators in

DSSCs. Figure 3 shows the structures of a series of cobalt polypyridine complexes synthesized in our labs in order to identify what structural and thermodynamic motifs generate the best mediators. The focus of this investigation was not to generate the highest efficiency cells possible, but rather to generate cells with cobalt complex mediators that closely match the performance of comparable I^-/I_3^- mediated cells. In the best case so far, the cobalt-based mediators reported here give efficiencies greater than 80% of that given by the comparable cell mediated by the I^-/I_3^- couple.

Experimental Section.

Materials. Acetonitrile (Fisher Optima Grade), anhydrous ethanol (Pharmco), and all other solvents (Fisher ACS Grade) were used as received. Cobalt(II) perchlorate hexahydrate, 10% palladium on activated carbon, γ-butyrolactone, thionyl chloride, *t*-butyl alcohol, dibutylamine, 4-*t*-butylpyridine, 2,2'-dipyridyl, 4,4'-diphenyl-2,2'-dipyridyl, 4,4'-di-*t*-butyl-2,2'-dipyridyl, 4,4'-dinonyl-2,2'-dipyridyl, 4,4',4"-tri-*t*-butyl-2,2':6',2"-terpyridine, 1,10-phenanthroline, 4,7-diphenyl-1,10-phenanthroline, silver nitrate, lithium perchlorate, lithium triflate, and nitrosonium tetrafluoroborate were purchased from Aldrich at ≥97% purity and used as received. 3-methoxypropionitrile (Aldrich 98%) and 4-(3-pentyl)pyridine (TCI 95+%) were distilled under dynamic vacuum prior to use. 4,4'-dimethyl-2,2'-dipyridyl was purchased from Reilly Industries, Indianapolis. 5,5'-dimethyl-2,2'-dipyridyl, and 4,4',5,5'-tetramethyl-2,2'-dipyridyl were prepared as described previously.[15] All methyl-substituted bipyridines were recrystallized from ethyl acetate. 2,2'-bipyrine-4,4'-dicarboxylic acid,[16] 4,4',4"-triethyl-2,2':6',2"-terpyridine,[1] and *cis*-di(isothiocyanato)-bis(2,2'-bipyridine-4,4'-dicarboxylic acid) ruthenium(II) (N3)[17] were prepared according to previously published procedures.

Synthesis of 4,4'-di-(3-pentyl)-2,2'-dipyridyl. Freshly distilled 4-(3-pentyl)pyridine (18 mL) was refluxed with 2 g of 10% Pd on activated carbon under nitrogen for 5 days. After cooling the mixture to room temperature, the solids were filtered and rinsed with dichloromethane (DCM). The solvent in filtrate was then removed by rotary evaporation. Most of the unreacted 4-(3-pentyl)pyridine was removed by vacuum distillation. The remaining viscous oil was subjected to flash column chromatography using silica gel. The eluent was a gradient of acetone in DCM that was saturated with concentrated ammonium hydroxide solution. Combining and reducing the volume of the product containing fractions resulted in 2.7 g (16% yield) of 4,4'-di-(3-pentyl)-2,2'-dipyridyl in the form of a nearly colorless viscous oil that solidified into a waxy crystalline solid on standing at room temperature.

^{1}H NMR (300 MHz, $CDCl_3$) δ ppm: 0.81 (12H, t, 4× CH_3), 1.73 (8H, m, 4× CH_2), 2.50 (2H, m, 2× CH), 7.16 (2H, s, 2× H5), 8.34 (2H, s, 2× H3), 8.61 (2H, d, 2× H6).

Synthesis of 2,2'-bipyridine-4,4'-dicarboxylic acid chloride. Approximately 10 g of 2,2'-bipyridine-4,4'-dicarboxylic acid was placed in a 500 ml round-bottom flask fitted with a condenser. Thionyl chloride (ca. 200 ml) was added and the flask flushed with N_2. The solution was heated at reflux under a static N_2 atmosphere with stirring for three to four days. The solution was allowed to cool and the solids settle. Approximately 50 ml of the clear yellowish solution was decanted into a clean 250 ml flask being careful not to transfer any of the un-reacted solid. The thionyl chloride was removed by rotary evaporation leaving a slightly yellow-green solid on the sides of the flask. This product was used immediately without characterization or further purification.

Synthesis of 2,2'-bipyridine-4,4'-di-*t*-butoxyester. From a freshly opened bottle that had previously been warmed to melt the contents, ca. 20 ml of t-butyl alcohol was transferred to a clean, dry Erlenmeyer flask. A piece of sodium (ca. 1g) was washed several times with t-butyl alcohol and added to the Erlenmeyer flask. The flask was warmed with stirring under N_2 until the sodium had totally dissolved (ca. 1.5 hrs). This solution of sodium *t*-butoxide was then added to the flask containing the 2,2'-bipyridine-4,4'-dicarboxylic acid chloride. The flask immediately became hot to the touch. The resulting slurry was stirred for 30 min. and allowed to cool to room temperature. The solution was then filtered and the solid was washed with several portions of DCM.

The solution fractions were combined and the solvent removed by rotary evaporation leaving a yellowish solid on the sides of the flask. This solid consisted of the desired product, the monoacid-monoester bipyridine and a small amount of dicarboxylic acid bipyridine. The desired product was extracted from the solid mixture by adding several 10 ml portions of toluene to the flask and heating with swirling with a heat gun until the start of reflux. The toluene was then allowed to cool to room temperature before decanting from the solid residue. This processes was repeated until the toluene no longer tested significantly positive for dissolved bipyridine (by adding several drops to a solution of $Fe(ClO_4)_2 \cdot X\ H_2O$ in acetone which turns red-purple if the product is present). The toluene fractions were combined, the volume reduced to a few milliliters, and the solution was placed in a freezer. White, waxy crystals formed and were filtered from the cold solution. The product thus obtained was pure by thin layer chromatography (~ 1 g).

^{1}H NMR (300 MHz, $CDCl_3$) δ ppm: 1.65 (18H, s, 6× CH_3), 7.85 (2H, d, 2× H5), 8.84 (2H, m, 2× H3, 2× H6).

Synthesis of 2,2'-bipyridine-4,4'-bis-(di-*n*-butylamide). Approximately 20 ml of di-*n*-butylamine was added to a flask containing the 2,2'-bipyridine-4,4'-dicarboxylic acid chloride and the flask swirled for several minutes. After the reaction mixture cooled, approximately 100 ml of chloroform was added to the flask. This solution was extracted several times with aqueous NaOH. The organic layer was collected, dried with anhydrous sodium carbonate and reduced to a few milliliters. The crude product was chromatographed on silica gel using a gradient of acetone in DCM. The product obtained by removing the chromatography solvent was a white residue that had to be scraped from the sides of the flask. Estimated yield was ~1 g.

^{1}H NMR (300 MHz, $CDCl_3$) δ ppm: 0.81 (6H, t, 2× CH_3), 1.02 (6H, t, 2× CH_3), 1.15 (4H, two offset quintets, 2× CH_2), 1.43 (4H, two offset quintets, 2× CH_2), 1.52 (4H, quintet, 2× CH_2), 1.68 (4H, quintet, 2× CH_2), 3.20 (4H, t, 2× CH_2), 3.51 (4H, t, 2× CH_2), 7.30 (2H, m, 2× H5), 8.41 (2H, s, 2× H3), 8.74 (2H, m, 2× H6).

Synthesis of $[Co^{II}(L)_3]\{ClO_4\}_2$ and $[Co^{II}(L')_2]\{ClO_4\}_2$ complexes. All of the complexes depicted in Figure 3 were synthesized using the same procedure. Briefly, 3 equivalents of a bidentate ligand or 2 equivalents of a tridentate ligand were dissolved with magnetic stirring in refluxing methanol. The volume of methanol was adjusted according to the solubility of the ligand and the scale of the reaction such that all of the ligand material was dissolved. To this mixture was then added 1 equivalent of cobalt(II) perchlorate hexahydrate and the mixture was allowed to stir at reflux for 2 hours. After cooling the mixture to room temperature, the total volume was reduced by ca. 80% using rotary evaporation. Addition of ethyl ether caused the precipitation of the product (as a

solid that varied from light brown to light yellow), which was filtered and dried under vacuum. The resulting complexes were used without any further purification.

Dye Solutions. Saturated solutions of N3 were prepared by adding ca. 4 mg of dye to 10 ml of dry ethanol. This mixture was sonicated for ca. 10 minutes and filtered to remove undissolved dye.

Electrode Preparation. TiO_2 colloidal solutions were prepared either according to "Method A" reported by Nazeeruddin et al.[17] or according to the method reported by Zaban et al.[18] and will be referred to as the nitric acid or acetic acid preparation, respectively. Films of the colloid were coated onto SnO_2:F coated glass electrodes (Pilkington TEC 15) using the "1 Scotch" method. Zaban et al. described this technique in detail.[18] After coating, the films were air-dried and then sintered in air at 450 °C for 1 hour. The still hot electrodes (ca. 80 °C) were then immersed in the dye solution and allowed to sit in the dark at least overnight. Photoanodes were kept in the dark and in the dye solution until needed. Just prior to use, they were removed from the dye solution, rinsed thoroughly with dry ethanol, and dried under a stream of nitrogen. In some cases, the photoanodes were further treated by immersing into a 0.5 M solution of 4-*t*-butylpyridine in acetonitrile (ACN) for 10-30 minutes followed by rinsing in ACN just prior to use.

Platinum-on-glass electrodes, made by a sputtering process, were donated by Dr. Suzanne Ferrere at the National Renewable Energy Laboratories in Golden, Colorado. Gold-on-glass electrodes were made by thermal vapor deposition of 25 nm chromium followed by 150 nm gold on glass. Carbon-coated electrodes were made by spraying 3-5 coats of Aerodag G (Acheson) on SnO_2:F electrodes. The carbon coating produced in

this way was very fragile, and each electrode could only be used in a cell once, as cell disassembly usually created large scratches in the carbon film.

Mediator Preparation. Cobalt-based mediators were created by the addition of the desired Co(II) complex at various concentrations in either 3-methoxypropionitrile (MPN) or γ-butyrolactone (gBL). In all cases, the appropriate amount of nitrosonium tetrafluoroborate ($NOBF_4$) was added to oxidize 10% of the added Co(II) complex. In some cases, 0.2 M 4-*t*-butylpyridine was added to the mediator solutions. Lithium triflate or $LiClO_4$ was also added at various concentrations to some mediator solutions. For the purposes of comparison, a standard iodide-based mediator solution was prepared that consisted of LiI and I_2 (10:1) in MPN.

Analytical Measurements. UV-vis spectra were obtained using a HP 8452A diode array spectrophotometer. A reduced volume, 1 cm path length, quartz cell was used for measurement of all solutions. Cyclic voltammetric data was obtained using a standard three-electrode cell with an EG&G PAR Model 173 Potentiostat/Galvanostat controlled by a Model 175 Universal Programmer. The data was recorded on a Yokogawa 3023 X-Y recorder. The reference electrode was Ag/Ag^+ (0.47 V vs. SHE) composed of 0.1 M silver nitrate in dimethylsulfoxide. The auxiliary electrode was a 0.5 cm^2 platinum flag and the working electrode was a glassy carbon (7.1×10^{-2} cm^2), gold (7.1×10^{-2} cm^2), or platinum (2.8×10^{-2} cm^2) disk electrode (BAS). Prior to use, each working electrode was polished on a felt pad with a water slurry of 0.3 μm alumina polishing powder, followed by rinsing and sonication in ACN. This polishing procedure was repeated before each electrochemical experiment. The supporting electrolyte was 0.1 M lithium perchlorate in ACN.

Photoaction spectra were obtained from DSSCs in a two-electrode sandwich cell arrangement. Typically 10 μl of electrolyte was sandwiched between a TiO_2 photoanode and a counter electrode. When solutions of the different cobalt mediators (0.25 M Co(II) / 0.025 M $NOBF_4$) in MPN were used, the counter electrode was made of gold-sputtered on SnO_2:F-coated glass. A platinum-sputtered SnO_2:F-coated glass electrode was employed as a counter electrode when the redox mediator was 0.25 M LiI / 0.025 M I_2. The cell was illuminated with a 150 W Xe lamp coupled to an Applied Photophysics high irradiance monochromator. The irradiated area was 0.5 cm^2. Light excitation was through the SnO_2:F-coated glass substrate of the photoanode. Photocurrents were measured under short circuit conditions with a Contron model DMM 4021 digital electrometer. Incident irradiance was measured with a calibrated silicon photodiode from UDT Technologies.

To test the performance of each electron-transfer mediator solution, cells were assembled by clamping together a photoanode and cathode in a specially designed cell holder having a light aperture area of 0.4 cm^2. The electron-transfer mediator was introduced by the addition of a few drops of solution at the edge of the electrodes. Capillary forces were sufficient to draw the solution onto the entire electrode area. Solar illumination was simulated using the output of an Oriel 75 W xenon arc lamp which was further attenuated using neutral density filters and a 400 nm high-pass cutoff filter. The light intensity after filtering was adjusted to 100 mW cm^{-2} (ca. 1 sun) at the distance of the photoanode using a Molectron PowerMax 500A power meter. The current output of each cell was recorded in the dark and under solar illumination while sweeping the voltage between ca. 0.8 and -0.2 V using the same instrumentation as was used for cyclic

voltammetry. The data thus obtained was digitized using an Acer flatbed scanner and tsEdit digitizing software on a computer running under Windows® 98.

Results and Discussion

Ligands. Cobalt complexes of unsubstituted and methyl-substituted bipyridine or terpyridine ligands are poor electron-transfer mediators in the type of DSSCs considered herein. In contrast, if the ligand contains a tertiary butyl substituent in the position para to each nitrogen, the resulting cobalt complex-based mediators yield cells with quite good short circuit photocurrent densities (J_{sc}) and open circuit photovoltages (V_{oc}). Were these substituent effects electronic in origin, then ligands substituted with methyl groups should produce similarly good mediators (*vide infra*) and they do not. Consequently, we initiated this study assuming that the difference in mediator behavior of *t*-butyl-substituted polypyridine ligands was related to the steric bulk of the *t*-butyl group. Three types of polyimine ligands were examined: 2,2'-bipyridines, 1,10-phenanthrolines and 2,2':6',2"-terpyridines. Alkyl substituents having a range of steric requirements were examined. Since the electron-donating effect of all simple alkyl substituents is essentially the same (e.g., methyl, ethyl, *t*-butyl, etc.),[19] all of the complexes of a given ligand-type (i.e., bipyridine, phenanthroline or terpyridine) were expected and found to have very similar $E_{1/2}$ values for the relevant Co(II/III) couple. In addition, several other types of bulky substituents were examined which have significantly different electronic effects. This group included aryl substituents and strongly electron-withdrawing ester and amide groups. These latter two types of substituents make the ligands electron-deficient and produce cobalt complexes with significantly more positive $E_{1/2}$ values; consequently, the maximum theoretically possible V_{oc} is likewise greater.[11]

Spectral Properties. All of the complexes under consideration exhibit similar UV-vis absorption spectra. Each of the Co(II) complexes has a weak absorption band centered at ca. 440-450 nm. The onset of the ligand-based π-π^* transition occurs in the UV above 350-380 nm for each of the ligands. Molar extinction coefficients ($\varepsilon_{\lambda,max}$) for the band at 440-450 nm were obtained from Beer's law plots of standard solutions of each Co(II) complex. Table 1. summarizes the data for a set of representative complexes. The most intense visible absorption is for ttb-terpy^{2+} with $\varepsilon_{450} = 1.4 \times 10^3$ M^{-1} cm^{-1}. The remaining complexes all exhibit $\varepsilon_{\lambda,440-450}$ values that are approximately an order of magnitude smaller. In all cases, the visible absorbance of the Co(III) form is almost imperceptible and partial oxidation of solutions of any of the Co(II) complexes reduces the overall absorbance. For the sake of comparison, the $\varepsilon_{\lambda,440-450}$ value for I_3^- is ca. 2×10^3 M^{-1} cm^{-1}; therefore, except for ttb-terpy^{2+} that has a comparable absorbance, considerably less visible light is absorbed by all of the remaining cobalt complexes at similar concentrations.

Electrochemical Studies. Electrochemical characterization of these complexes revealed a dramatic and unexpected electrode surface dependence to the electron-transfer kinetics. Each complex was examined by cyclic voltammetry on three different working electrodes: glassy carbon, gold, and platinum. Figure 4 shows nine cyclic voltammograms (CVs) representing three different complexes (rows) on the three different working electrode surfaces (columns). The vertical axis in these CVs was converted to current density to normalize for the different electrode areas. Table 2. contains the measured electrochemical parameters for the complete set of complexes.

The results found for 4,4'-dmb and dtb-bpy (Figure 4, top and middle rows, respectively) are typical of complexes with ligands containing alkyl substituents in the 4 and 4' (or equivalent) positions. Gold electrodes exhibit the most reversible and ideally shaped CVs. Glassy carbon electrodes also produce quasi-reversible voltammograms, although less reversible than gold. Quite unexpectedly, the voltammetry on platinum electrodes is quite irreversible with large anodic and cathodic peak separations (ΔE_p) or, in some cases, peaks that are so broad as to be indistinguishable as peaks. In contrast, the voltammetry of the dtb-est complex (Figure 4, bottom row), is most reversible on glassy carbon with ΔE_p increasing on gold and platinum.

Complexes whose ligands are either unsubstituted or are substituted only in the 5 and 5' positions with methyl groups exhibited very different behavior (see Table 2). In general, there is a less dramatic surface dependence. Gold and platinum electrodes give nearly reversible voltammograms while the CVs on glassy carbon are quasi-reversible.

In general, the shapes of the quasi-reversible waves indicate that, in cases where the heterogeneous electron transfer is slow, the transfer coefficient, α, is considerably greater than 0.5.[20] In other words, for equivalent overpotentials the heterogeneous reduction of the Co(III) complex is considerably faster than the corresponding oxidation of the Co(II) species. While the electrode-dependant electron-transfer kinetics are not presently understood, there is a rough empirical correlation between the solution voltammetry of a complex and its performance as a redox mediator in a DSSC. The complexes that exhibit reversible or nearly reversible voltammetry on all three electrodes are generally poor mediators; i.e., they give very low J_{sc} values. The voltammetric results also suggest that, while platinum is the cathode of choice for the I^-/I_3^- redox mediator, it should *not* be the

optimal choice for cobalt complex-based mediators. Likewise, although carbon is a poor cathode with the I^-/I_3^- redox mediator system, it should be acceptable for any of the cobalt systems considered here.

Initial Screening of Mediators. To qualitatively and quantitatively compare these cobalt complexes as mediators, DSSCs were assembled using identical photoanodes and cathodes. Due to the varying solubility of the complexes, the concentration of mediator in solution was kept low. This resulted in devices with less than optimal performance, but allowed for comparisons in cell performance as a function of mediator structure.

As with the electrochemical observations, there were distinct differences in cell performance based on the identity of the ligand substituents and in what positions they were located. Mediators based on phen, phen-phen, bpy, 5,5'-dmb, or tm-bpy yielded almost no photocurrent. Mediators composed of 4,4'-dmb and te-terpy resulted in a very modest photoeffect, but both V_{oc} and J_{sc} were very low and further investigation with these complexes was considered unwarranted. Both dtb-est and bdb-amd gave $V_{oc} > 0.55$ V but J_{sc} that were ca. <10% that of the best cobalt-based systems. The remaining complexes under consideration showed promise as potential efficient mediators and efforts were focused on optimizing DSSCs containing the best of these.

Solvents and Cathode Materials. In surveying a number of potential low volatility solvents, MPN and gBL were found to work well with all of the cobalt mediators. For any given concentration of mediator, gBL was generally a superior solvent, in that the fill factor (FF) was improved over the same cell made with MPN as the mediator solvent. However, in some cases the mediators were more soluble in MPN, and in those cases the higher concentration of mediator made for better cell performance.

Based on the CV results, we predicted that gold cathodes would give higher J_{sc} than platinum; this was indeed found to be the case. For all the efficient cobalt complex mediators, cells assembled using gold cathodes outperformed those assembled with platinum. However, platinum gave better results than might have been anticipated from the voltammetry. In all of our studies there was no evidence that the cobalt complexes were in any way corrosive towards the gold surface. In fact, the same gold cathode was used throughout the course of these investigations, and remains unchanged.

Again, based on the CV results, we anticipated that a carbon cathode should also work well in these cells. To that end we prepared cathodes consisting of SnO_2:F glass coated with a thin layer of graphite nanoparticles. These carbon-coated cathodes work well initially, even outperforming platinum, but they are not stable for extended periods because the layers of graphite particles are not held together with any binder and are readily damaged (this is especially evident when the cell is disassembled). Nevertheless, these results demonstrate the proof-of-concept that a stable carbon cathode should function well in cells based on these cobalt mediators.

Photoaction Spectra. Photoaction spectra—incident photon-to-current conversion efficiency (IPCE) versus wavelength—of N3 bound to nanocrystalline TiO_2 films in the presence of different electron-transfer mediators in MPN solutions are shown in Figure 5. The performances of the photoelectrochemical cell are observed to be strongly dependent on the composition of the electrolyte solution. A maximum conversion efficiency of ca. 80%, in correspondence to the metal-to-ligand charge-transfer absorption maximum of N3 was obtained in the presence of 0.25 M LiI / 0.025 M I_2. With the cobalt complex mediators, the best performances were observed when solutions of ttb-terpy^{2+} / ttb-terpy^{3+}

(ca. 55% IPCE) and dtb-bpy^{2+} / dtb-bpy^{3+} (ca 50% IPCE) were used. In the other investigated cases, the phen, te-terpy, and 44'-dmb complex-based mediators exhibited maximum IPCE values in the range of 10-20%.

Open-Circuit Voltage. Figure 6 shows V_{oc}, $E_{1/2}$ and J_{sc} data for five different cobalt bipyridine mediators plotted against the number of carbons in the substituents. In each case, the substituent is either an aryl or alkyl group that is appended at the 4 and 4' positions. These measurements were all made using MPN as the solvent. The mediators were all 125 mM in $Co(II)L_3$ and 13 mM in $Co(III)L_3$ and nothing else was added to the solution (i.e., no other cations were present and the solution contained no pyridine type bases). It is interesting that within this limited set of complexes at least, there is no obvious correlation between V_{oc} and $E_{1/2}$. On the other hand, there is a steady increase in the value of V_{oc} with the number of carbons in the ligand's substituents, which appears to be asymptotically approaching a limiting value. In the most generally accepted description,[11,21,22] V_{oc} is the difference of the quasi-Fermi level of electrons at the negative electrode and the "holes" at the positive electrode. This latter term is essentially the Nerstian potential of the cobalt couple at the cathode. All of the 4,4'-alkyl and 4,4'-aryl substituted bipyridine complexes herein have similar $E_{1/2}$ (within ca. 60 mV), so they should all yield the same V_{oc}, all else being equal. The fact that V_{oc} varies by ca. 400 mV over this collection of mediators indicates that something must shift the Fermi energy of the electrons in the TiO_2. The two most obvious candidates are shifts in the conduction band edge of the TiO_2 or differences in the rates of electron/$Co(III)L_3$ recombination. With I^-/I_3^-, numerous studies have demonstrated that V_{oc} depends on the size of the countercation of iodide.[23-25] This effect is ascribed to a shift in the conduction band edge

energy of TiO_2 upon adsorption and/or intercalation of cations; and the magnitude of this shift is related to the charge-to-radius ratio of the cation. The complexes considered in Figure 6 are of different sizes and the trend in V_{oc} is in the correct direction to be consistent with this model (i.e., V_{oc} increases with larger radius). Furthermore, Nusbaumer et al. have shown that a related cobalt complex-based mediator does adsorb on the TiO_2 surface.[14] While this picture is in qualitative agreement with the model, it does not stand up to a more quantitative analysis. With I^-/I_3^-, the typical shift in V_{oc} upon changing between Li^+ and Cs^+ is less than 200 mV (at comparable concentrations) while their ionic radii differ by almost a factor of ×3.[24] The difference in V_{oc} between bpy and dn-bpy mediated cells is ca. 400 mV but their radii differ by, at most, a factor ×2. More likely the variations in V_{oc} arise from differences in the recombination rate between $Co(III)L_3$ and photoinjected electrons, which should decrease as the bulk of the substituents increases (*vide infra*).

Lithium Ion Effect. As considered above, the presence of small countercations (most notably Li^+) in mediator solutions of I^-/I_3^- lowers V_{oc}. Concomitantly, J_{sc} increases, and the net result is an overall improvement in cell efficiency (η).[23] There is ample experimental verification that adsorbed Li^+ lowers the energy of acceptor states in the TiO_2; and this fact is the most commonly invoked explanation for the cation-induced decrease in V_{oc}.[23] The origin of the increased J_{sc} upon addition of Li^+ to the I^-/I_3^- is less clear. Photoinjection of electrons from the excited dye occurs with near unity quantum efficiency irrespective of the cation. Since the photocurrent is determined by the difference between the photoinjection rate and the overall recombination rate, any

increase in J_{sc} must lie in cation-induced changes in recombination rates (irrespective of the type of mediator system).

In principle, Li^+ could decrease recombination in at least three ways: (1) by accelerating the rate of oxidized dye reduction by I^-, (2) by slowing the rate of direct combination of electrons with the dye or (3) it could slow the rate of recombination of electrons with I_3^-. Grätzel et al. showed that Li^+ (and other cations with high charge-to-radius ratios) greatly accelerate the rate of reaction between I^- and adsorbed photooxidized N3.[26] In practice, for the I^-/I_3^- system this is largely irrelevant to J_{sc} because, at usual I^- concentrations, the rate of reaction between oxidized N3 and I^- is fast even in the absence of Li^+.[26] Consequently, neither processes (1) or (2) above should significantly factor in to determining J_{sc}, which leaves the recombination reaction of electrons with I_3^- as the dominant factor. The Li^+-induced lowering of the acceptor state energies in the TiO_2 could result in a driving-force-based decrease in the rate of I_3^- reduction at the photoanode. Alternately, and most probably, adsorbed cations affect the rate and or mechanism of the heterogeneous electron transfer in some undetermined way.

The addition of Li^+ to solutions of the cobalt-based mediators also increases J_{sc} significantly, and Figure 7 shows the current-voltage response of cells demonstrating this effect. The analogous three processes considered above remain relevant. In the discussion of V_{oc} below, data is presented that strongly indicates that Li^+ has a marked effect on the recombination rate with $Co(III)L_3$. Quite possibly this is the dominant process which determines both J_{sc} and V_{oc}. However, there is presently insufficient data to totally eliminate the other two processes from consideration.

In clear contrast to I^-/I_3^-, Li^+ *increases* V_{oc} with all of the efficient cobalt mediators. It seems highly unlikely that the presence of the cobalt complex in solution would alter the effect of Li^+ in lowering the energy of the TiO_2 acceptor states (conduction band or surface states). Consequently, the Li^+-induced increase in V_{oc} must come from some other source. Moreover, the effect must be large enough to offset the band shift to lower energy. First, Li^+ has a negligible effect on the $E_{1/2}$ of the $Co(II/III)L_3$ couple at the cathode so that cannot be the origin of the increase in V_{oc}. As with the increase in J_{sc}, the remaining obvious possibilities are directly tied to the recombination processes discussed at the beginning of this section.

Even though the rate of oxidized N3 regeneration by I^- appears to not play a significant role in recombination,[26] the rate of regeneration is greatly increased by the presence of Li^+ (*vide supra*). At present for our cobalt complex mediators, there is no data on how Li^+ affects the relative rates of reaction between the oxidized N3 dye and either the photoinjected electron or $Co(II)L_3$. So just as in the consideration of J_{sc}, these processes cannot be discounted in terms of their potential effect on V_{oc}. Given that caveat, there is evidence that the recombination reaction at the SnO_2:F contact is affected by Li^+. On a bare SnO_2:F electrode of the same type used as the TiO_2 current collector, the overpotential for dtb-bpy^{3+} reduction is several hundred millivolts more negative in the presence of 0.25 M Li^+ and 0.10 M tetrabutylammonium ion (TBA^+) than in 0.10 M TBA^+ alone. It is also reasonable that the rate of the analogous reaction on TiO_2 might respond to Li^+ likewise given the approximate similarity of their surfaces. Simple double layer theory arguments predict that the specifically adsorbed cations should reduce the rate of heterogeneous reduction of a cationic mediator. Furthermore, while not

conclusive, considerations of the dark current of a cell having dtb-bpy as the mediator supports this argument. For example, the dark current for the reduction of dtb-bpy^{3+} is approximately the same magnitude at the V_{oc} with Li^+ present as it is at the lower V_{oc} in the absence of Li^+. Put another way, the effective overpotential for this reduction in the dark increases by an amount roughly equal to the shift in V_{oc} upon addition of Li^+ to solution.

In a sense, this Li^+ effect is more intuitive with cobalt mediators than with I^-/I_3^-. Decreasing the recombination rate by any mechanism should increase both V_{oc} and J_{sc}. Consequently, if J_{sc} increases so should V_{oc}, all else being equal. The apparent conundrum is with the I^-/I_3^- system. There, the effect of the decrease in the recombination rate is insufficient to offset the shift in the conduction band, which on the surface gives rise to the intuitive contradiction

Pyridine Effect. The effect on V_{oc} of adding 4-*t*-butylpyridine to a cobalt mediator solution parallels the behavior with the I^-/I_3^- mediator system—a modest improvement results. As is evident from Figure 7, there is also a small increase in J_{sc} that is not typical of the I^-/I_3^- mediator system.[22] When both 4-*t*-butylpyridine and Li^+ are present in solution, the increase in V_{oc} is significantly greater than for either alone (see Figure 7). The effect of added 4-*t*-butylpyridine on the energy of the conduction band and any other acceptor states in the TiO_2 is anticipated to be the same as with I^-/I_3^-. Additionally, the same effect was observed whether the 4-*t*-butylpyridine was added directly to the mediator solution or whether the photoanode was pre-treated by soaking in a solution of it.

Optimized Mediators. To fabricate DSSCs with better performance—i.e. higher η and FF—the composition and concentration of the more promising mediators were surveyed. For dtb-bpy, d3p-bpy, and dp-bpy we found that optimal mediators were formed from saturated solutions of the corresponding Co(II) complexes and 0.5 M lithium triflate. The solubility limit in gBL is less than 0.5 M for dtb-bpy and less than 0.3 M for d3p-bpy and dp-bpy in MPN. The oxidized form of these complexes are considerably less soluble than the corresponding Co(II) complexes under these conditions, and oxidation of 10% of the saturated solutions led to precipitation of an unknown, but minimal amount of the Co(III) complex.

The dn-bpy and ttb-terpy-based mediators show optimal performance at less than saturated concentrations. That is to say, above ca. 0.3 M, addition of more mediator actually lowers the η of a cell, but it is likely that there is a different explanation in each case. For dn-bpy, addition of the complex causes a dramatic increase in the viscosity of the mediator solution, much more so than for any of the other mediators under study. The self-exchange rates of cobalt complexes of this type are known to be slow,[27,28] thus it is safe to assume that the process of mediation is diffusion controlled. Under high viscosity conditions, this diffusional transport of mediator between dye-sites and the cathode is hindered and thus could become the limiting factor in determining J_{sc}. This is consistent with the behavior observed, i.e., as the concentration of dn-bpy is increased, J_{sc} first increases, then decreases. For cells containing a ttb-terpy-based mediator, similar behavior is observed, however, we believe the peaking of J_{sc} values is due to the high $\varepsilon_{\lambda max}$ observed for this complex—and since viscosity is not significantly different even at high concentrations of mediator. Above ca. 0.3 M, the benefit of having additional

mediator is outweighed by the reduction in the amount of light reaching the entire thickness of the photoanode: the ttb-terpy mediator simply begins to out-compete the dye for light.

Table 3 lists the data obtained for DSSCs fabricated using "optimized" cobalt mediators and comparable I^-/I_3^- mediators. All the cobalt complex mediated cells suffer from a V_{oc} that is 100-200 mV less than the comparable I^-/I_3^- mediated cells. Nonetheless, the performance of these cells is still quite good, and the η relative to a comparable I^-/I_3^- mediated cell (η_{rel}) is greater than 50% for d3p-bpy and dtb-bpy mediated cells. Cells containing the dtb-bpy-based mediators have exhibited the best performance to date, and Figure 8 shows the current-voltage response of such a cell, which exhibits a FF of 62% and η_{rel} of 82%.

Conclusions

The results that we have obtained to date indicate that cobalt complexes of relatively simple and commercially available alkyl-substituted polypyridines are promising electron-transfer mediators for use in DSSCs. Cyclic voltammetric studies have shown a dramatic surface dependence of the electron-transfer kinetics, which empirical evidence suggests is a necessary attribute for an efficient mediator. The electrochemical results also led to the discovery that gold and carbon outperform platinum as cathode materials in these cells. Furthermore, these mediators show no tendency to be corrosive, enabling the use of metallized SnO_2:F electrodes required in large-area DSSCs.[10]

Photoelectrochemical measurements of cobalt complex-mediated cells revealed that addition of lithium salts dramatically improves their performance. We have concluded that the Li^+ effect observed with these mediators—in contrast to I^-/I_3^- mediated cells

where V_{oc} decreases instead of increasing—is due primarily to a reduction in the recombination rate between $Co(III)L_3$ and the electrons in TiO_2 and/or the SnO_2:F collector. Several of the complexes studied were efficient mediators with dtb-bpy being the best among these. This is a particularly significant discovery because the best performing of these complexes can be made in one step from commercially available reagents without the need for further purification.

Besides being non-volatile, non-corrosive, and lightly colored, there is an inherent advantage with cobalt complex mediators that the I^-/I_3^- mediator lacks: they can be easily modified. This research represents our first efforts to understand this new class of electron-transfer mediator. As we continue to modify, study, and improve these cobalt complex mediators, the realization of truly inexpensive, stable, and efficient DSSCs grows nearer.

Chapter 4.

Tables

Table 4.1. Extinction coefficients of cobalt(II) complexes.

Complex	λ_{max} (nm)	$\varepsilon_{\lambda_{max}}$ (M^{-1} cm^{-1})
ttb-terpy	450	1.4×10^{3}
dtb-bpy	440	1.4×10^{2}
d3p-bpy	440	1.1×10^{2}
dn-bpy	440	1.1×10^{2}
bdb-amd	440	1.5×10^{2}

Table 4.2. Electrochemical properties of cobalt(II/III) complexes.

	Glassy Carbon		Gold		Platinum	
Complex	$E_{½}$ (V)[b]	ΔE_p (V)[b]	$E_{½}$ (V)[b]	ΔE_p (V)[b]	$E_{½}$ (V)[b]	ΔE_p (V)[b]
te-terpy	126	200	91	111	89	156
ttb-terpy	0	77	-5	75	(a)	(a)
bpy	222	86	219	60	222	60
4,4'-dmb	90	171	80	110	150	290
5,5'-dmb	130	115	126	60	129	64
tm-dmb	12	123	4	57	88	326
dtb-bpy	90	271	52	86	(a)	(a)
dp-bpy	122	94	120	69	148	162
d3p-bpy	171	116	169	82	(a)	(a)
dn-bpy	82	80	86	76	104	221
phen	309	198	302	87	310	153
phen-phen	142	60	145	75	158	163
dtb-est	403	103	471	398	486	631
bdb-amd	446	101	451	86	520	442

a) No discernable cathodic peak

b) Voltage is reported here versus the saturated calomel electrode

Table 4.3. Photoelectrochemical properties of DSSCs.

Mediator[a]	Solvent	V_{oc} (Volts)	J_{sc} (mA cm^{-2})	FF (%)	η^b (%)	$\eta_{rel}{}^c$ (%)
0.25 M dn-bpy, 0.25 M LiTriflate	gBL	0.43	0.89	59	0.22	31
0.25 M dp-bpy, 0.2 M $LiClO_4$	MPN	0.40	0.97	49	0.19	27
0.25 M ttb-terpy, 0.5 M LiTriflate	MPN	0.40	1.71	48	0.32	45
0.2 M d3p-bpy, 0.2 M $LiClO_4$	MPN	0.47	1.47	59	0.41	58
0.25 M dtb-bpy, 0.5 M LiTriflate	gBL	0.51	2.40	47	0.57	80
0.25 M LiI, 0.03 M I_2	MPN	0.60	2.03	58	0.71	—
Sat'd dtb-bpy, 0.5 M LiTriflate[d]	gBL	0.44	4.82	62	1.30	82
0.5 M LiI, 0.05 M I_2[d]	MPN	0.57	5.32	52	1.58	—

a) The concentrations of complex given are for the total cobalt; each solution is 9:1 Co(II):Co(III). A gold cathode was used for all cells containing cobalt complex mediators; a platinum cathode was used in I^-/I_3^- mediated cells. These mediator solutions also contained 0.2 M 4-*t*-butypyridine (see "d" below for exceptions).

b) All efficiency measurements were carried out under 100 mW cm^{-2} (~1 sun) illumination.

c) This is the efficiency relative to a comparable I^-/I_3^- mediated cell.

d) The photoanodes in these cells were constructed with acetic acid prepared TiO_2, and after dyeing, were soaked in 0.2 M 4-*t*-butypyridine in ACN just prior to use.

Chapter 4.

Figures

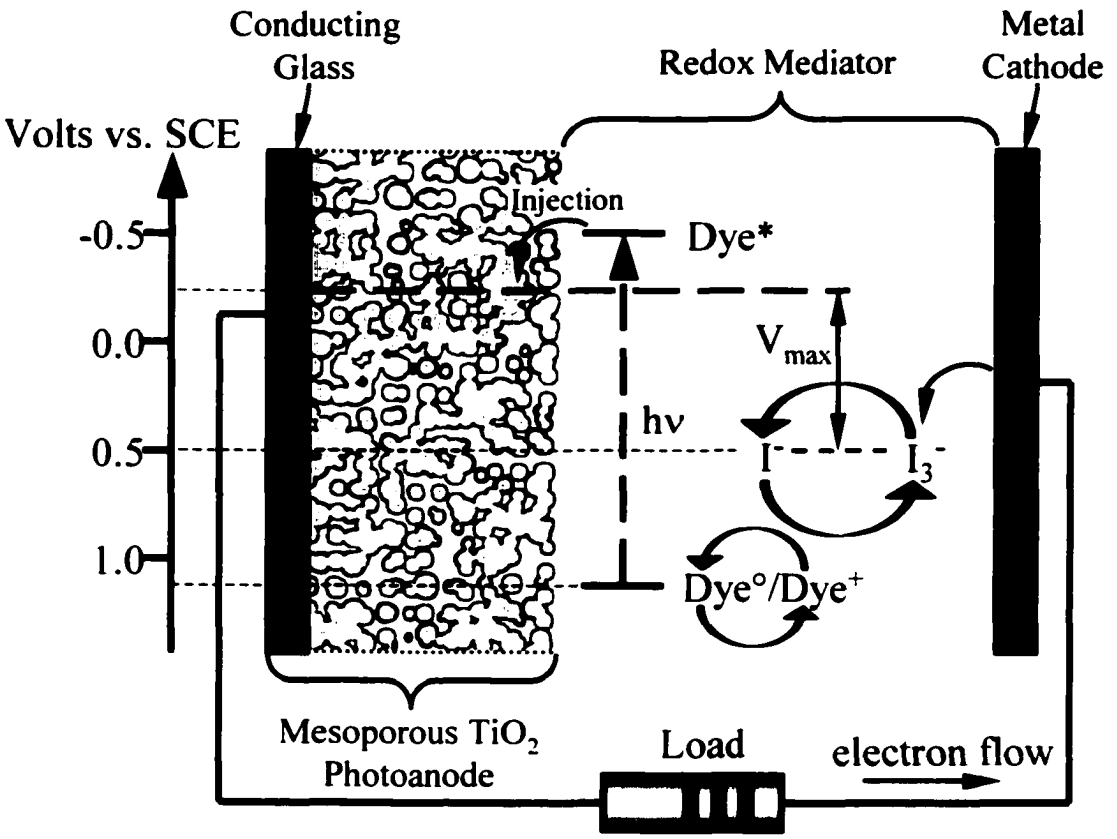

Figure 4.1. Basic construction and operation of a I-/I3- mediated DSSC. The energy scale on the left is in units of volts versus the saturated calomel electrode (SCE).

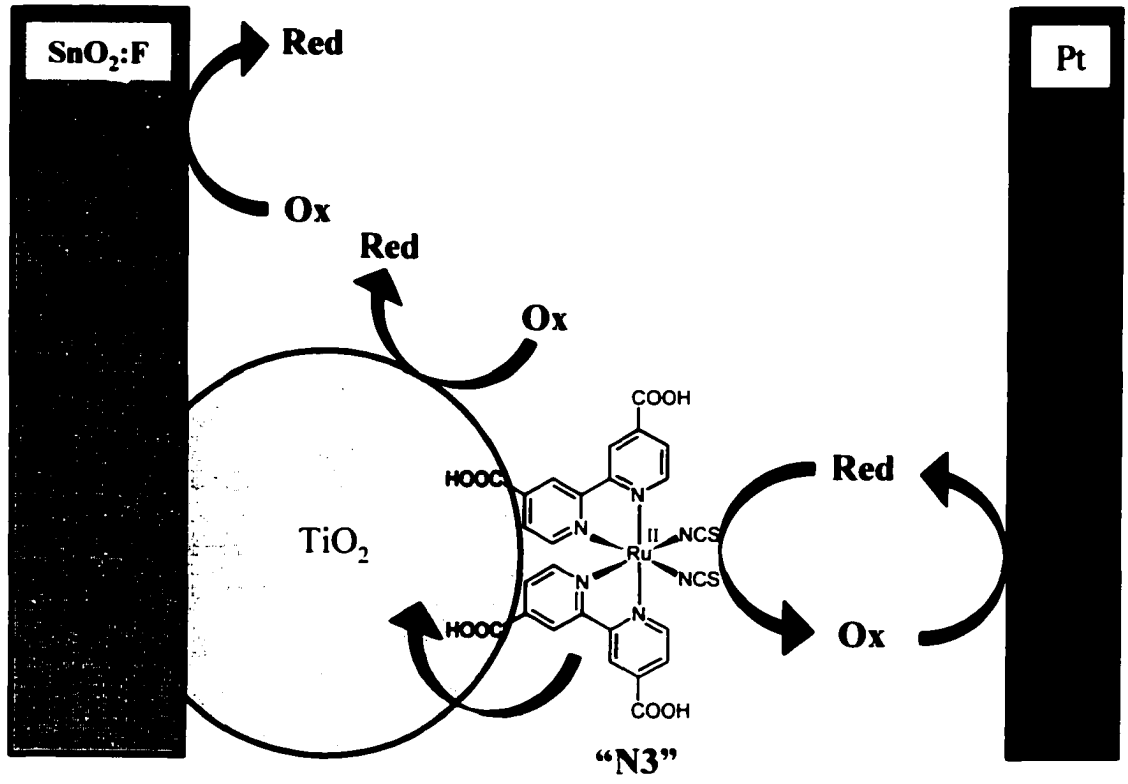

Figure 4.2. Electron-transfer processes in DSSCs. The shaded arrows represent the injection and mediation processes, whereas the solid black arrows represent parasitic recombination reactions.

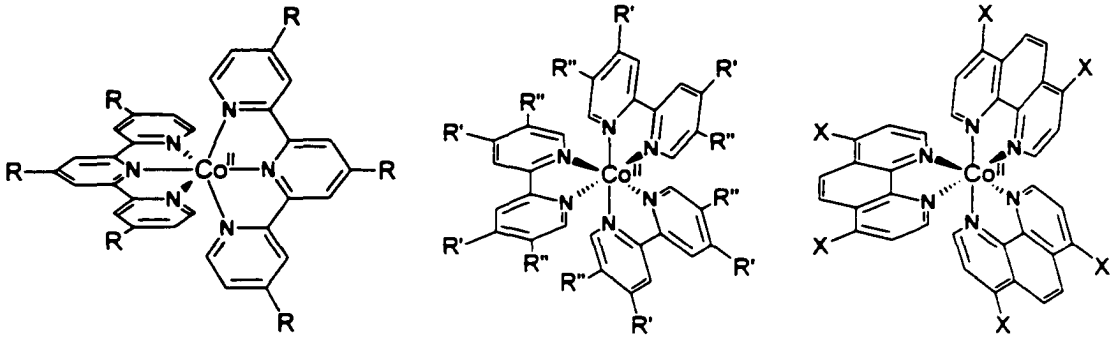

R = ethyl (te-terpy)

R = *t*-butyl (ttb-terpy)

R' = H, R" = H (bpy)

R' = CH_3, R" = H (4,4'-dmb)

R' = H, R" = CH_3 (5,5'-dmb)

R' = CH_3, R" = CH_3 (tm-bpy)

R' = 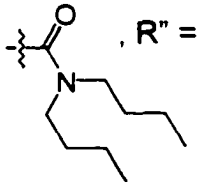 , R" = H (bdb-amd)

R' = *t*-butyl, R" = H (dtb-bpy)

R' = COO-*t*-butyl, R" = H (dtb-est)

R' = phenyl, R" = H (dp-bpy)

R' = 3-pentyl, R" = H (d3p-bpy)

R' = nonyl, R" = H (dn-bpy)

X = H (phen)

X = phenyl (phen-phen)

Figure 4.3. The series of terpyridine, bipyridine, and phenanthroline complexes of cobalt(II) synthesized and employed in this study. The abbreviated names, as used in the text, refer to the entire complex, not the ligands.

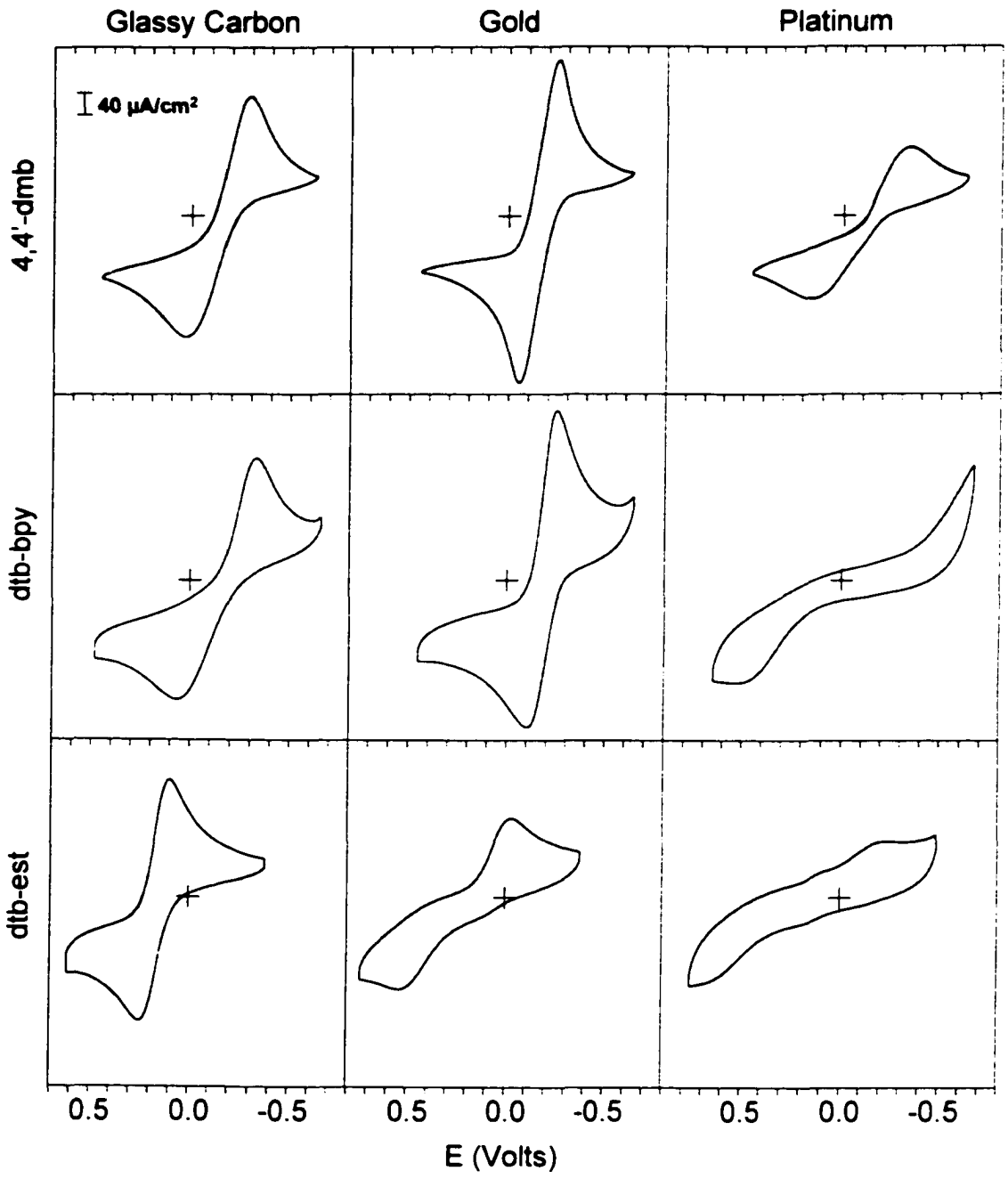

Figure 4.4. Cyclic voltammograms of three different cobalt complexes (in rows) on three different electrodes (in columns). The vertical axis is current density to compensate for modest differences in electrode areas, and the scale is indicated in the upper left hand corner. The concentration of the complexes was 10^{-3} M, and the scan rate was 200 mV s^{-1}. See the text for details.

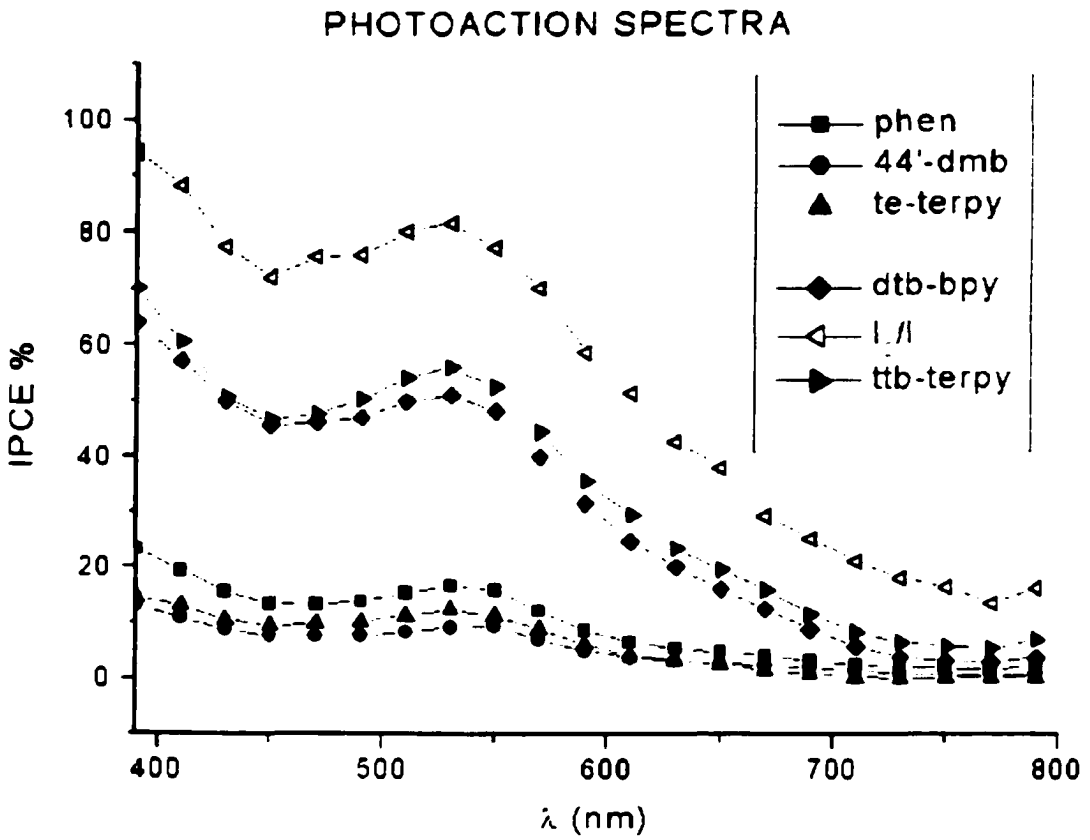

Figure 4.5. Photoaction spectra of N3 bound to nanocrystalline TiO_2 films in the presence of different electron mediators in MPN solutions: 0.25 M LiI / 25 mM I_2 (—◁—). 0.25 M ttb-terpy^{2+} / 25 mM $NOBF_4$ (—▶—). 0.25 M dtb-bpy^{2+} / 25 mM $NOBF_4$ (—◆—). 0.25 M phen^{2+} / 25 mM $NOBF_4$ (—■—). 0.25 M te-terpy^{2+} / 25 mM $NOBF_4$ (—▲—). saturated (< 0.15 M) 4,4'-dmb^{2+} / 15 mM $NOBF_4$ (—●—). 0.25 M $LiClO_4$ was added to all solutions containing a cobalt mediator.

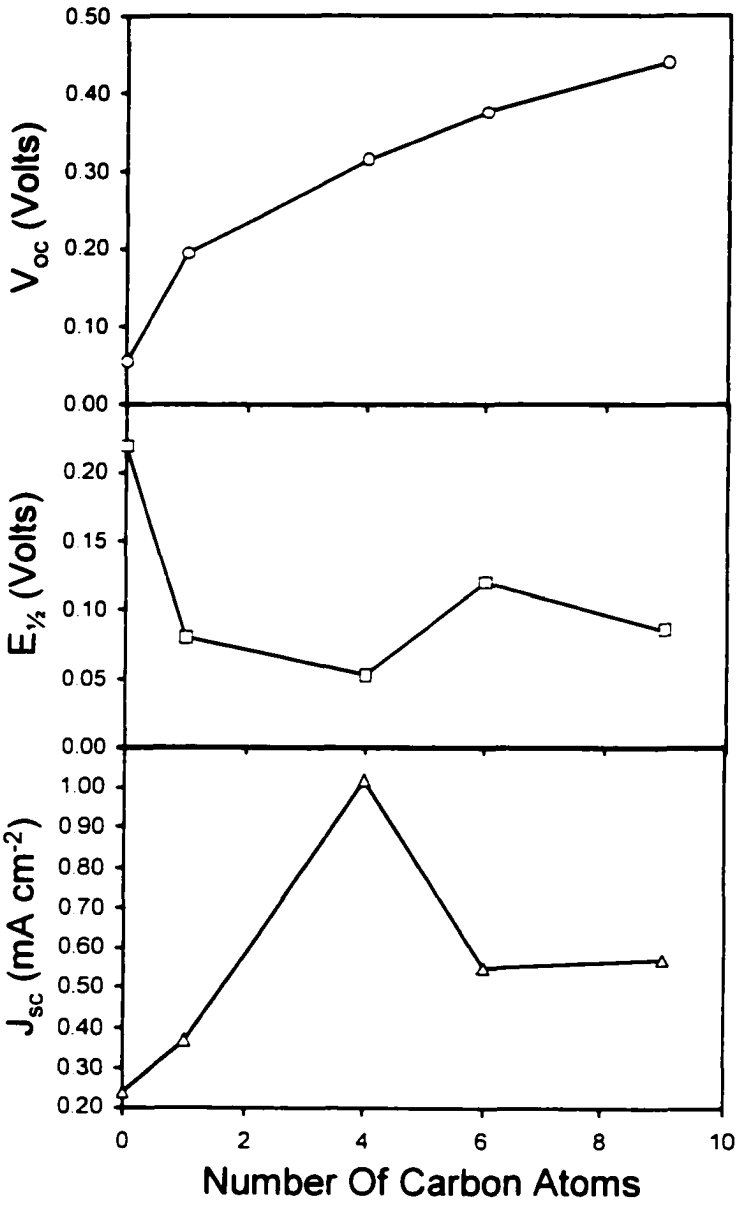

Figure 4.6. A plot of V_{oc}, $E_{1/2}$, and J_{sc} as a function of the number of carbon atoms in the alkyl or aryl substituents at the 4 and 4' positions of 2,2'-bipyridine ligands. V_{oc} and J_{sc} were measured in DSSCs with a gold cathode and containing 125 mM Co(II)L_3 and 13 mM $NOBF_4$ in MPN.

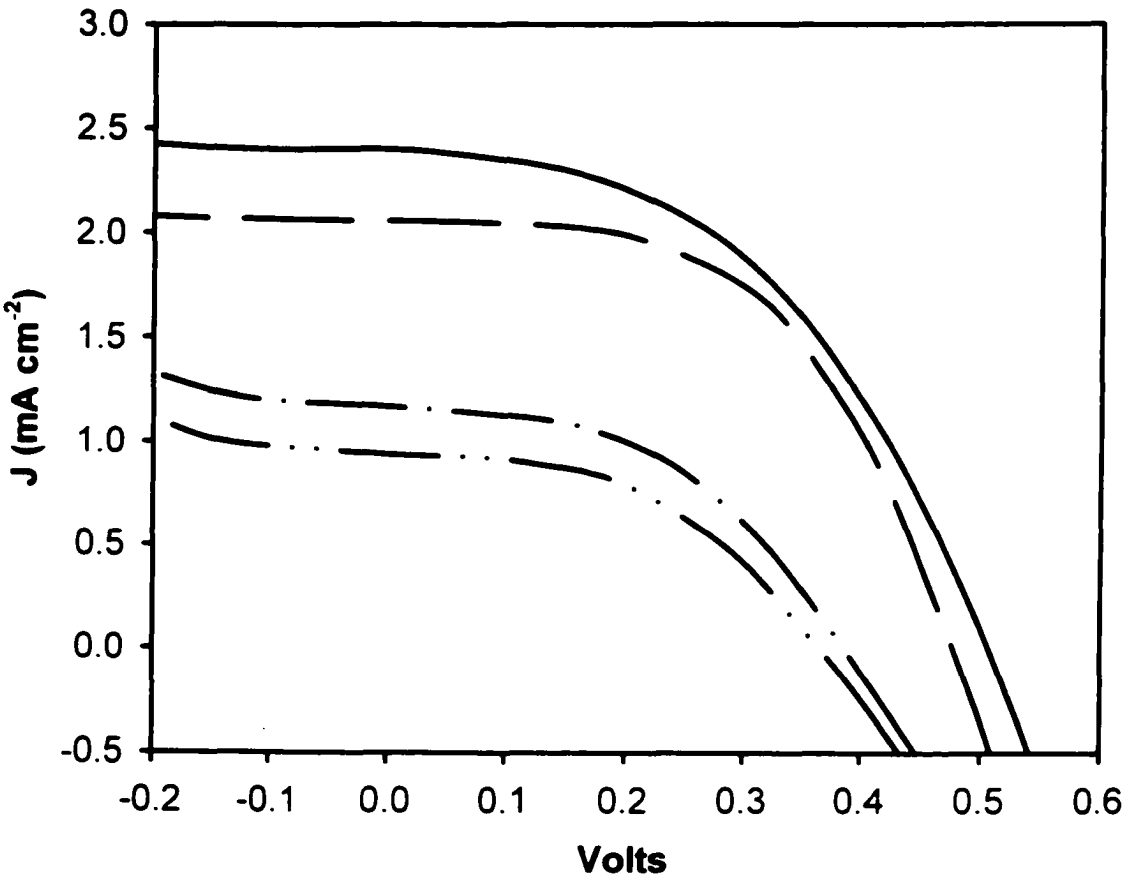

Figure 4.7. Current-voltage response of DSSCs with a gold cathode and containing: 0.25 M dtb-bpy and 25 mM $NOBF_4$ in gBL (— · · —), with added 0.2 M 4-*t*-butylpyridine (— · —), with added 0.2 M 4-*t*-butylpyridine and 0.2 M lithium triflate (— —), and with added 0.2 M 4-*t*-butylpyridine and 0.5 M lithium triflate (——).

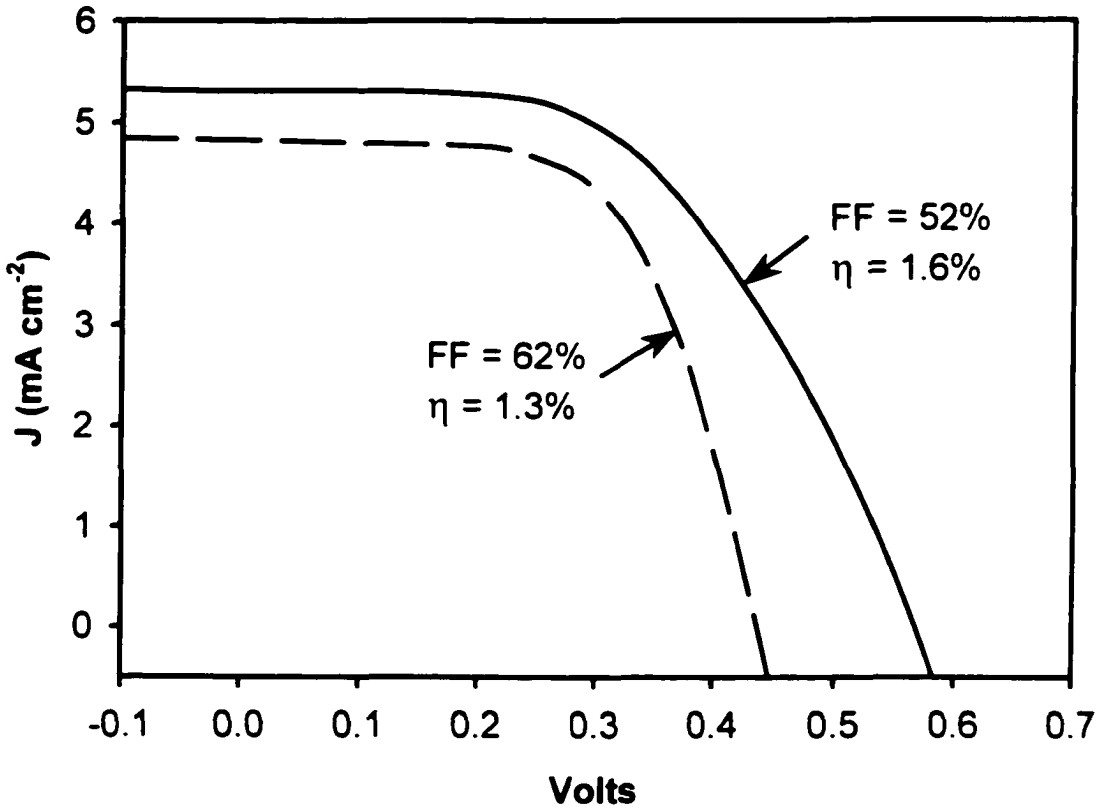

Figure 4.8. Current-voltage response of DSSCs assembled from N3-dyed photoanodes of acetic acid prepared TiO_2. These photoanodes were treated with a solution 0.5 M 4-*t*-butylpyridine in ACN just prior to use. The solid line represents a mediator of 0.5 M LiI and 50 mM I_2 in MPN using a platinum cathode. The dashed line represents a mediator of saturated (< 0.5 M) dtb-bpy, 50 mM $NOBF_4$, and 0.5 M lithium triflate in gBL using a gold cathode.

Chapter 4 References:

(1) Nazeeruddin, M. K.; Pechy, P.; Renouard, T.; Zakeeruddin, S. M.; Humphry-Baker, R.; Comte, P.; Liska, P.; Cevey, L.; Costa, E.; Shklover, V.; Spiccia, L.; Deacon, G. B.; Bignozzi, C. A.; Gratzel, M. *J. Am. Chem. Soc.* **2001**, *123*, 1613.

(2) Green, M. A. *MRS Bull.* **1993**, *18*, 26.

(3) Watanabe, H. *MRS Bull.* **1993**, *18*, 29.

(4) Hamakawa, Y.; Ma, W.; Okamoto, H. *MRS Bull.* **1993**, *18*, 38.

(5) Cao, F.; Oskam, G.; Searson, P. C. *J. Phys. Chem.* **1995**, *99*, 17071.

(6) Papageorgiou, N.; Athanassov, Y.; Armand, M.; Bonhote, P.; Pettersson, H.; Azam, A.; Gratzel, M. *J. Electrochem. Soc.* **1996**, *143*, 3099.

(7) Murakoshi, K.; Kogure, R.; Wada, Y.; Yanagida, S. *Chem. Lett.* **1997**, 471.

(8) Murakoshi, K.; Kogure, R.; Wada, Y.; Yanagida, S. *Sol. Energy Mater. Sol. Cells* **1998**, *55*, 113.

(9) Savenije, T. J.; Warman, J. M.; Goossens, A. *Chem. Phys. Lett.* **1998**, *287*, 148.

(10) Gregg, B. A.; Pichot, F.; Ferrere, S.; Fields, C. L. *J. Phys. Chem. B* **2001**, *105*, 1422.

(11) Hagfeldt, A.; Gratzel, M. *Acc. Chem. Res.* **2000**, *33*, 269.

(12) Bonhote, P.; Gratzel, M.; Jirousek, M.; Liska, P.; Pappas, N.; Vlachopoulos, N.; Von Planta, C.; Walder, L. *Presented at the 10th International Conference on Photochemical Conversion and Storage of Solar Energy (IPS-10)*, Interlaken, Switzerland, 1994, Abstract C2.

(13) Wen, C.; Ishikawa, K.; Kishima, M.; Yamada, K. *Sol. Energy Mater. Sol. Cells* **2000**, *61*, 339.

(14) Nusbaumer, H.; Moser, J. E.; Zakeeruddin, S. M.; Nazeeruddin, M. K.; Gratzel, M. *J. Phys. Chem. B* **2001**, *105*, 10461.

(15) Sasse, W. H. F.; Whittle, C. P. *J. Am. Chem. Soc.* **1961**, *83*, 1347.

(16) Nazeeruddin, M. K.; Kalyanasundaram, K.; Graetzel, M. *Inorg. Synth.* **1997**, *32*, 181.

(17) Nazeeruddin, M. K.; Kay, A.; Rodicio, I.; Humphry-Baker, R.; Mueller, E.; Liska, P.; Vlachopoulos, N.; Graetzel, M. *J. Am. Chem. Soc.* **1993**, *115*, 6382.

(18) Zaban, A.; Ferrere, S.; Sprague, J.; Gregg, B. A. *J. Phys. Chem. B* **1997**, *101*, 55.

(19) Wade, L. G. *Organic Chemistry*; 2nd ed.; Prentice-Hall, Inc.: Englewood Cliffs, New Jersey, 1991; Chapter 17.

(20) Bard, A. J.; Faulkner, L. R. *Electrochemical Methods*; 1st ed.; John Wiley & Sons: New York, 1980; Chapter 3.

(21) Cahen, D.; Hodes, G.; Graetzel, M.; Guillemoles, J. F.; Riess, I. *J. Phys. Chem. B* **2000**, *104*, 2053.

(22) Huang, S. Y.; Schlichthorl, G.; Nozik, A. J.; Gratzel, M.; Frank, A. J. *J. Phys. Chem. B* **1997**, *101*, 2576.

(23) Kelly, C. A.; Farzad, F.; Thompson, D. W.; Stipkala, J. M.; Meyer, G. J. *Langmuir* **1999**, *15*, 7047.

(24) Liu, Y.; Hagfeldt, A.; Xiao, X. R.; Lindquist, S. E. *Sol. Energy Mater. Sol. Cells* **1998**, *55*, 267.

(25) Enright, B.; Redmond, G.; Fitzmaurice, D. *J. Phys. Chem.* **1994**, *98*, 6195.

(26) Pelet, S.; Moser, J.-E.; Graetzel, M. *J. Phys. Chem. B* **2000**, *104*, 1791.

(27) Szalda, D. J.; Creutz, C.; Mahajan, D.; Sutin, N. *J. Phys. Chem.* **1983**, *22*, 2372.

(28) Newton, M. D. *J. Phys. Chem.* **1991**, *95*, 30.